Charged Particle Dynamics of Negative-ion-rich Plasma in the Negative Hydrogen Ion Source for NBI

Shaofei GENG

Doctor of Philosophy

Department of Fusion Science
School of Physical Sciences
SOKENDAI (The Graduate University for Advanced Studies)

SOKENDAI

(The Graduate University for Advanced Studies)

Charged Particle Dynamics of Negative-ion-rich Plasma in the Negative Hydrogen Ion Source for NBI

Shaofei GENG

Doctor of Philosophy

2016

Contents

Abstract

Neutral beam injection (NBI) is an effective method for plasma heating and current drive for fusion devices. In a neutral beam injector, charged particles are produced in the ion source, accelerated, neutralized and injected into the target plasmas confined in the fusion machine. Having the advantages of high neutralization efficiency, negative-ion-based Neutral Beam Injector (N-NBI) has been intensively developed to inject the beam with sufficient penetration length in the fusion plasmas. As the source of negative ions, the negative ion source determines the performance of the N-NBI system. Comparing to positive ion sources, negative ion sources have some differences, which are (1) the negative ones involve strong magnetic field to magnetize electrons in the source, (2) the source plasma consists of electrons, positive and negative ions, and (3) a part of electrons are extracted together with negative ions. In order to understand the mechanisms of electron and positive ion flow during beam extraction and the extraction of negative ions in Cs-seeded plasmas for the improvement of the present negative hydrogen ion source, investigation on charged particle dynamics of the negative-ion-rich plasma has been conducted. In this research, Langmuir probe, cavity ring-down, photodetachment, and four-pin directional Langmuir probe have been utilized for the experiments on the negative hydrogen ion source to investigate the characteristics of the negative-ion-rich plasma and the charged particle flows.

In Chapter 1, the worldwide energy issue and the importance of the development of magnetic confinement fusion was introduced. A neutral beam injector can inject high energy particles into a fusion device to heat the target plasma and drive plasma current. Having the advantages of high neutralization efficiency and low beam divergence angle, the N-NBI system is a preferable choice. The basis of negative hydrogen ion source has been introduced in this Chapter. In a negative hydrogen ion source, negative ions (H^-) are produced by two mechanisms: (1) volume production and (2) surface production. In a practical negative ion source, Cs vapor is seeded and H^- ions are mainly produced by

the mechanism of surface production. At National Institute for Fusion Science (NIFS), remarkable results have been achieved. The injection energy reached 190 keV and the total injection power was kept more than 15 MW. Research on improvements of the negative ion source is still necessary to obtain the stable and high power beam injections. In the R&D Negative Hydrogen Ion Source (NIFS-RNIS), negative-ion-rich plasma, of which electron density is one to two orders lower than that of H^- ion, has been observed in the beam extraction region. During beam extraction, H^- ion density decreases due to the extraction and electrons flow to the extraction region together with positive ions. Consequently, negative-ion-rich plasma is contaminated with electrons, and the co-extracted electron current is increased. The co-extracted electrons are filtered from the beam and absorbed onto the extraction grid. Increment of co-extracted electron current carries more heat load to the extraction grid and causes damages in high power and long pulse beam acceleration. Understanding of the mechanisms of the electron and positive ion flow in the extraction region and H^- extraction is required for the improvement of the negative hydrogen ion source.

In Chapter 2, the negative ion source RNIS utilized for the experiments was introduced and described, as well as the diagnostic methods. This ion source is divided into a driver region and an extraction region by a transversal magnetic field named filter field. Plasma is generated by filament-arc discharge and confined in the multi-cusp magnetic field. Diagnostic tools including Langmuir probe, cavity ring-down and photodetachment technique have been applied to the experiments. Langmuir probe provided basic plasma parameters, for example, plasma potential V_s, electron density n_e, electron temperature T_e and so on. Although line-averaged H^- ion density has been accurately obtained by cavity ring-down, H^- ion density at a specific point is necessary for this research. For this purpose, photodetachment technique has been applied to the experiments. H^- ion density n_{H^-} is proportional to the photodetachment current and a coefficient is required to evaluate n_{H^-}. In the conventional photodetachment method for electron-rich plasma, the coefficient is determined by the ratio of photodetachment current to electron saturation current of the probe. However, this method is not available in negative-ion-rich plasma. Then a new method based on the combination of cavity ring-down and photodetachment has been developed to determine the coefficient for the

estimation of n_{H^-}. This is the first time that n_{H^-} at a specific point is measured in a Cs-seeded negative ion source. In principle, this new method has no limitation of plasma condition.

In Chapter 3, the basic characteristics of the RNIS have been investigated by the diagnostics tools introduced in Chapter 2. The negative ion source requires long Cs-conditioning time because of the complicated and slow Cs expansion. After seeding Cs into the plasma, the plasma potential V_s decreases due to the emission of H^- ions from the plasma-grid surface. The density of surface-produced H^- ions increases comparable to electron density n_e, which decreases as increasing n_{H^-} during Cs-seeding. The electron density n_e is sensitive to the bias voltage applied to the plasma grid with respect to the plasma chamber, and n_e decreases at higher bias voltage. n_{H^-} in the extraction region is lower at higher bias voltage of the plasma grid. It is necessary to apply low bias voltage to the plasma grid to obtain high H^- beam current with the premise of avoiding damage on the extraction grid. Hydrogen pressure also influences the plasma in the extraction region. In this experiments, n_{H^-} decreases at high pressure due to the mutual neutralization with positive ions, since the temperature of positive ions decreases at high pressure and the reaction rate of mutual neutralization increases. Therefore, extraction and acceleration currents decrease at higher pressure. Low operational gas pressure is beneficial to the negative ion source, because the stripping loss of H^- ions due to collisions with neutral molecules and atoms is reduced. However, the discharge is unstable in extremely low gas pressure, because the plasma of the ion source is sustained by electrons impact ionization and the mean free paths of electrons are larger at lower pressure. In addition, electron percentage in the source plasma increases with respect to H^- percentage in low gas pressure. Consequently, 0.2 to 0.4 Pa of hydrogen pressure is a proper choice for the operation of the negative ion source for NBI.

In the negative hydrogen ion source for NBI, an electron deflection magnetic field (EDM field) is introduced in the extraction gap to filter the co-extracted electrons. This EDM field forms a loop field by partially penetrating into the extraction region. The result of plasma profile measured with a Langmuir probe indicates that the boundary of

the EDM field is at ~10 mm apart from plasma grid. Electrons near the plasma grid are magnetized with the EDM field and trapped into the cusp region of the field.

The plasma response to extraction field has been investigated by scanning the measurement position of the Langmuir probe and photodetachment probe perpendicular to the plasma grid. By comparing the profiles of the probe saturation current and n_{H^-} before and during beam extraction, the profile of the plasma response to the extraction region has been obtained. The results show that the maximum n_e increase and n_{H^-} decrement caused by the beam extraction is at ~20 mm apart from the plasma grid. The linear extrapolation of the profiles suggests the boundary of the extraction region and driver region of the ion source is at ~40 mm apart from the plasma grid. Although the maximum response is initially expected close to the extraction aperture, the experimental results show that the peak position of the plasma response is located far from the plasma grid.

In Chapter 4, flows of electrons and positive ions have been investigated by a four-pin directional Langmuir probe. The flow direction has been determined by the periodic distribution of the probe saturation current by rotating the directional Langmuir probe. The flow speed has been determined by the difference of probe saturation currents at upstream and downstream positions. The movement of electrons and positive ions are ambipolar. Flow changes of electron and positive ion have been observed by subtracting the two-dimensional flow patterns before and during beam extraction. By considering the flow pattern before beam extraction as a background and the transition of flow occurs is in a finite time, the change of the flow velocity is regarded as the flux increments of electrons and positive ions induced by beam extraction. The flux increments are from lower to upper side and trapped into the cusp region of the EDM field. The channel of the flux increments is at ~20 mm apart from the plasma grid and this region is the transition region of the filter field and the EDM field. Therefore, the probe located in this region can detect the maximum plasma response to the extraction field.

In Chapter 5, the four-pin directional Langmuir probe with photodetachment has been utilized to the experiments to investigate H^- flow for the understanding of the extraction mechanism and the unexpected position of the maximum H^- ion density reduction. The

flow velocity has been estimated using the recovery speed of the H^- ion in the photodetachment region at upstream and downstream probe tips. Meanwhile, temperature of H^- ions has been obtained. The result indicates that in the extraction region, temperature of H^- ions is ~0.12 eV which is consistent with the result of saturated cavity ring-down measurement. The two-dimensional flow pattern of H^- ions suggests that H^- ions come from the direction of the plasma grid and flow to the extraction region. During beam extraction, H^- flow turns to the aperture direction at ~20 mm apart from the plasma grid. Therefore, the maximum reduction of n_{H^-} can be detected near this position. In the extraction region, the Larmor radius of H^- ion is ~10 mm. Note that the boundary of the EDM field is at ~10 mm apart from the plasma grid. These two dimensions elucidate the existence of stagnation point of the H^- ions located at ~20 mm apart from the plasma grid.

In conclusion, it becomes clear that H^- ions undergo following sequence from production to extraction by applying extraction field: (1) H^- ions come from the direction of the metal part of the plasma grid, (2) once flow towards the plasma in the extraction region, (3) turn at the stagnation point located at ~20 mm apart from the plasma grid and (4) move to the aperture of the plasma grid. The behavior of the H^- flow is affected by the EDM field and filter field. The region of the stagnation point corresponds to the transition region of the filter field and the EDM field. In this region, the extraction-induced additional electron and positive-ion fluxes increase and the stagnation point appears. Consequently, the maximum plasma response to the extraction field is far from the plasma grid. In addition, the H^- ion temperature is estimated to be ~ 0.12 eV. This is one of the evidences that negative hydrogen ion beam has a low beam divergence angle. In the NIFS-RNIS, H^- ions are not extracted directed from the surface of the plasma grid but mainly from the region near the aperture of the plasma grid.

Since the extraction process occurs in the region near the plasma-grid aperture, the improvement of the negative hydrogen ion source is possible to be focused to this region. One of the improved method is to increase the EDM field, and then boundary of the EDM field becomes far from the plasma grid. More H^- ions will be extracted by increasing the magnetic region. Meanwhile, suppression of electrons near the plasma

grid is then enhanced. Consequently, the increase in the extracted H^- ion current and decrease in electron component are possible. The performance of the negative ion source is expected to improve.

1. Introduction

1.1 Global energy issues and fusion reactor

A fundamental characteristic of modern industrial society is the consumption of large amount of energy. The production and development are driven by the use of technology which depends on the external energy source in the industrial society [1]. The use of large amount of energy is also essential for food production due to the mechanization of agriculture. The required human labor decreases as the increasing efficiency and the excess labor is moved to the urban and participates in the industrial production or service industries. The urban is supported by the input of external energy for the activities of production, daily life, transportation, storage, and so on [2]. Consequently, the growth of modern industrial society is correlated with the energy consumption. Figure 1-1 shows the correlation of energy use and gross domestic product (GDP) around the world in 2012. It is apparent that the countries having higher GDP per capita consumed more energy.

During the first industrial revolution, coal became the main source of energy in the production activities. In the past decades, fossil fuel including oil, coal, and natural gas so on, captured around 80% of the energy consumption for human beings as illustrated in Figure 1-2. The heavy used of the fossil fuel caused serious environment issues. Most of the greenhouse gas emissions come from the combustion of fossil fuels which also produces pollution to the air due to the emissions of SO_2, NO_x, and heavy metals. As a consequence, acid rain is produced and falls to the Earth causing influence to the natural. In addition, the polluted air can also lead to respiratory diseases because the particles of the emissions can induce negative effects to the health when inhaled by people.

Presently, the fossil fuel supports the source of the energy mainly. Unfortunately, the amount of fossil fuel is limited and cannot be reproduced. Figure 1-3 shows the so called "peak oil" theory [3] which indicates the point of the maximum production of petroleum.

After the peak oil point, the rate of production of petroleum is expected to enter terminal decline and people have to face to the shortage of energy for the daily life and the growth of industry. This brings a demand to find an alternative energy source for the future.

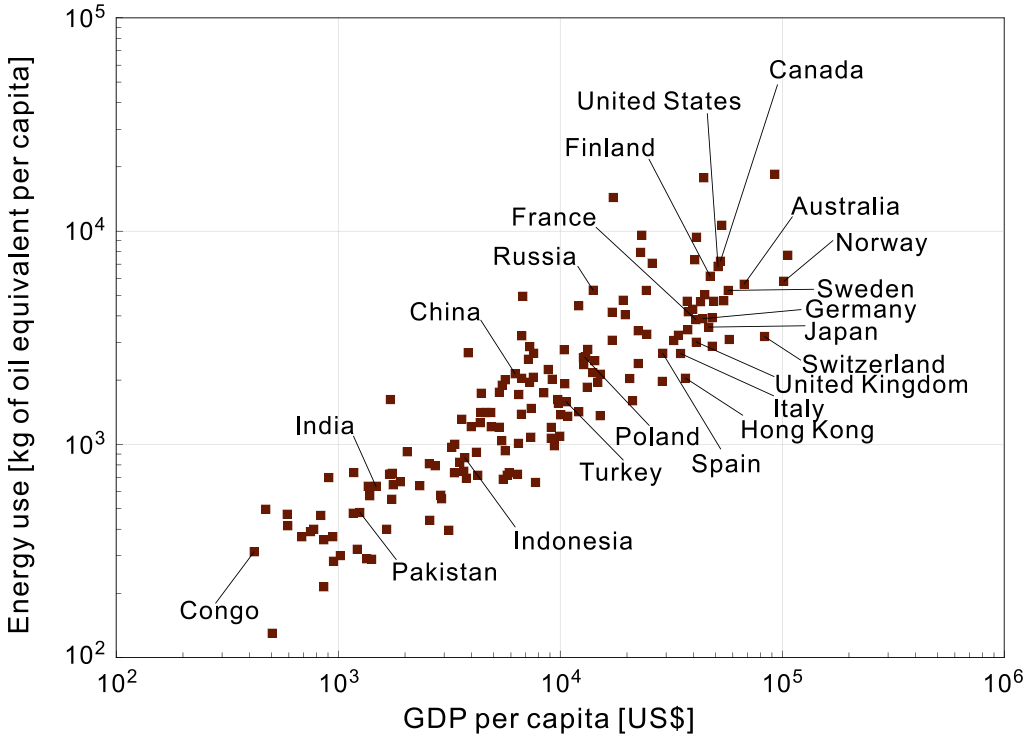

Figure 1-1. Annual energy consumption versus annual GDP per capita. (Data source: World Bank Group, 2012)

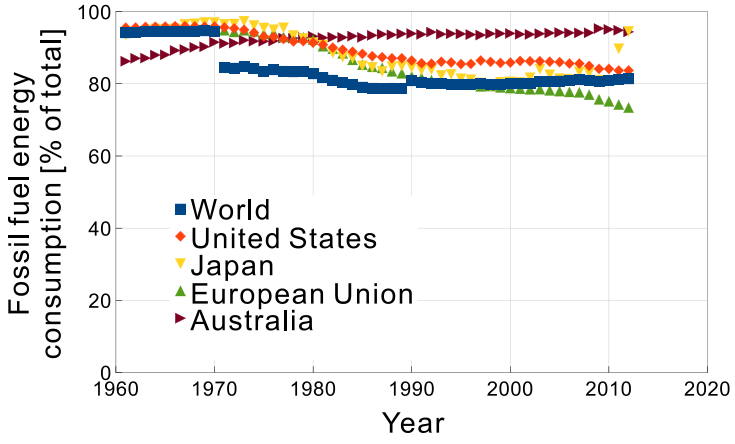

Figure 1-2. Fossil fuel energy consumption. Fossil fuel comprises coal, oil, petroleum, and natural gas products. (Data source: World Bank Group, 2012)

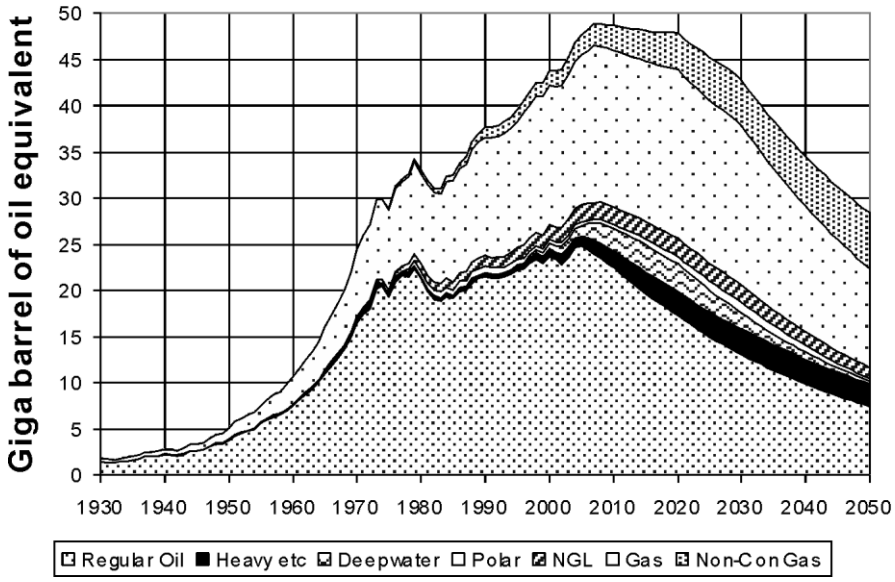

Figure 1-3. Oil and gas production profile [3].

Even renewable energy which comes from the resources can be naturally replenished, such as solar energy, wind, tides, and geothermal heat etc. have been widely developed, its efficiency is limited and the stability is influenced by the circumstance. Actually, these energy resources fluctuate time by time and the deviation exceeds the acceptance of the industrial usage of electricity. Nuclear power plants based on nuclear fission seems a good choice because of the low fuel consumption. However, people have to consider the risk of accidents and incidents of nuclear power plants. Additionally, disposal of the nuclear waste, including high-level, intermediate-level, and low-level waste, is a critical issue since people have to develop technology to seal the radionuclide safely and find appropriate permanent sites which is still under way in some countries [4].

Without the disadvantages of the emissions of greenhouse and toxic gases, particulates and inducing environmental disaster due to accidents, a nuclear fusion reactor is considered as an excellent alternative to fossil fuel and fission reactor. In a fusion reactor, nuclear fusion reactions occur when two atomic nuclei come close enough and then collide to form a new nucleus since the strong nuclear force which pulls the two nuclei together exceeds the Coulomb's force which pushes them away. Large amount of energy is released during this process. Nuclear fusion is the mechanism of energy production in a star [5].

For a fusion reactor used for a power plant, the fuel is limited to the lightest element which is the easiest atom to ignite because of the small charge. The isotopes of hydrogen, deuterium (D) and tritium (T) are selected as the fuel for a fusion reactor. The process of the fusion of deuterium and tritium is

$$D + T \rightarrow {}^{4}He\ (3.5\ MeV) + n\ (14.1\ MeV). \tag{1-1}$$

Deuterium is a stable isotope of hydrogen and can be extracted from seawater. Tritium is not stable and quite rare in nature. It can be produced inside the fusion reactor from the breeding blanket when energetic neutrons impact the lithium of the blanket:

$$n + {}^{6}Li \rightarrow T + 4He + 4.8\ MeV, \tag{1-2}$$

$$n + {}^{7}Li \rightarrow T + 4He + n - 2.5\ MeV. \tag{1-3}$$

The reaction cross section σ is an evaluation of the fusion reaction probability which depends on the relative velocity of the two colliding nuclei. Usually, the nuclei have a velocity distribution. Therefore, an average over the distributions of cross section and velocity, $<\sigma v>$, which is called "reactivity", is used to evaluate the reaction rate. Figure 1-4 indicates that for D-T reaction, high temperature is necessary since the reactivity decreases rapidly when the temperature is lower than 20 keV. At the temperature required according to Figure 1-4, the fuel deuterium and tritium exist in plasma state.

Huge amount of supply of power is required to the fusion reactor to produce and maintain the deuterium and tritium plasma. In order to realize net output of energy from a fusion reactor, the heating of the plasma by fusion reaction is required to be sufficient to maintain the temperature of the plasma and to compensate the power losses from the plasma, and then a steady state can be obtained. The condition to obtain such steady state of plasma is called "Lawson criterion". Since the produced heating by fusion reaction can sustain the plasma temperature against the energy losses, the applied external heating can be removed and the plasma is maintained by internal heating. The Lawson criterion is the condition for starting burning plasma. It suggests a minimum requirement on the product of plasma (electron) density n_e, confinement time τ_E, and plasma temperature T_{pl}. For D-T reaction, the requirement for starting burning plasma is

$$n_e\, T_{pl}\, \tau_E > 3 \times 10^{21}\ m^{-3}\ keV\ s. \tag{1-4}$$

The minimum value of the product $n_e T_{pl} \tau_E$ appears when the plasma temperature is close to 14 keV [6]. It is essential to heat up the plasma in a fusion reactor above the ignition temperature.

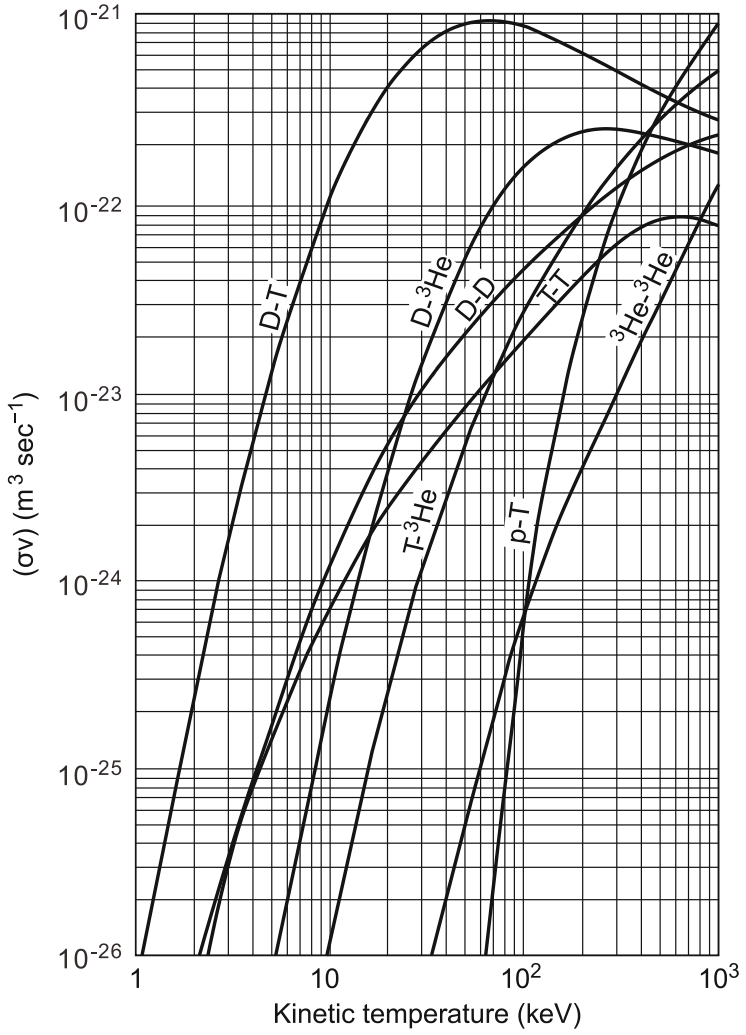

Figure 1-4. Fusion reaction rate between light atoms [5].

1.2 Neutral beam injection

There are several means to heat up the plasma in a fusion reactor including ohmic heating, electron cyclotron resonance heating (ECRH), ion cyclotron resonance heating

(ICRH), and neutral beam injection (NBI) heating. The theme of this thesis focuses on the neutral beam injection (NBI). Only NBI will be introduced.

The fundamental concept of NBI is the injection of a high-energy beam of neutral atoms, typically hydrogen or deuterium into the plasma in the fusion reactor. The atoms in the high-energy beam transfer their energy to the plasma, and then the plasma is heated up and temperature increases.

By injecting high-energy neutral beam into the plasma in a fusion reactor, a neutral beam injector is possible to be applied for several purposes. They are summarized as followings:

(1) Plasma heating [7,8]

In order to realize the plasma temperature higher than 10 keV for ignition, neutral beam injection heating is one of the approaches. The energetic neutral atoms injected into the plasma from a neutral beam injector are ionized by electron-impact ionization, ion-impact ionization, and charge exchange, and then captured by the magnetic field of the fusion reactor. The energetic ions converted from the neutral atoms transfer their energy to electrons and ions by collisions. The temperature of plasma increases, consequently.

Plasma heating by NBI has archived remarkable results for fusion reactor research. For instance, fusion power of 16 MW has been produced at 22.3 MW of input NBI power on the Joint European Torus (JET) [9].

(2) Current drive [10,11]

On a Tokamak-type fusion reactor, plasma current is important for the confinement of the plasma. It is difficult to produce the plasma current continuously by the transformer via the change of magnetic flux for long time. Neutral beam injection acts as one of the effective methods for non-inductive current drive for the steady operation of a Tokamak-type fusion reactor.

(3) Fuelling [8]

In addition to the injection of gas puffing and pellets injection to increase the plasma density, neutral beam injection is also a desirable method to fuel the fusion reactor. The particle flux from NBI can be expressed as

$$N_f = 6.25 \times 10^{21} P/E_f, \quad (1\text{-}5)$$

where the N_f is the particle flux, P is the injection power in MW, and E_f is the injection energy in keV.

Particles from NBI can fuel the central plasma due to their high energy. This is essential to control the central plasma density.

(4) Plasma diagnostics [12-15]

Neutral beam injection can also be applied for the diagnostics of the plasma to measure several plasma parameters such as ion temperature, density of impurities, plasma current density profile, and plasma rotation speed etc. by Doppler effect, Stark effect, and charge exchange recombination spectroscopy (CXRS) after the high energy beam is injected into the plasma.

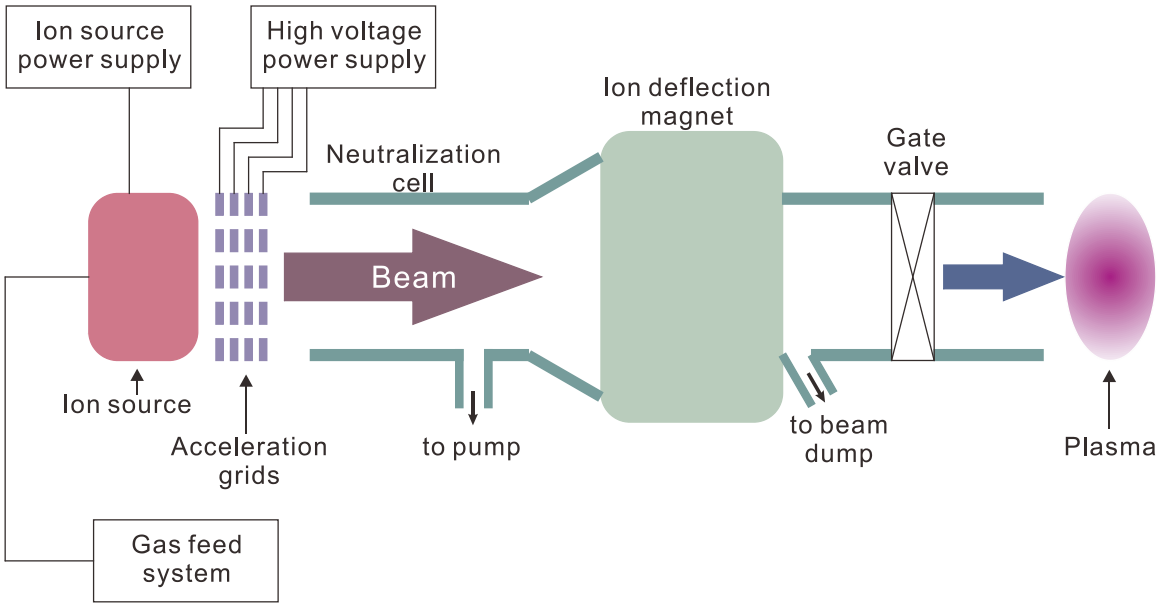

Figure 1-5. Conceptual illustration of a neutral beam injector.

Conceptual view of neutral beam injector is schematically shown in Figure 1-5. At the head part of the neutral beam injector, the left most part of the Figure 1-5, a device producing low temperature plasma is installed, from which, ions are generated and extracted. This device gives the name "ion source". Ions produced in the ion source are extracted by so-called extraction and acceleration grid system which is also known as "beam optical system". Ions are accelerated by the electrostatic field of the acceleration grids and focused to form an ion beam. The ion beam then enters the neutralization cell and the ions collide with the background gas, experience charge exchange for positive ions or electron stripping for negative ions. A part of the ions are neutralized during this process and a neutral beam is formed. The remaining ions which are not neutralized and the positive ions via re-ionization process are then deflected by a magnetic field, and absorbed by a residual ion beam dump. Since the neutralized particles are not influenced by the magnetic field and can pass through the magnetic field directly, the neutral beam is injected into the fusion reactor.

In a fusion reactor, the injected neutral particles experience collision with the background plasma and lose energy during this process. The penetration depth of the neutral beam L depends on the initial energy of the neutral beam and the density of the background plasma:

$$L = (E/A)/18n_e, \tag{1-6}$$

where the unit of L is meter, E is the energy of the neutral beam in keV, A is the mass of the injected neutral particle in amu, and n_e is the plasma density in $10^{19}m^{-3}$. In order to heat the central plasma, high energy neutral beam is desirable.

The neutralization of the accelerated ion beam happens in the neutralization cell of the NBI system by the collisions of ions with background gas and neutralization efficiency is determined by the collision cross sections. For deuteron and proton (D^+/H^+) the maximum neutralization efficiency drops down steepy as the beam energy is higher than 100 keV and decreases to be lower than 20% at 200 keV of beam energy. This brings a serious issue to the overall efficiency of the NBI system and a decrease to the output power. In addition, the remaining ions which are not neutralized in the NBI system causes amount of heat load to the beam. On the other hand, the neutralization

efficiency of negative deuterium / hydrogen ions (D^-/H^-) can keep higher than 60% even the beam energy reaches 1 MeV as shown in Figure 1-6 [16,17]. Having this advantage, the negative ion based NBI system (N-NBI) is a desirable device to obtain high energy beam.

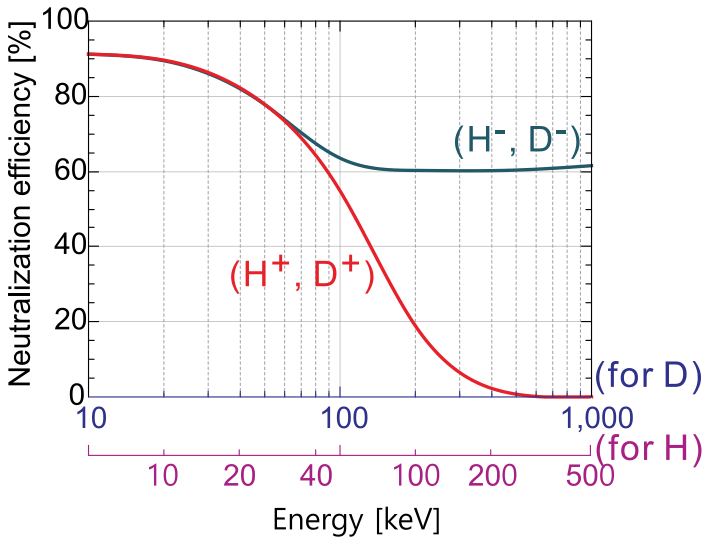

Figure 1-6. Maximum neutralization efficiency of D^- and D+ beam versus beam energy [16].

In addition to the neutralization efficiency, the N-NBI system has advantage in beam divergence. For a Tokamak, dense toroidal coils are necessary in order to generate strong toroidal magnetic field, and then the space for an injection port is limited because the injection port can only be in the gap between two neighbor coils. For a stellarator, the coil structure is complicated in order to generate proper helical magnetic field. A challenge of the injection port design also exists due to the limited space. For a practical fusion reactor, for example DEMO (DEMOnstration Power Plant), D-T reactions happen in the reactor and large number of neutrons is produced. The vessel of the fusion reactor has components for shielding the neutrons. However, the NBI injection port is a leakage window for neutrons. The neutron flux can travel to the outside of the fusion reactor through the injection port. Consequently, an injection port with dimension as small as possible is appropriate. The requirement of small injection port introduces the demand of neutral beam with small divergence.

Under the condition of well designed beam optics system, the minimum beam divergence is influenced by the ion temperature and space charge mainly. The ion temperature introduces a transverse speed in to the particles in the beam. During beam transport, the beam can also expand due to the repulsive force caused by space charge. In an positive ion source based on filament-arc discharge, the ion temperature is around 1 eV [18]. Coupland *et al*. has calculated the ion temperature which reaches 7 eV in a helium ion source [19]. On the other hand, the negative ion temperature in a negative hydrogen ion source is one order lower than the positive ion temperature [20]. Table 1-1 shows the beam parameters of positive NBI system on some devices. It can be found that the divergence angle of the ion beam extracted from positive ion sources is around 1°. This value is consistent with the statement that under "perveance match" condition, 80% of the ion beam current extracted from a positive ion source can be found within a divergence angle of less than ±1.15° [18].

Table 1-1. Beam parameters of positive NBI system on some devices.

Device	Extraction grid dimension [cm]	Transparency	Beam energy [kV] /Current [A] /Pulse width [s]	Current density [A/cm2]	Divergence angle	Ref.
DITE	φ22	0.53	30/35/0.2	0.175	1.15°	[21]
HL-1M	12×25	0.48	30/50/0.15	0.35	1.5°	[22]
TEXTOR	23×48	0.36	55/88/10	0.22	0.95°	[23]
JT-60	12×27	0.4	75/35/10	0.28	1.1°	[24]
HL-2A	φ17.4	0.49	55/25/2	0.21	1°	[25]
TFTR	12×43	0.6	120/70/2	0.23	1°	[26]

On the Large Helical Device (LHD) at the National Institute for Fusion Science (NIFS), both positive and negative NBI systems are equipped. The beam divergence of the positive ion beam is 1.1°. On the other hand, the ion beam divergence angle of the N-NBI system is less than 0.29° [27]. The small divergence angle of the negative ion beam is not only because of the low negative ion temperature, but also attributed to the low current density. From Table 1-1, it can be found that the typical positive ion beam current density is around 200 mA/cm^2. The current density of a negative ion beam extracted from a negative ion source for N-NBI is around 30 mA/cm^2 [27]. Therefore,

the space charge effect of negative ion beam is one order lower than that of positive ion beam. The divergence of the negative ion beam due to space charge is lower.

Owning to the low divergence angle of negative ion beam, it is possible to design the long beam path for the beam line, and this is beneficial to reduce neutron flux and of magnetic strength from torus.

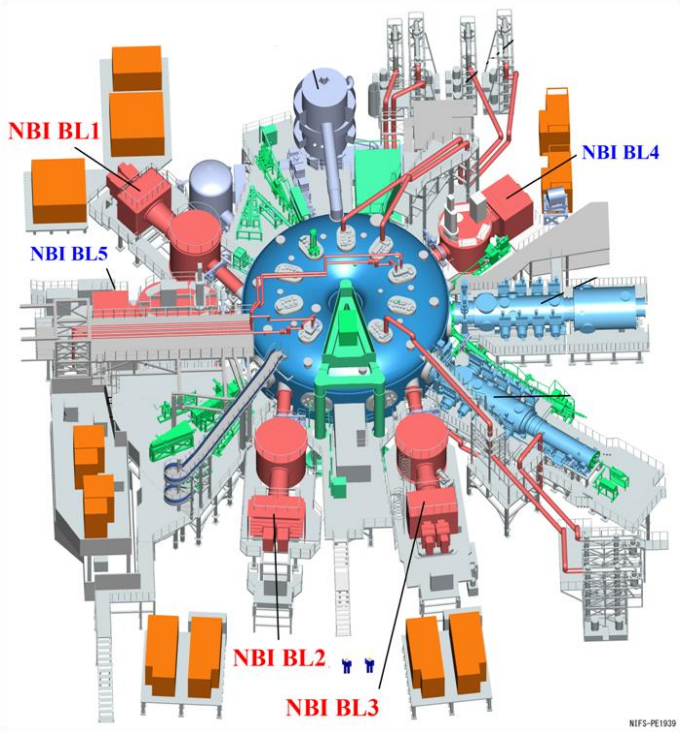

Figure 1-7. Beam line configuration of LHD

The N-NBI system has been used in LHD [28] and JT-60U [29] due to its advantages in neutralization efficiency at the beam energy more than 100 keV and beam divergence. It will also play an essential role in plasma heating and current drive for ITER [30]. The N-NBI systems have contributed remarkable achievements for LHD. As shown in Figure 1-7, LHD is equipped with 5 beam lines (BL). Beam lines 1, 2 and 3 are N-NBI and BL 4 and 5 are positive ion-based NBI (P-NBI). Two negative ion sourced are installed on each beam line. By optimizing caesium (Cs) dose rate and beam control, the injection power by the three N-NBI beam lines has reached and kept 15 MW as shown in Figure

1-8. The injection power and H- ion current density are presented in Figure 1-9. The maximum injection power per beam line has reached 6.9 MW and the current density of H- ions has achieved 340 A/m^2 which exceeded ITER NBI requirement on beam current density.

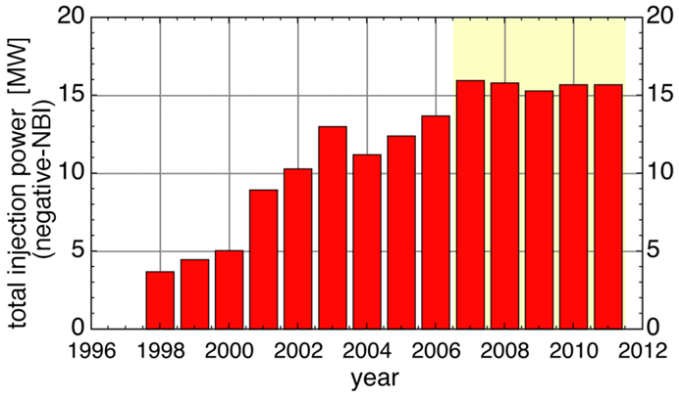

Figure 1-8. Total injection power of N-NBI systems on LHD

At Japan Atomic Energy Agency (JAEA), an arc-driven negative ion source was applied for the NBI beam line of JT-60SA. The beam energy reached 0.5 MeV. The maximum beam current depended on the beam duration which was 32 A at 1 s of beam duration and decreased to 15 A at 100 s of beam duration. Correspondingly, the beam current was 189 A/m^2 and 89 A/m^2 at 1 s and 100 s of beam duration, respectively. The maximum beam duration was 100 s [31].

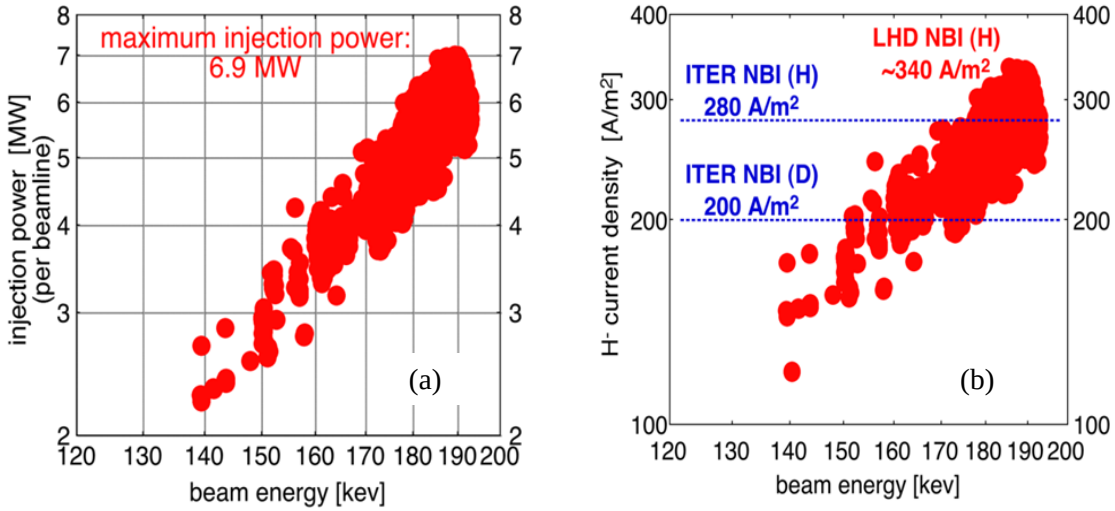

Figure 1-9. Injection power (a) and current density (b) of LHD-NBI per beam line

1.3 Basis of negative hydrogen ion source

The early application of H^- ions was to double the particle energy in a DC particle accelerator, which is called "tandem accelerator". According to this concept, an H^- ion is accelerated from ground (0 V) to high positive potential (+V) which is sustained by an electrode. At the electrode, incoming H^- ions are converted to protons through thin film by stripping two electrons. The protons are accelerated from high positive potential (+V) to ground (0 V). Finally, a beam with energy which is twice of applied DC voltage on the acceleration electrode can be obtained [32]. The schematic illustration of this concept is shown in Figure 1-10.

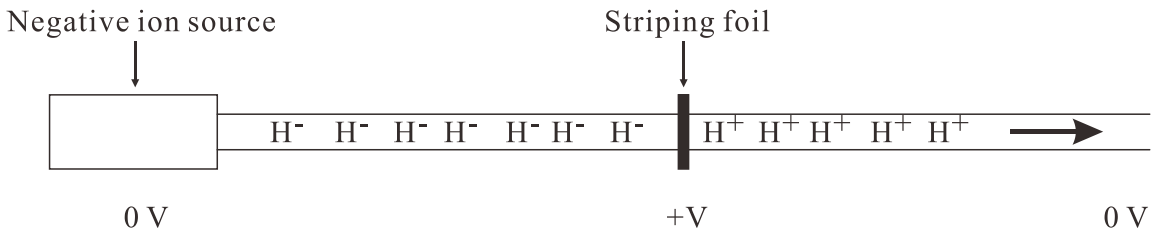

Figure 1-10. Schematic illustration of energy doubling in a DC accelerator

The advantages of using negative ions in an accelerator are not only to double the final energy of the particles. In a cyclotron, because H^- ions are converted to protons, the Lorentz force applied to the particles changes its direction. As a consequence, the extraction of the accelerated beam becomes much simpler [33]. Over the past decades, a variety of negative ion sources have been applied to many accelerators for various purposes [34]. The research of negative hydrogen ion source oriented to NBI systems of fusion reactors started from 1970s. So far, the negative-ion-based NBI system has become indispensable equipment for the advanced fusion reactor.

Of course, a question listed at the top is how to produce H^- ions in a negative ion source. The H^- ion production mechanisms can be classified to two types: (1) volume process and (2) surface process.

1.3.1 Volume process

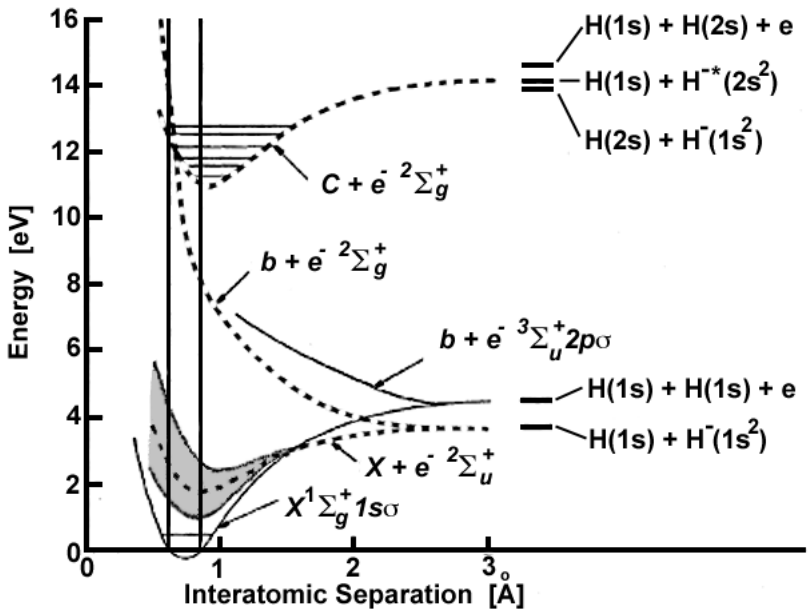

Figure 1-11. Schematic illustration of potential energy curve for H_2 and H_2^-

In pure hydrogen plasma, H^- ions are produced mainly though the process of dissociative attachment (DA) of electrons to vibrationally excited H_2 molecules. Experimental investigations have been conducted by G. J. Schulz and D. Rapp in order to measure the cross section of DA in the process of electron colliding with vibrationally excited H_2 molecules in 1s-1s state at low electron energy [35,36]. In this process, an electron is temporarily captured to the H_2 molecule and an intermediate H_2^- state is formed. The lifetime of this H_2^- state is only ~10^{-15} s and then a decay process occurs with production of a neutral hydrogen atom and a negative hydrogen ion as described as following,

$$H_2(X\,^1\Sigma_g^+ 1s\sigma) + e \rightarrow H_2^-(X + e^{-2}\Sigma_u^+) \rightarrow H + H^- . \qquad (1\text{-}7)$$

This process is schematically demonstrated in Figure 1-11. The cross section for the reaction has a maximum value 1.6 × 10^{-21} cm^2 or 2.8 × 10^{-21} cm^2 (depending on the choice of the data) [37] at electron energy of 3.75 eV which is the threshold energy for the formation of H^- ions, since at incident electron energy lower than 3.75 eV, the reverse

auto-detachment is very possible and compound system can decay to the ground or a higher vibrational state by emitting an electron [36].

In 1979, a drastic increase of the DA cross sections have been found theoretically and experimentally when H_2 molecules are in either vibrationally or rotationally excited states [38,39]. An impressive phenomenon is that the cross sections increase by four orders of magnitude for excited H_2 molecules from the vibrationally excited state $v'' = 0$ to $v'' = 4$. Table 1-2 shows the cross sections of DA process for H_2 molecules in vibrationally excited states $v'' = 0$ to $v'' = 9$ calculated by Wadehra [38].

Table 1-2. Dissociative attachment cross sections near thresholds for H_2 molecules at vibratinally excited states v'' = 0 to v'' = 9 [38].

v''	Electron energy [eV]	Cross section [cm^2]
0	3.75	2.8×10^{-21}
1	3.23	8.3×10^{-20}
2	2.75	1.0×10^{-18}
3	2.29	7.5×10^{-18}
4	1.86	3.8×10^{-17}
5	1.46	1.2×10^{-16}
6	1.08	2.9×10^{-16}
7	0.74	4.3×10^{-16}
8	0.42	3.2×10^{-16}
9	0.14	4.3×10^{-16}

Since the cross sections for DA process are enhanced much if H_2 molecules are in vibrationally or rotationally excited states, the main mechanism to produce H^- ions in pure hydrogen plasma can be considered as the process of dissociative attachment of electrons to excited H_2 molecules. This is a two-step process [40] : (1), Production of vibrationally and rotationally excited H_2 molecules $H_2^*(v'')$ and (2), Formation of H- ions by dissociatively attaching low energy electrons to $H_2^*(v'')$ molecules, as described as follows:

$$H_2 + e \rightarrow H_2^*(v'') + e\,, \tag{1-8}$$

$$H_2^*(v'') + e \rightarrow H^- + H\,. \tag{1-9}$$

In Allan's experiments, the dependence of vibrationally excited states of H_2 molecules on electron energy has been investigated [39]. If electron energy is lower than 5 eV, H_2 molecules at ground electronic state are excited to vibrational states up to v'' = 4 by the collisions between electrons and H_2 molecules. The formation of H^- ions in this process is

$$H_2(X^1\Sigma_g^+ 1s\sigma, v'') + e(< 5eV) \rightarrow H_2^*(X^1\Sigma_g^+ 1s\sigma, v''+\Delta v'') + e, \quad (1\text{-}10)$$

$$H_2^*(X^1\Sigma_g^+ 1s\sigma, v'') + e(< 1eV) \rightarrow H^- + H. \quad (1\text{-}11)$$

In 1979, Bacal has measured H^- ion density using photodetachment technique in arc discharge plasmas. The result showed that the H^- ion density reached as high as 30% of positive ion density at optimized arc condition and pressure [41]. The reactions described in Equation 1-10 and 1-11 were the main processes for the formation of H^- ions [40,41] in this experiment. However, in Equation 1-10, the most possible value for $\Delta v''$ is $\Delta v'' = \pm 1$, and a higher vibrational state is difficult to reach [42]. In order to obtain the population of H_2 molecules in higher vibrationally excited states, collisions of H_2 molecules in ground vibrational state with energetic electrons are required. The processes for the formation of H^- ions involving in energetic electrons are [42,43]

$$H_2(X^1\Sigma_g^+ 1s\sigma, v'' = 0) + e(> 20eV) \rightarrow H_2^*(B^1\Sigma_u^+ 2p\sigma, C^1\Pi_u 2p\pi, \ldots) + e, \quad (1\text{-}12)$$

$$H_2^*(B^1\Sigma_u^+ 2p\sigma, C^1\Pi_u 2p\pi, \ldots) \rightarrow H_2^*(X^1\Sigma_g^+ 1s\sigma, v'') + h\nu, \quad (1\text{-}13)$$

$$H_2^*(X^1\Sigma_g^+ 1s\sigma, v'') + e(\sim 1eV) \rightarrow H^- + H. \quad (1\text{-}14)$$

H_2 molecules in ground electronic state are excited to high electronic states including all members of singlet electronic states (B, C …) as indicated by line 1 in Figure 1-12. The singlet states then decay to ground electronic state with a photon emission, but in higher vibrational states as indicated by line 2 in Figure 1-12. H^- ions are then produced when low energy electrons are attached to the highly vibrationally excited H_2 molecules. The cross section is large if electron energy is around 1 eV [38]. In a negative hydrogen ion source, H^- ions produced through volume production mechanism are mainly generated from the H_2 molecules in high vibrational states ($v'' > 4$) [42]. The process in Equation 1-12 is effective if the electron energy is higher than 20 eV and the cross sections reach maxima at incident electron energy of about 40 eV [44].

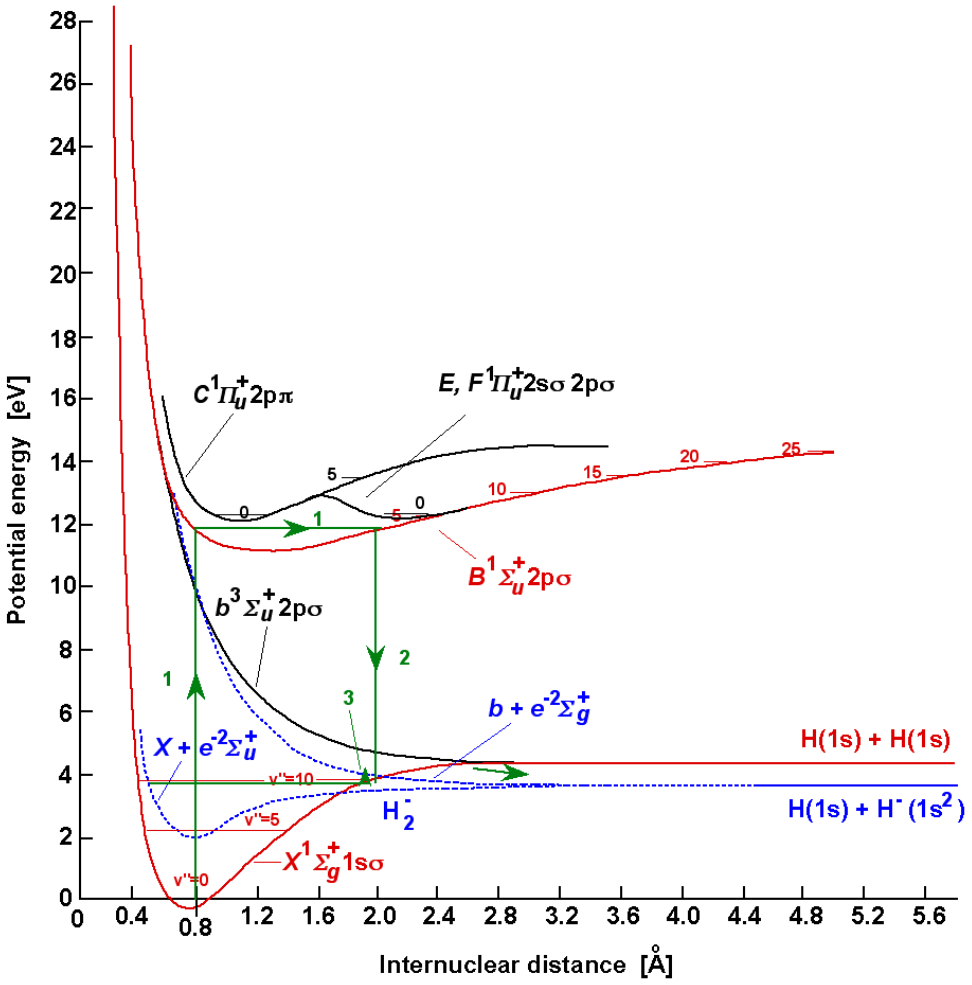

Figure 1-12. Potential energy curves for H_2 and H_2^- in different states.

According to the mechanism of volume process for producing H^- ions, in order to obtain intense H^- ions in the ion source, requirements can be summarized as follows briefly:

(1). Energetic electrons (20-40 eV) are necessary to obtain large cross sections to excite H_2 molecules to high vibrational states.

(2). Low energy electrons (~1 eV) are necessary to obtain large cross sections for DA process of electrons to excited H_2 molecules ($v'' > 4$).

(3). Electron affinity of an H^- ion is 0.754 eV. Electron with energy higher than 1 eV can destroy H^- ion through the electron detachment (ED) process

$$H^- + e(>1eV) \rightarrow H + 2e\,. \tag{1-15}$$

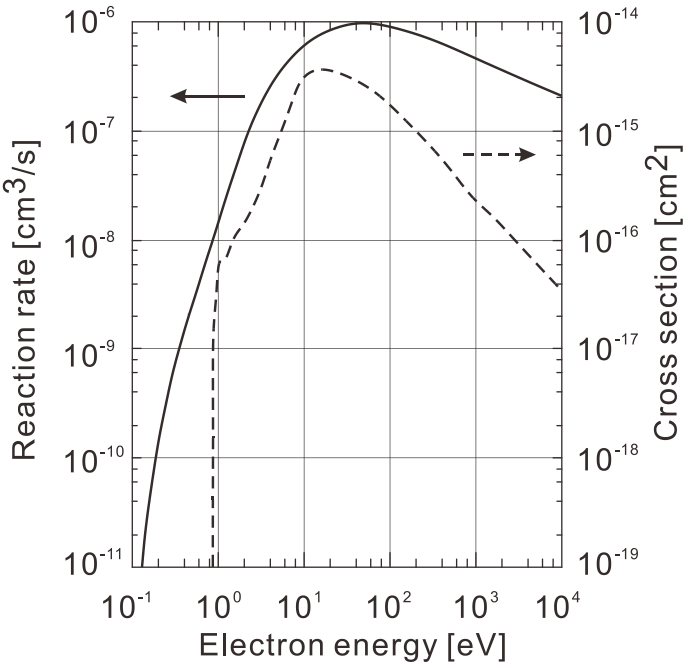

Figure 1-13. Cross section and reaction rate for ED process of H^- ions vs. electron energy.

The cross section and reaction rate for ED process has been shown in Figure 1-13 [45]. The cross section increases drastically when the electron energy is higher than 1 eV. Therefore, it is necessary to keep the electron energy lower than 1 eV to minimize losses of H^- ions.

A negative hydrogen ion source should have the ability of producing plasma with energetic electrons in order to maximize the production of excited H_2 molecules ($v'' > 4$). In addition, low energy electrons are required to reduce the destruction of H^- ions. Satisfying these requirements, the concept of "tandem-type ion source" has been widely used by the negative hydrogen ion sources for NBI systems.

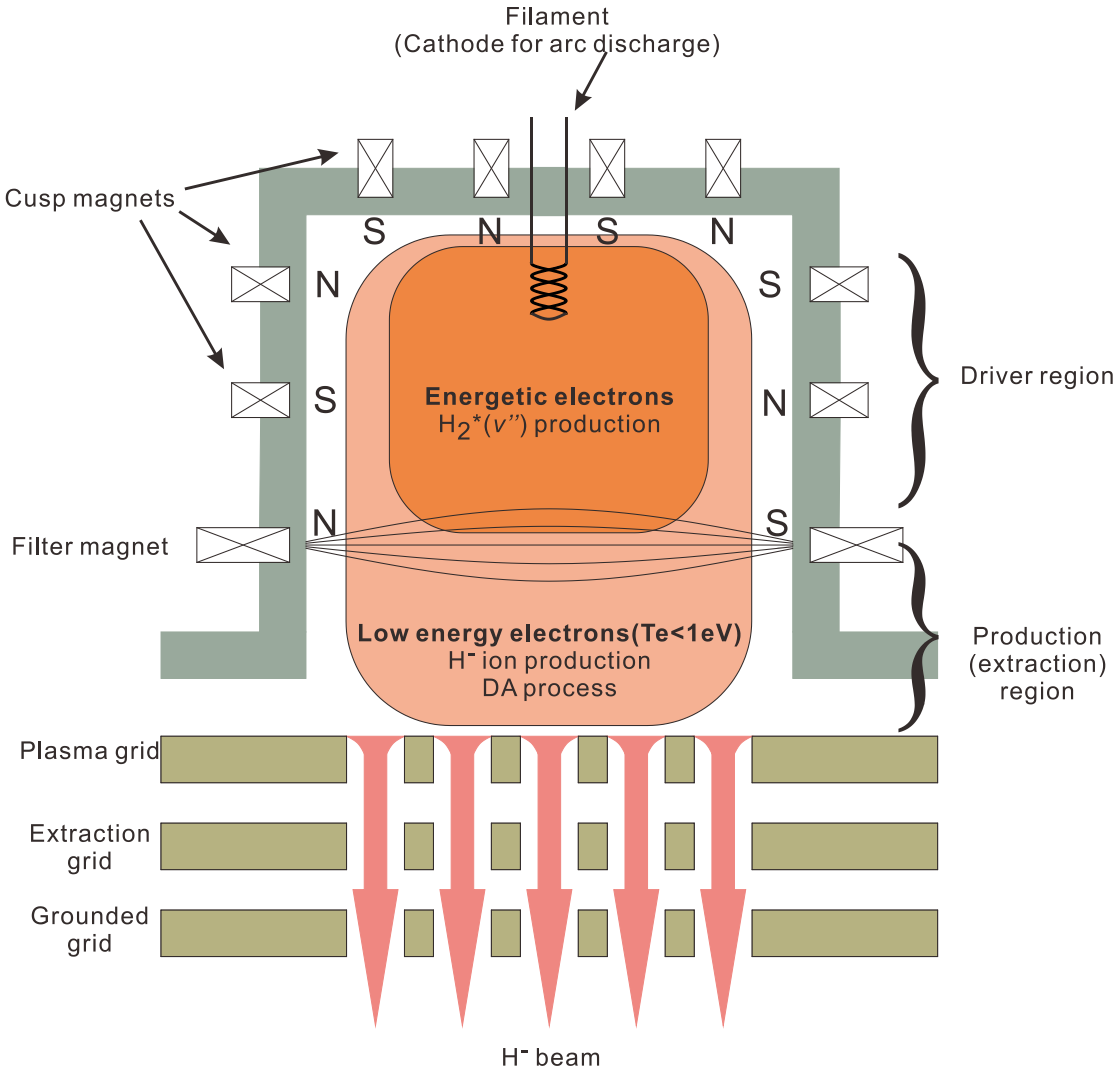

Figure 1-14. Schematic illustration of a volume production negative hydrogen ion source.

Figure 1-14 shows the schematic illustration of a "tandem-type" volume production negative hydrogen ion source. A typical characteristic of the ion source is the application of filter magnetic field which divides the ion source into a driver region and an extraction/production region. In the driver region, plasma is generated by filament-arc discharge. Primary electrons emitted from the hot filaments has energy high enough to excite H_2 molecules to high vibrational states ($v'' > 4$). The filter magnetic field plays a role of barrier for the primary electrons to prevent them from directly flowing from the driver region to the extraction/production region [30]. Energetic electrons are trapped into the filter magnetic field, diffuse across the filter field and experience collisions with

other particles. As a consequence, electrons lose their energy and are thermalized. Low temperature electrons (T_e < 1 eV) can be obtained in the extraction/production region for the production of H^- ions through DA process. H^- ions are mainly concentrated in the extraction/production region in which the DA process is effective and losses of H^- ions by ED reaction are minimized. Sufficient H^- current can be obtained by volume process. However, H_2 gas load is too high and not acceptable for practical N-NBI .

1.3.2 Surface process

Production of H^- ions through so-called surface process is the main mechanism for the present negative hydrogen ion sources applied to NBI systems for fusion experimental devices. A significant improvement in the negative ion production has been achieved by seeding a small amount of Cs into the negative ion source [46]. This has been shown that the production of H^- ions is dominated by surface processes on the wall of the negative ion source [47]. In the surface processes, H^- ions are emitted from the metal surface with low work function in the process of (1), energetic hydrogen atoms (H) impacting with the wall and being bounced back to the plasma with capturing an additional electron and (2), positive ions (H^+, H_2^+ and H_3^+) impacting with the wall and being emitted back as H^- ions [18,48].

If an H atom has enough energy higher than the work function of the metal-wall surface, the yield of H^- ions depends on the energy of incident atoms. Experiments by Lee and Seidl have shown that the maximum yield is as high as 25% for an H atom temperature of 5 eV with Cs covered Mo surface [49]. The dependence of H^- ion yield on the energy of incident H atom is shown in Figure 1-15.

If the incident particles are enrgetic positive ions, the yield of H^- ions is also denpends on the energy of the positive ions. Experiments by M. Seidl et al. have demostrated that a saturation in H^- yield can be found for a Cs covered Mo surface with work function of 1.5 eV [50]. The threshold energy for the saturation is ~15 eV as shown in Figure 1-16.

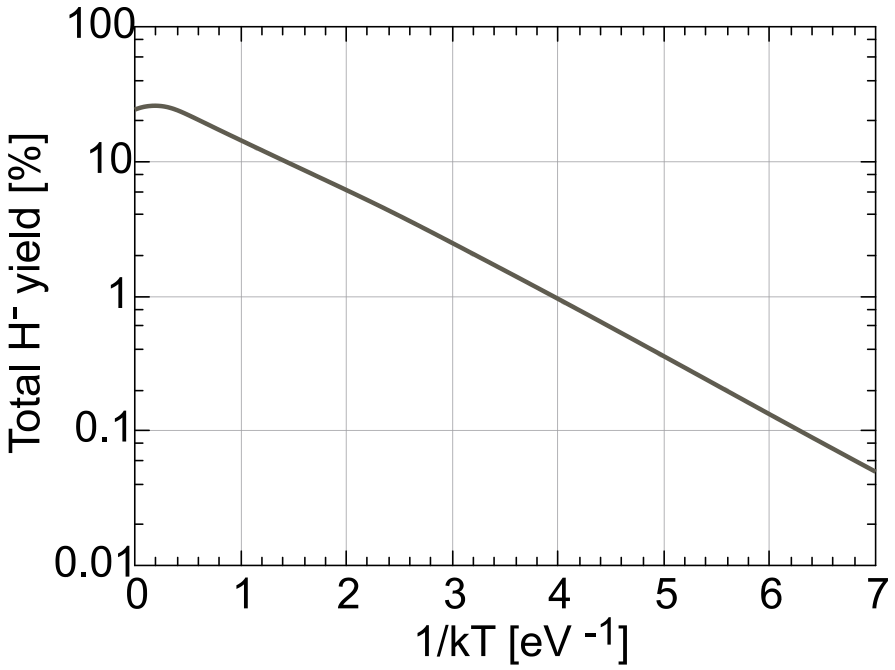

Figure 1-15. Depenced of H^- ion yeild on the energy per incident H atoms [49].

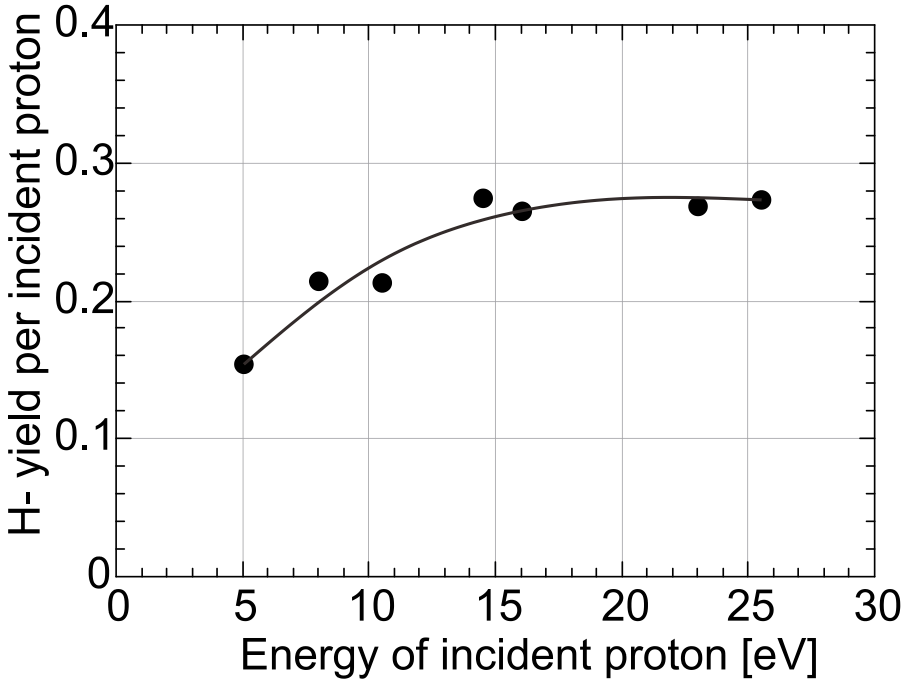

Figure 1-16. Dependence of H^- ion yield on the incident energy per nucleus [50].

In order to produce H^- ions the backscattered particles need to capture electrons from the atoms of the surface. The probabilty of H^- ion production denpends on the work function of the metal surface and decrease with the increasing work function significantly [18]. However, the electron affinity of H^- in interaction-free condition is only ~0.754 eV. On the other hand, the work function of refactory metals, such as tangsten and molybdenium, used in dense plasma exceeds 4 eV (for tungsten: 4.55 eV and for molybdenum: 4.6 eV) [43]. In order to produce H^- ion effectively through surface process, it is essential to reduce the work function of the metal surface.

Generally, the work function of the metal surface can be decreased by covered with low work function materials such as alkaline earth atoms. The work function of the metal surface covered with alkaline atoms can be lower than the work function of the substrate. In all the potential materials, caesium (Cs) has the lowest work function which is only 2.1 eV. Therefore, Cs has been chosen for negative hydrogen ion sources applied for NBI systems.

The work function of the metal surface depends on the Cs coverage. As shown in Figure 1-17, schematically, the work function of the Mo surface decreases with the increasing Cs coverage. The minimum work function appears at Cs coverage of 0.6 monolayes for the (110) face of a single Mo crystal. When the Cs coverage is higher than 1 monolayer, the work function is up to about 2.1 eV [18,51] and approaches to the work function of Cs metal. The behavior of work function dependence on the Cs coverage has been observed in the experiments [52] as shown in Figure 1-18. The work function of clean W (110) surface is measured as 5.1 eV and decreases initially toward the minimum value 1.45 eV with around half a monolayer Cs. Further Cs coverage increases the work function to 2.15 eV. The conversion efficiency of H^+ ions to H^- ions is also shown in Figure 1-18 Corresponding to the minimum work function, the maximum conversion efficiency can be found.

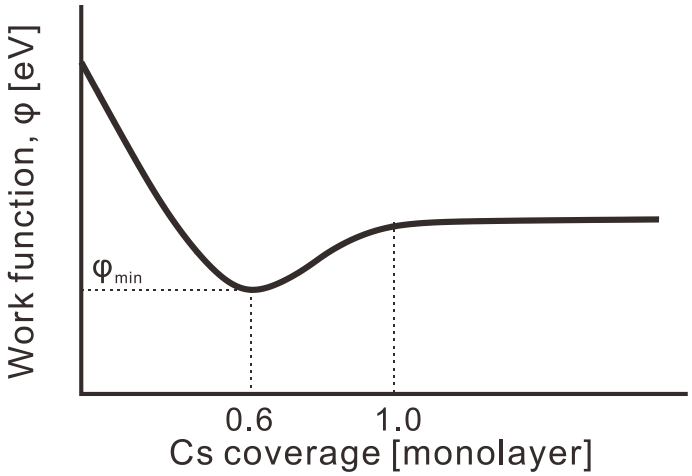

Figure 1-17. Dependence of work function of Cs covered Mo surface on the thickness of Cs layer.

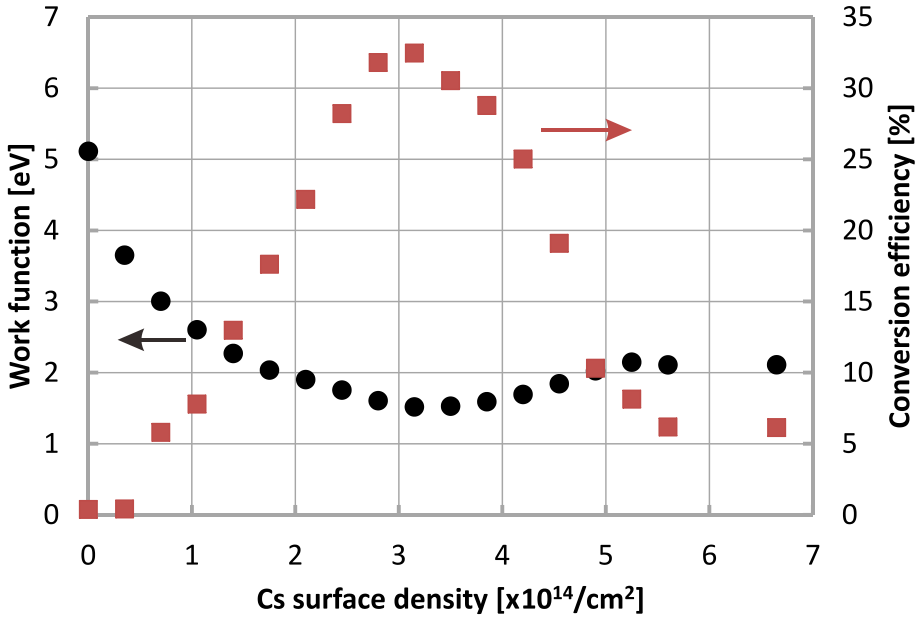

Figure 1-18. Dependence of surface work function for the (110) face and H^- ion conversion efficiency on the surface density of deposited Cs [52].

An optimum Cs condition exists due to the existence of minimum work function for the surface production of H^- ions. It is possible to reach to the optimum Cs condition in a negative hydrogen ion source from the engineering point of view, because the ionic characteristic is partially included in the half a monolayer Cs on W and Mo metals. Due to the ionic characteristic, the binding energy between the Cs and those metals are much

stronger than the metallic bond of Cs-Cs. Overmuch Cs atoms on the metal surface can be sputtered into the chamber by the energetic particles in plasmas or evaporated by controlling the temperature of the metal surface.

1.3.3 A brief review of the negative ion sources used for NBI systems

In order to produce dense H^- ions, regular hydrogen plasma should be generated in the ion source. In principle, all kinds of discharge producing large area plasma can be used, including:

(1), Arc discharge

(2), Radio frequency (RF) discharge

(3), Electron cyclotron resonance (ECR) discharge

(4), Magnetron glow discharge

(5), Microwave discharge

Various kinds of negative ion sources have been developed for NBI systems. In a charge exchange ion source, it has been reported that by using a 1.5 keV 200 mA D^+ ion beam which is extracted from a multi-aperture ion source, passing through Cs vapor, a 50 mA D^- beam has been obtained [53]. Because of the disadvantages of polluting the beam line by Cs vapor, large beam divergence angle and difficulty in matching with accelerator system, this type of ion source was not used since 1980s. The magnetron type negative ion source was historically the first negative ion source. The H^- ion current increased from several milliampere to 880 mA by seeding Cs into the ion source [54,55]. In 1980s, a type of multicusp surface production ion source has been developed [56]. This ion source has been improved by replacing the Cs-coated copper surface by a pure Ba surface at the end of 1980s [57]. The developments of volume production negative ion sources were accelerated after the enhancement of DA process of electrons to the high vibrationally exited H_2 molecules was found [39,41] and the application of filter

magnetic field [58]. In 1990, a 3.4 A H^- ion beam was obtained in the volume production negative ion source at JAEA with H_2 pressure of 2.1 Pa [59]. However, this ion source was not enough for a NBI system since the high operational pressure and low H^- ion current density which was 13 mA/cm^2. The performance of this type of ion source has been increased significantly by seeding a small amount of Cs in to the ion source following the experiments of Leung [60].

With the considerations of high power (several ten kilowatts), stability of the plasma and robustness of the ion source, only arc-discharge-driven and RF-discharge-driven ion source have been used for NBI systems in present. So far, 34 mA/cm^2 H^- ion beams have been achieved in the arc-discharge-driven ion source for LHD-NBI at NIFS. At JAEA, the H^- ion beam extracted from an arc-discharge-driven ion source reached 18.9 mA/cm^2. In IPP Garching, an RF-driven negative ion source has been developed oriented to the application of NBI systems of ITER. The H^- ion current density has reached 35 mA/cm^2 with 4 s beam extraction [61].

1.4 Objective of present work

In a negative hydrogen ion source, electrons, H^- ions and positive ions exist in the beam extraction region. By applying extraction voltage, both H^- ions and electrons are extracted since H^- ions and electrons have the same charge polarity. The extracted H^- ions are the required particle for the beam used for N-NBI. On the other hand, the extracted electrons, named co-extracted electrons are unnecessary and have to be removed from the beam. A deflection magnetic field is applied to the extraction grid to suppress electrons near the plasma grid and deflect the co-extracted electrons [62]. The co-extracted electrons are mainly absorbed by the extraction grid. Consequently, the extraction grid has to suffer additional heat load bringing by the co-extracted electrons.

In the experiments on NIFS Research and Development Negative Ion Source (NIFS-RNIS), it has been observed that H^- ion density decrease by applying extraction voltage and meanwhile electron density increase in the beam extraction region. This

phenomenon indicates that H^- ions are partially replaced by the electrons flowing from the driver region during beam extraction [63]. Therefore, the ratio of H^- ion density to electron density decreases. The ratio of accelerated current to the extraction current then also decreases. The efficiency of the negative ion source can be increased if the H^- ion density is possible to be kept constant and additional incoming electrons are possible to be suppressed during beam extraction. The detailed transport dynamics in negative ion source is unknown and has not been measured yet. In order to know the mechanism, it is necessary to understand the magnetic structure in the beam extraction region, response of charged particles to electrostatic field, diffusion type of electron and positive ions and movements of electrons, positive and negative ions. The present work is an experimental study on the charged particle dynamics of the negative-ion-rich plasma in the extraction region, aiming at the understanding of the extraction process of H^- ions. Some suggestions to increase the efficiency of the negative ion source are expected from results of this work.

1.5 Structure of thesis

The present work is organized in the following way in this thesis as illustrated in Figure 1-19. In chapter 2, NIFS-RNIS is introduced. The structure of the magnetic field, which plays an important role in plasma profile and plasma flow, is demonstrated and discussed. Diagnostic methods used for this work including Langmuir probe, photodetachment and cavity ring-down are briefly summarized. A new method to calculate the local absolute H^- ion density is introduced in detail. In chapter 3, results obtained by the diagnostics introduced in chapter 2 are put forward. The conversion of normal plasma to negative-ion-rich plasma, the effect of Cs, the effect of external parameters, plasma profile and effect of extraction field are discussed. Basic characteristics of NIFS-RNIS are summarized. In order to measure the charged particle flow, methods of a directional Langmuir probe (DLP) and DLP with photodetachment are applied to the experiments. They are described in chapter 4. In this chapter, the one-dimensional charged particle flow is shown and discussed. Ambipolar movement and

drift dominate the flow. H^- ion temperature obtained in the experiments can help the discussion for the production of H^- ions. In chapter 5, the two-dimensional flow patterns of charged particles are put forward. The two-dimensional charged particle flows are used to understand the phenomena of plasma profile due to the extraction field. Origin and termini of the charged particle are also discussed. Some suggestions are proposed for the improvement of the present negative ion source.

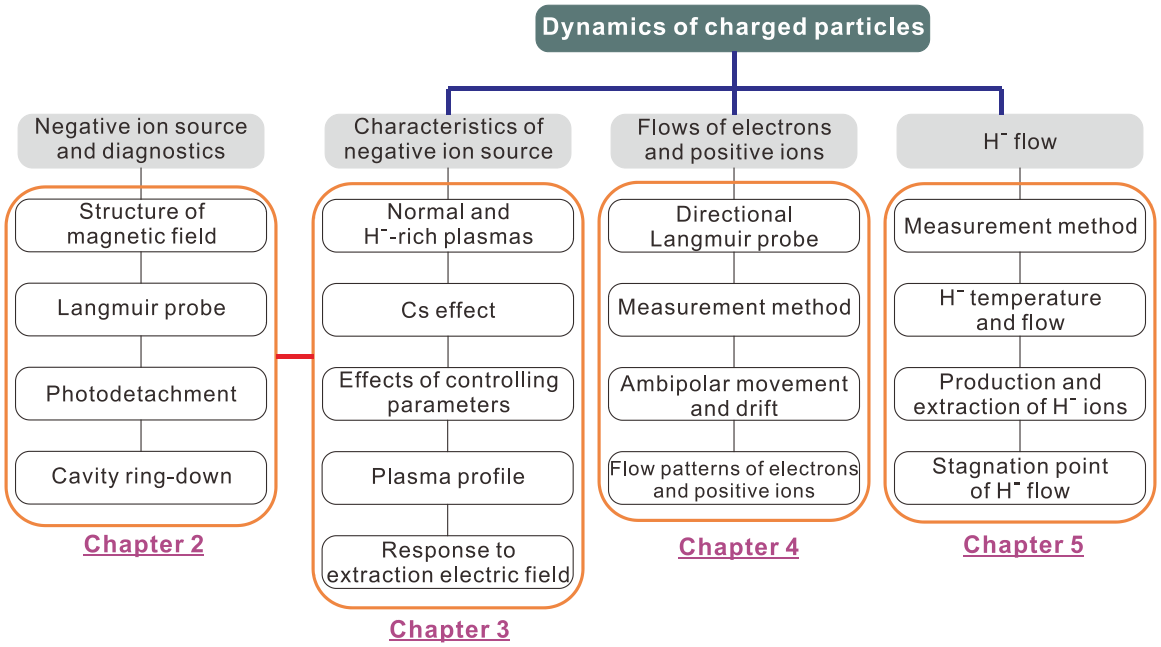

Figure 1-19. Structure of thesis.

References

[1] J. J. Kraushaar and R. A. Ristinen, *Energy and the Environment* (New York, NY: Wiley & Sons Inc, 2006).

[2] W. B. Arthur, Sci. Am. **262,** 92 (1990).

[3] C. J. Campbell and J. H. Laherrère, Sci. Am. **278,** 60 (1998).

[4] R. Vandenbosch and S. E. Vandenbosch, *Nuclear waste stalemate: Political and scientific controversies* (University of Utah Press, 2007).

[5] P. H. Yamada, in *Handbook of Climate Change Mitigation*, edited by W.-Y. Chen, J. Seiner, T. Suzuki, and M. Lackner (Springer US, 2012).

[6] J. Wesson and D. J. Campbell, *Tokamaks* (OUP Oxford, 2011).

[7] D. Post and R. Pyle, in *Atomic and Molecular Physics of Controlled Thermonuclear Fusion*, edited by C. J. Joachain and D. E. Post (Springer US, 1983), p. 477.

[8] B. B. Kadomtsev, F. S. Troyon, M. L. Watkins, P. H. Rutherford, M. Yoshikawa, and V. S. Mukhovatov, Nucl. Fusion **30,** 1675 (1990).

[9] A. Gibson and J. E. T. Team, Phys. Plasmas **5,** 1839 (1998).

[10] W. S. Cooper, Phys. Fluids B **4,** 2300 (1992).

[11] T. Oikawa, Y. Kamada, A. Isayama, T. Fujita, T. Suzuki, N. Umeda, M. Kawai, M. Kuriyama, L. R. Grisham, Y. Ikeda, K. Kajiwara, K. Ushigusa, K. Tobita, A. Morioka, M. Takechi, T. Itoh, and JT-60Team, Nucl. Fusion **41,** 1575 (2001).

[12] F. M. Levinton, Rev. Sci. Instrum. **63,** 5157 (1992).

[13] B. W. Rice, D. G. Nilson, and D. Wróblewski, Rev. Sci. Instrum. **66,** 373 (1995).

[14] S. R. Cortes, N. C. Hawkes, P. Lotte, C. Fenzi, B. C. Stratton, J. Hobirk, R. D. Angelis, F. Orsitto, C. a. F. Varandas, and C. t. t. E.-J. w. Program, Rev. Sci. Instrum. **74,** 1596 (2003).

[15] W. Jing, Y. Lieming, Z. Jianhua, H. Xiaoyu, and L. Wenzhu, Plasma Sci. Technol. **14,** 953 (2012).

[16] K. H. Berkner, R. V. Pyle, and J. W. Stearns, Nucl. Fusion **15,** 249 (1975).

[17] M. Kuriyama, N. Akino, N. Ebisawa, L. Grisham, H. Liquen, A. Honda, T. Itoh, M. Kawai, M. Kazawa, K. Mogaki, Y. Ohara, T. Ohga, K. Ohmori, Y. Okumura, H. Oohara, K. Usui, and K. Watanabe, Journal of Nuclear Science and Technology **35,** 739 (1998).

[18] I. G. Brown, *The Physics and Technology of Ion Sources* (John Wiley & Sons, 2004).

[19] J. R. Coupland, T. S. Green, D. P. Hammond, and A. C. Riviere, Rev. Sci. Instrum. **44,** 1258 (1973).

[20] S. Geng, K. Tsumori, H. Nakano, M. Kisaki, K. Ikeda, M. Osakabe, K. Nagaoka, Y. Takeiri, M. Shibuya, and O. Kaneko, Rev. Sci. Instrum. **87,** 02B103 (2016).

[21] T. Obiki, A. Sasaki, F. Sano, and K. Uo, Rev. Sci. Instrum. **52,** 1445 (1981).

[22] S. F. Jiang, C. P. Zhou, D. T. Wang, D. L. Lu, H. S. Wang, G. J. Lei, H. J. Li, C. J. Zhang, B. Dai, W. J. Gao, T. Jiang, J. Q. Zhang, and E. Y. Wang, in *HL-1M Neutral Beam Injection Systemand Preliminary NB Heating Experiments*, 26th EPS Conference on Controlled Fusion and Plasma Physics, Maastricht, Netherlands 1999.

[23] R. Uhleman, H. Euringer, and M. Lochter, in *Fusion technology 1988*; *Vol. 1* (Elsevier Science Publishers B. V., Amsterdam, The Netherlands, 1989), p. 636.

[24] M. Akiba, M. Araki, H. Horiike, T. Ito, M. Kawai, M. Kuriyama, S. Kitamura, S. Matsuda, M. Matsuoka, H. Mukaida, Y. Oguchi, Y. Ohara, T. Ohga, H. Ohtsuki, Y. Okumura, K. Shibanuma, T. Shibata, H. Shirakata, and S. Tanaka, Rev. Sci. Instrum. **53,** 1864 (1982).

[25] G. J. Lei, S. F. Jiang, G. W. Zhong, J. Y. Cao, D. L. Lu, G. Q. Zou, H. Liu, X. M. Zhang, T. Jiang, J. F. Yang, J. M. Qian, L. X. Tang, C. P. Zhou, W. C. Mao, and Y. Liu, Chinese Physics C **32,** 271 (2008).

[26] J. A. Paterson, C. F. Chan, M. Y. Fong, G. W. Koehler, and J. S. Sullivan, in *Mechanical Baseline Design of the Common Long Pulse Source for the Neutral Beam Systems of TFTR, Doublet III-D, and MFTF-B*, Proceedings of 11th Symposium of Fusion Engineering, Austin, Texas, 1985.

[27] T. Kuroda, Fusion Eng. Des. **36,** 143 (1997).

[28] Y. Takeiri, O. Kaneko, K. Tsumori, Y. Oka, M. Osakabe, K. Ikeda, E. Asano, T. Kawamoto, and R. Akiyama, Rev. Sci. Instrum. **71,** 1225 (2000).

[29] M. Kawai, L. Grisham, T. Itoh, M. Kazawa, M. Kuriyama, K. Mogaki, Y. Okumura, and K. Watanabe, Rev. Sci. Instrum. **71,** 755 (2000).

[30] J. P. Boeuf, B. Chaudhury, and L. Garrigues, Phys. Plasmas **19,** 113509 (2012).

[31] M. Hanada, A. Kojima, H. Tobari, R. Nishikiori, J. Hiratsuka, M. Kashiwagi, N. Umeda, M. Yoshida, M. Ichikawa, K. Watanabe, Y. Yamano, and L. R. Grisham, Rev. Sci. Instrum. **87,** 02B322 (2016).

[32] L. W. Alvarez, Rev. Sci. Instrum. **22,** 705 (1951).

[33] K. Prelec and T. Sluyters, Rev. Sci. Instrum. **44,** 1451 (1973).

[34] D. P. Moehs, J. Peters, and J. Sherman, IEEE Trans. Plasma Sci. **33,** 1786 (2005).

[35] D. Rapp, T. E. Sharp, and D. D. Briglia, Phys. Rev. Lett. **14,** 533 (1965).

[36] G. J. Schulz and R. K. Asundi, Phys. Rev. **158,** 25 (1967).

[37] G. J. Schulz and R. K. Asundi, Phys. Rev. Lett. **15,** 946 (1965).

[38] J. M. Wadehra and J. N. Bardsley, Phys. Rev. Lett. **41,** 1795 (1978).

[39] M. Allan and S. F. Wong, Phys. Rev. Lett. **41,** 1791 (1978).

[40] M. Kikuchi and M. Azumi, *Frontiers in Fusion Research II: Introduction to Modern Tokamak Physics* (Springer, 2015).

[41] M. Bacal and G. W. Hamilton, Phys. Rev. Lett. **42,** 1538 (1979).

[42] M. Bacal, Nucl. Fusion **46,** S250 (2006).

[43] M. Bacal and M. Wada, Applied Physics Reviews **2,** 021305 (2015).

[44] J. R. Hiskes, J. Appl. Phys. **70,** 3409 (1991).

[45] R. K. Janev, W. D. Langer, K. J. Evans, and D. E. J. Post, *Elementary Processes in Hydrogen-Helium Plasmas: Cross Sections and Reaction Rate Coefficients* (Springer Science & Business Media, 2012).

[46] S. R. Walther, K. N. Leung, and W. B. Kunkel, J. Appl. Phys. **64,** 3424 (1988).

[47] K. N. Leung, S. R. Walther, and W. B. Kunkel, Phys. Rev. Lett. **62,** 764 (1989).

[48] M. Bacal, Rev. Sci. Instrum. **79,** 02A516 (2008).

[49] B. S. Lee and M. Seidl, Appl. Phys. Lett. **61,** 2857 (1992).

[50] M. Seidl, H. L. Cui, J. D. Isenberg, H. J. Kwon, B. S. Lee, and S. T. Melnychuk, J. Appl. Phys. **79,** 2896 (1996).

[51] A. Simonin, J. Bucalossi, C. Desgranges, M. Fumelli, C. Jacquot, P. Massmann, J. Pamela, D. Riz, R. Trainham, and Y. Belchenko, Rev. Sci. Instrum. **67,** 1102 (1996).

[52] J. N. M. Van Wunnik, J. J. C. Geerlings, E. H. A. Granneman, and J. Los, Surf Sci. **131,** 17 (1983).

[53] J. E. Osher, F. G. Gordon, and G. W. Hamilton, in *Production of intense negative ion beams*, Ion Sources: Proceedings of the Second International Conference on Ion Sources, 1972, p. 876.

[54] Y. I. Belchenko, G. I. Dimov, and V. G. Dudnikov, Nucl. Fusion **14,** 113 (1974).

[55] B. Wolf, *Handbook of Ion Sources* (CRC Press, 1995).

[56] K. W. Ehlers and K. N. Leung, Rev. Sci. Instrum. **51,** 721 (1980).

[57] C. F. A. v. Os, P. W. v. Amersfoort, and J. Los, J. Appl. Phys. **64,** 3863 (1988).

[58] K. N. Leung, K. W. Ehlers, and M. Bacal, Rev. Sci. Instrum. **54,** 56 (1983).

[59] M. Hanada, T. Inoue, H. Kojima, Y. Matsuda, Y. Ohara, Y. Okumura, K. Watanabe, and M. Seki, Rev. Sci. Instrum. **61,** 499 (1990).

[60] K. N. Leung, C. A. Hauck, W. B. Kunkel, and S. R. Walther, Rev. Sci. Instrum. **60,** 531 (1989).

[61] U. Fantz, B. Heinemann, D. Wünderlich, R. Riedl, W. Kraus, R. Nocentini, and F. Bonomo, Rev. Sci. Instrum. **87,** 02B307 (2016).

[62] L. M. Lea, A. J. T. Holmes, M. F. Thornton, and G. O. R. Naylor, Rev. Sci. Instrum. **61,** 409 (1990).

[63] K. Tsumori, H. Nakano, M. Kisaki, K. Ikeda, K. Nagaoka, M. Osakabe, Y. Takeiri, O. Kaneko, M. Shibuya, E. Asano, T. Kondo, M. Sato, S. Komada, H. Sekiguchi, N. Kameyama, T. Fukuyama, S. Wada, and A. Hatayama, Rev. Sci. Instrum. **83,** 02B116 (2012).

2. Configuration of the negative ion source and diagnostics

The plasma in positive ion source is generated in “field free” region surrounded with multi-cusp field near the chamber walls and the field strength is reduced at beam extraction region to obtain homogeneous beam distribution. On the other hand, relatively strong magnetic field is necessary for negative ion source to reduce the energy of electrons diffused from the plasma-generation region to extraction region, the vicinity of plasma grid. That is because H^- ions are easily destructed via collision with the electrons with high energy. Additional magnetic field is required to sweep co-extracted electrons and to absorb them onto extraction grid. Linear combination of those magnetic fields forms complicated magnetic field in the extraction region. The structure of the magnetic field changes in a small negative ion source and NIFS R&D negative ion source (NIFS-RNIS), whose cross-sectional structure is the same on the short side of the source and the long side is a half height of the ion source for LHD NBI, is applied for the experiments. Most of the important events occur in the beam extraction region and measurements have been conducted for the plasma in the extraction region. The configurations of the RNIS including the geometry and magnetic field are described in this chapter. A Langmuir probe, photodetachment technique and cavity ring-down were used for the diagnostics of the plasma in the extraction region. The methods are described as well as a new approach to determine the absolute H^- ion density at a specific point.

2.1 Introduction

A high power ion source is required for producing dense plasma and high density H^- ions. LHD-NBI systems use filament-arc-driven ion sources to produce H^- ion beam. The filament-arc-driven ion sources have advantages of simple structure, reliability , easy to control, robustness and low cost of power supply systems. The experiments in this

thesis were carried out on the NIFS-RNIS which has a half size of the ion sources applied for LHD-NBI, and is installed on the test-stand [1]. As a fundamental diagnostic tool, a Langmuir probe was applied to measure basic plasma parameters including electron temperature (T_e), electron density (n_e) and plasma potential (V_s) etc. However, it is difficult to measure the H^- ion density by a Langmuir probe since electrons and H^- ions have the same charge, and identifying H^- ion component from the probe current is very sophisticated. Therefore, cavity ring-down (CRD) method, which is a kind of laser absorption spectroscopy technique, was applied to measure the line-averaged H^- ion density [2]. The regular CRD method is not enough to measure the H^- ion density locally. Photodetachment technique with a DC biased Langmuir probe has been then utilized. Photodetachment current is proportional to the local H^- ion density. By combining the photodetachment technique and CRD method, a new approach to estimate the absolute local H^- ion density was proposed.

2.2 Configuration of the ion source

In an N-NBI system, the H^- ions are produced and extracted from source plasma. An ion source to generate plasma is installed at the most upstream of the N-NBI. Figure 2-1 shows the schematic cross-sectional view of the NIFS-RNIS. The ion source is a bucket ion source with a pair of filter magnet, which induces transversal magnetic field in the source. The discharge chamber has dimensions of 350 mm in width (x direction), 226 mm in depth (z direction) and 700 mm in length (y direction, not shown in Figure 2-1). Therefore, the ion source has the ability of producing large volume plasma.

As discussed in Chapter 1, the ion source is divided into a “driver region” and an “extraction region” by a filter magnetic field. High density plasma is produced in the driver region by filament-arc discharge. Power supplies to heat the filaments and drive the arc discharge are applied to produce the plasma. The electrical diagram connections for filament feeding, arc discharge and beam acceleration are schematically illustrated in Figure 2-2.

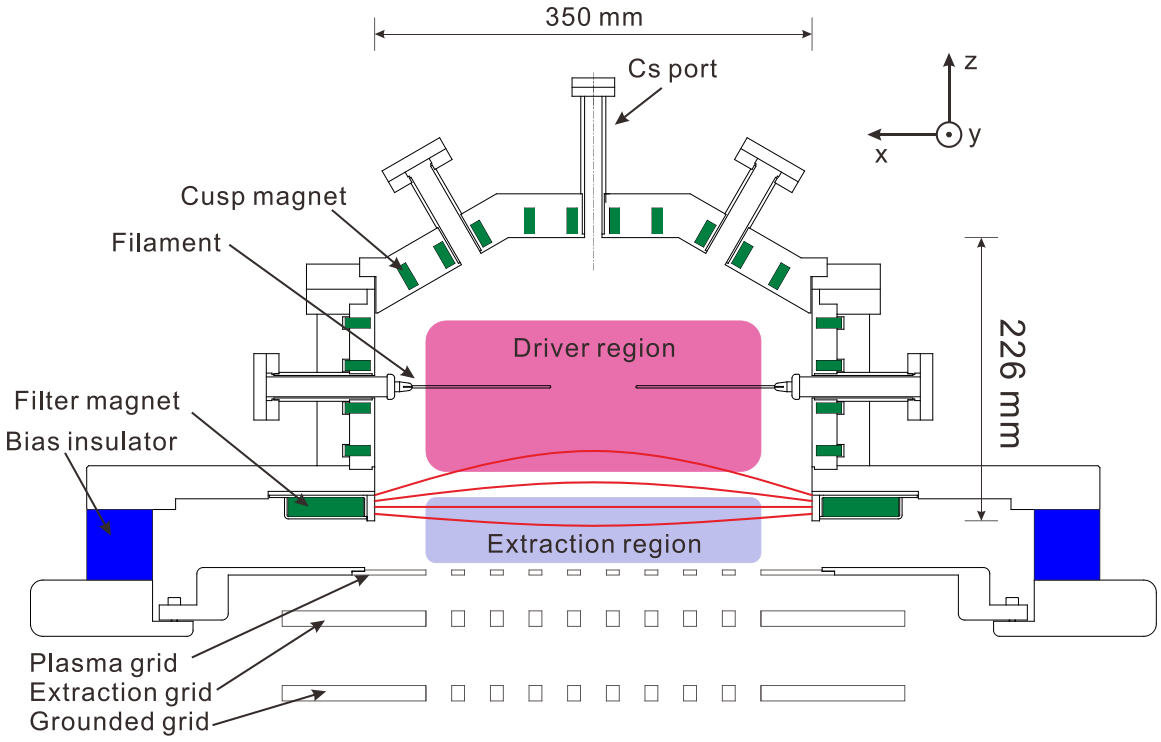

Figure 2-1. Corss-sectional view of the RNIS

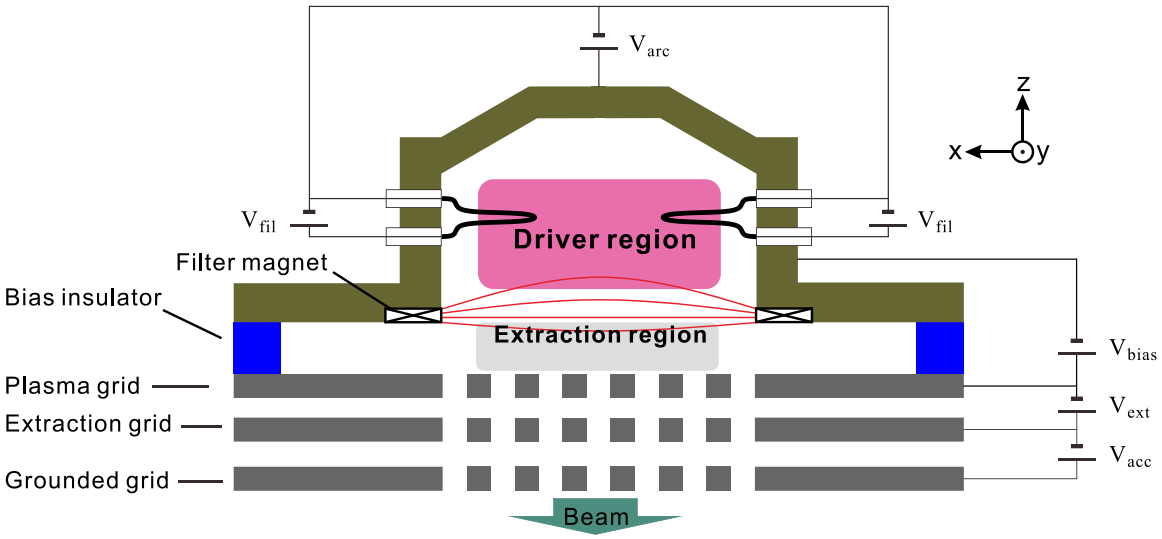

Figure 2-2. Electrical diagram of the ion source. V_{arc}: arc voltage; V_{fil}: filament voltage; V_{bias}: bias voltage; V_{ext}: extraction voltage; V_{acc}: acceleration voltage.

The RNIS is equipped with 12 filaments made of tungsten (W). Technically, three types of filament can be used for an arc-driven ion source: spring type (helical), hair-pin type and U-shape type. However, the discharge can be unstable in the cases of spring and U-shape filaments. Therefore, the hair-pin type filaments are preferable due to its advantages of stability of discharge, high arc efficiency and high uniformity of plasma [3]. The filaments are heated to about 3000 K by a filament power supply. The typical current transmits through a filament is 110 - 120 A, and the current is adjusted to whether the Cs is seeded or non-seeded in the H_2 plasma. Electrons, named primary electrons, are emitted from the hot filaments through thermionic emission. The primary electrons are accelerated by the arc voltage applied between the filaments and chamber wall and obtain energies. Collisions occur between the accelerated electrons and neutral particles (H_2 molecules and H atoms). Hydrogen plasma is produced through cascade collisions with electron-impact ionization processes.

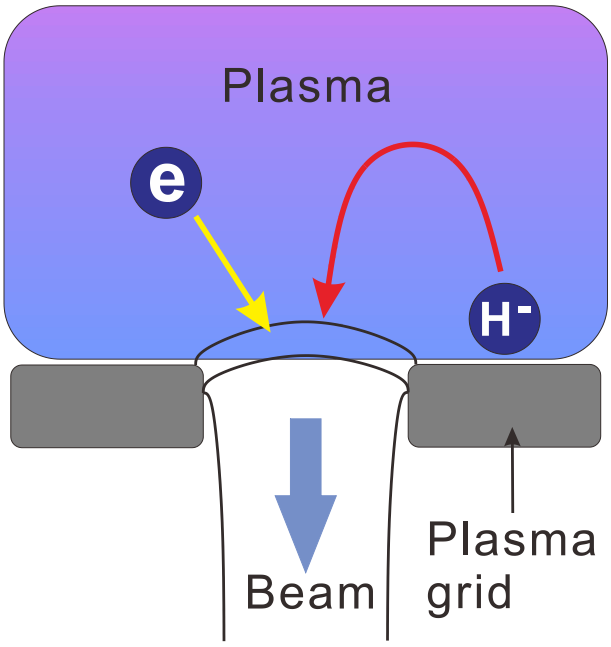

Figure 2-3. Extraction of a beam from the plasma boundary through an aperture of plasma grid.

The plasma grid works as a physical boundary between the plasma and the beam region. H^- ions are extracted from the plasma boundary through the apertures of the

plasma grid as schematically illustrated in Figure 2-3. On the RNIS, the plasma grid is electrically insulated from the arc chamber by a bias insulator. A positive bias voltage is applied to the plasma grid with respect to the arc chamber. This is an effective means to suppress the electrons in the extraction region to decrease the electron density and reduce the co-extracted electron current. There are two possible mechanisms for the suppression of electrons by the bias voltage: (1), positive ions are reflected by the bias voltage and consequently the density of electrons is reduced and (2), electrons in the extraction region are absorbed by the positively biased plasma grid [4].

In order to reduce the loss of the plasma in the bucket ion source to the wall, multicusp magnetic field is applied. On the RNIS, cusp magnets (permanent magnet bar, SmCo) are installed on the external surface of the plasma chamber as shown in Figure 2-1. The three-dimensional arrangement of the magnets is schematically illustrated in Figure 2-4. Multicusp magnetic field is generated inside the plasma chamber. The filaments are located in the field-free region ($B < 20$ G) in which large volume plasma exists. Surrounded by the multicusp magnetic field, the direct loss of the plasma to the chamber wall is suppressed and sustaining the high density plasma is possible. In the field-free region of the ion source, the uniformity of the plasma is improved. Figure 2-5 shows the magnetic field lines of the cusp field together with the filter magnetic field lines.

The filter magnetic field is also shown in Figure 2-5. The main function of the filter field is to decrease the temperature of electrons. The filter magnetic field with strength of around 60 G at the center suppresses the electrons diffusing from the driver region. Electrons have to travel across the filter field and are trapped into the filter field. In this process, electrons have long residence time in the filter field and experience several collisions with neutral particles and charged particles, transfer their energy to the neutral particles [5]. Electron temperature is decreased significantly and reaches low temperature ($T_e < 1$ eV) in the extraction region. This is essential for the negative ion source, since the rate coefficients of the DA processes are high with electron temperature ~1 eV [6] and the losses of H^- ions through electron detachment (ED) processes can be minimized if electron temperature is lower than 1 eV [7].

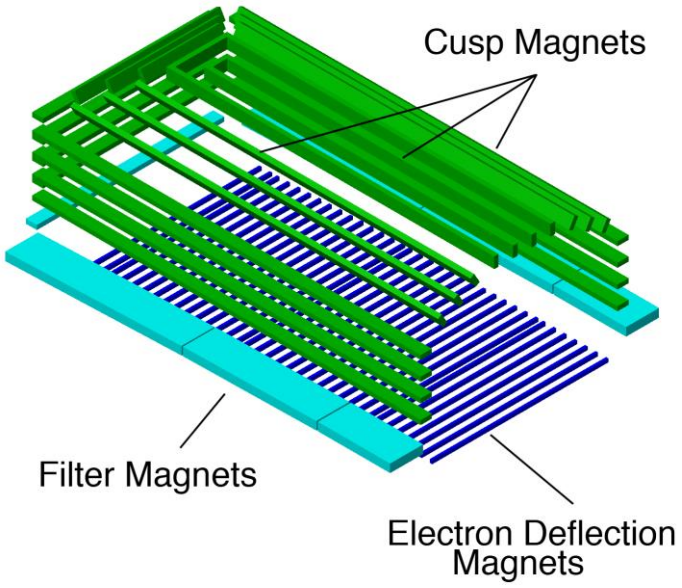

Figure 2-4. Three-dimensional illustration of magnet arrangement.

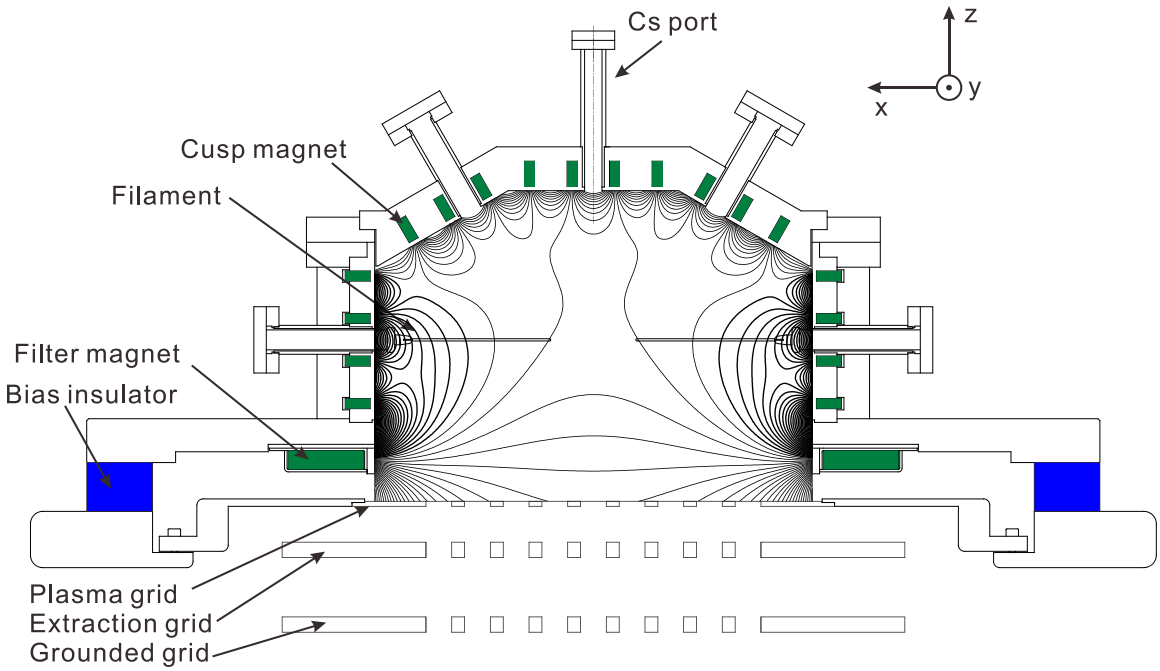

Figure 2-5. Multicusp field and filter lines in the RNIS.

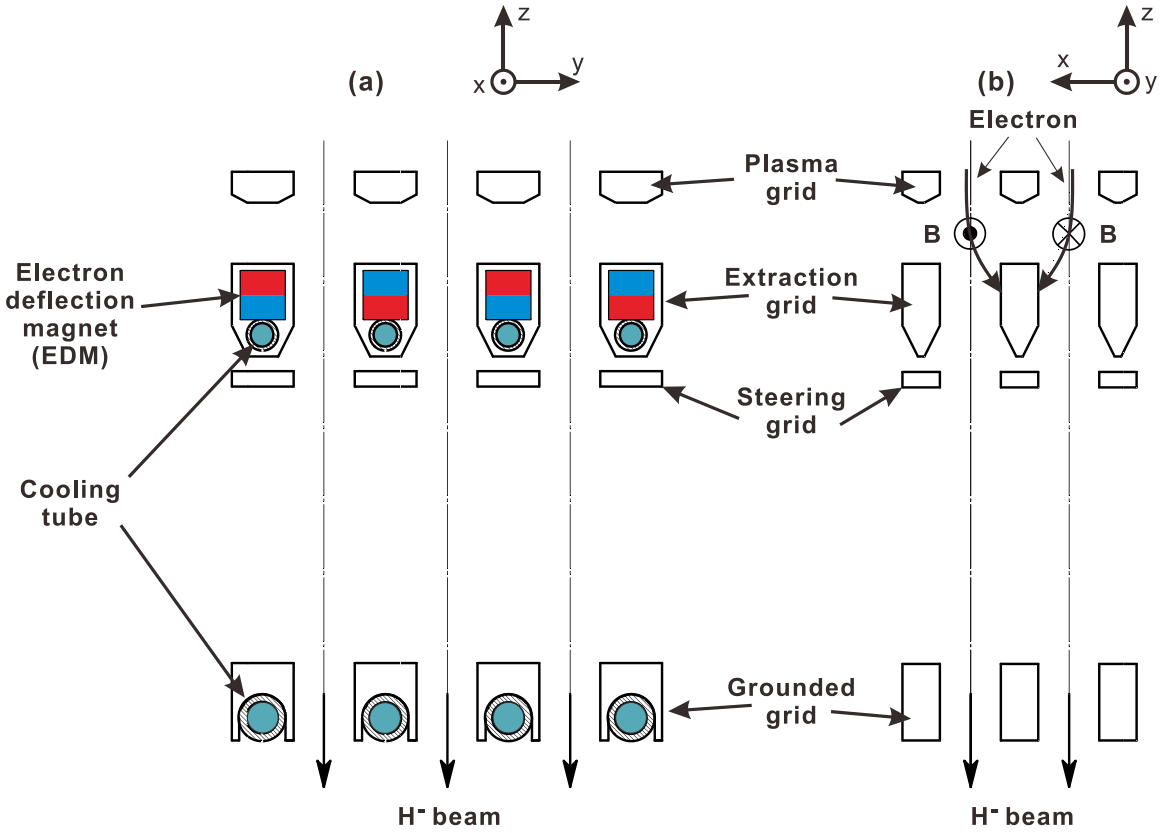

Figure 2-6. Schematic drawing of extraction and acceleration grid system of RNIS. (a) cross sectional view in y-z plane perpendicular to the electron deflection magnet bars and (b) cross sectional view in x-z plane parallel to the electron deflection magnet (EDM) bars [8].

If an extraction field is applied between the extraction grid and plasma grid, the extracted particles are not only H^- ions but also electrons since electrons have the same charge as H^- ions. The co-extracted electrons are useless for neutral beam and cause waste of power if they are accelerated. It is required to remove the electrons from the extracted particles. Because the electrons leaked into the acceleration gap can obtain more energies than that in the extraction gap, carry the heat load to the grounded grid and cause damages. A series of electron deflection magnets (EDM), whose polarities are alternated row by row, are embedded in the extraction grid as shown in Figure 2-6. The co-extracted electrons are deflected in the EDM field by Lorentz force. Absorbed by the extraction grid, the co-extracted electrons deposit heat load to the extraction grid. Because the mass of an H^- ion is 1836 times that of an electron, the deflection of H^- ion

beam is much lower than that of the co-extracted electron beam. H^- ions can pass through the extraction apertures.

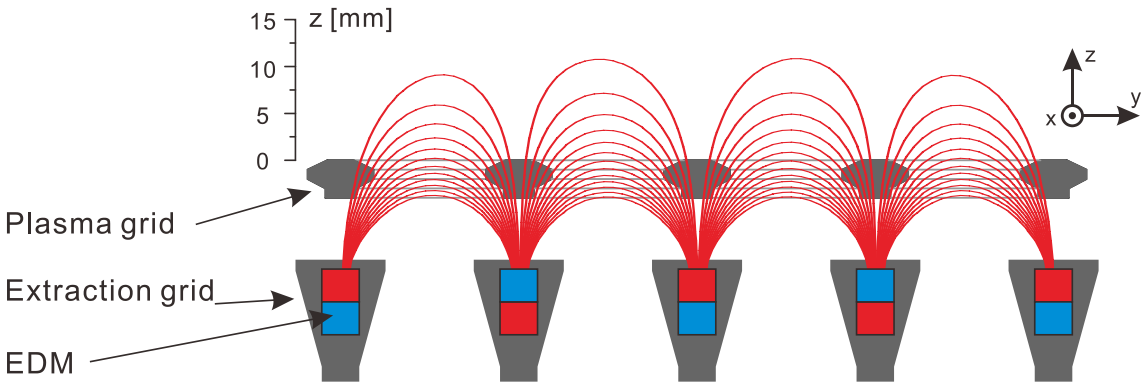

Figure 2-7. EDM field near the plasma grid.

The magnetic field generated by the EDM near the plasma grid is shown in Figure 2-7. The EDM field penetrates partially into the extraction region and forms loop-like region. Therefore, the EDM field suppresses the electron flux flowing to the aperture and reduces the current of co-extracted electrons, consequently. In addition, the profile of electron density is influenced by the EDM field due to the existence of cusp field near the plasma grid.

2.3 Single Langmuir probe

As a simplest means to probe the characteristics of plasma, the electrostatic measurement can be applied to obtain some basic plasma parameters, for example, electron density, electron temperature, plasma potential floating potential and so on. In this method, a small refractory, conducting material is inserted into the plasma. Since plasma consists of charged particles, the conducting material can collect a current by applying a potential to it. The measured current and potentials allow determining the properties of the plasma.

In 1920s Langmuir developed this electrostatic-probe method based on the small charge-collecting surface in the plasma. Therefore, the electrostatic-probe method is named “Langmuir probe”. A simplest single Langmuir probe consists of a wire enclosed into an insulator material such as a ceramic tube with a bared surface facing to the plasma. The part of the wire facing to the plasma also called “probe tip” suffers impact by the high speed particles in the plasma and can be heat up to high temperature. In order to avoid melt or evaporation, the probe tip should be made of refractory material such as tungsten (W). A schematic illustration of a single Langmuir probe is shown in Figure 2-8.

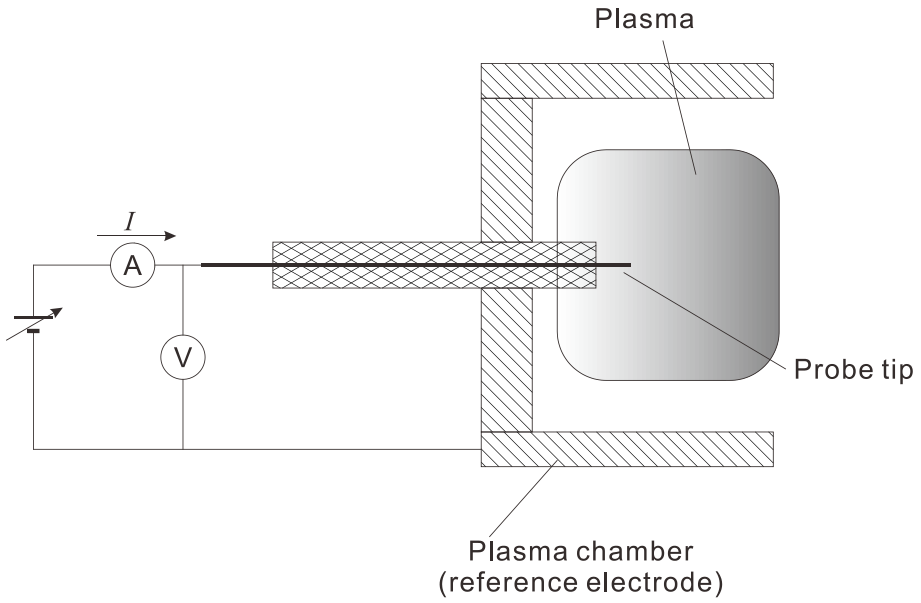

Figure 2-8. Schematic illustration of a single Langmuir probe

In the single Langmuir probe scheme shown in Figure 2-8, a variable power supply is applied to the probe. If the plasma is sustained stably, an *I*-*V* curve can be obtained by changing the voltage output of power supply. On the RNIS it is required to obtain the time evolution of the plasma parameters. This demand is satisfied by applying a sweeping voltage to the probe. The time evolutions of the probe current and voltage are recorded by an analog-to-digital converter (ADC) system and the data are stored in a computer. Whole the system is lifted on a high voltage stage and is insulated with an optical fiber to the ground for the purpose to obtain the signal during applying high voltage to the ion source. Figure 2-9 shows the typical single Langmuir probe scheme on

the RNIS. The probe is installed into the extraction region through the bias insulator. A 20 Hz sawtooth signal is generated by a function generator and transmitted to an amplifier. The output sweeping voltage -40 V – +40 V from the amplifier is applied to the single Langmuir probe through a sampling resistor. The voltage $V_{current}$ acquired from this resistor is used to determine the probe current by $I_p = V_{current}/R$, where R is the resistance of the sampling resistor for probe current and equal to 50 Ω. 1% of the amplifier output voltage is acquired from another sampling resistor and recorded as V_p'. Note that V_p' is not the real probe voltage. The real voltage applied to the Langmuir probe V_p should be subtracted from the output of the amplifier and calculated by $V_p = 100 \times V_p' - V_{current}$. The sweeping voltage applied to the single Langmuir probe and the corresponding probe current are shown in Figure 2-10.

The fundamental properties of the plasma including plasma potential, electron temperature, electron density and floating potential can be determined by the *I-V* curve of the single Langmuir probe.

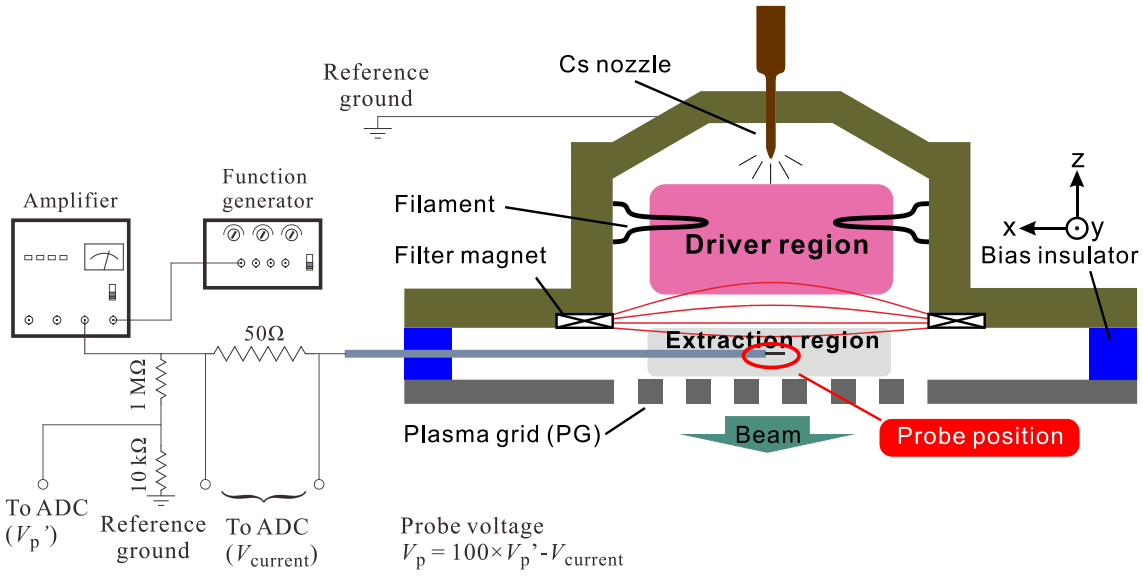

Figure 2-9. Single Langmuir probe installation on RNIS

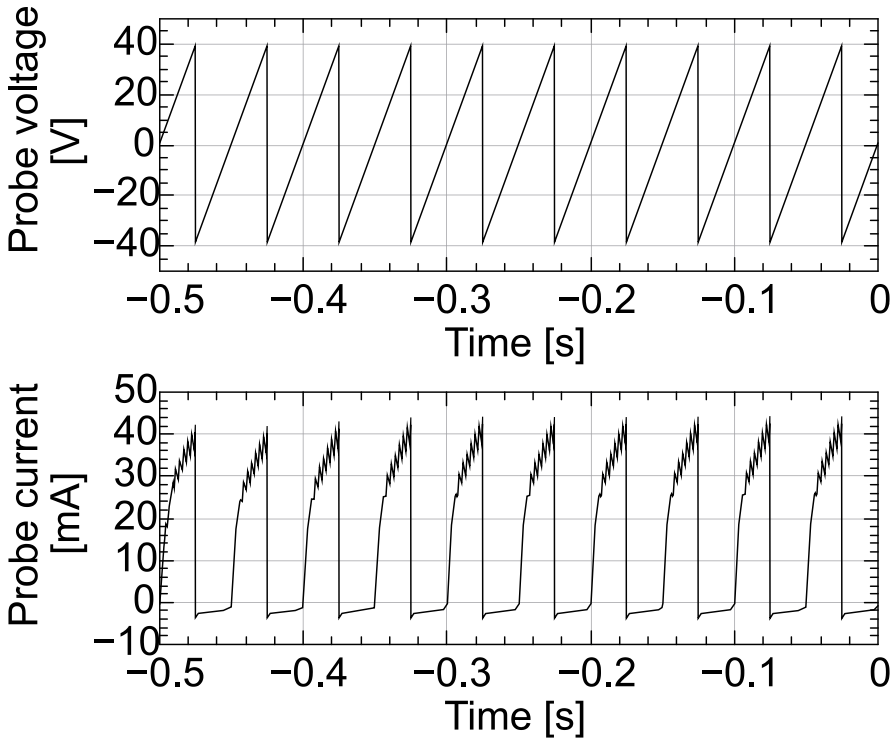

Figure 2-10. Time evolution of probe voltage and probe current. Note that the time 0 indicates the moment when the extraction voltage is applied.

2.3.1 Electron and positive ion saturation currents

Figure 2-11 shows a typical measured I-V curve obtained by the Langmuir probe on the RNIS in pure hydrogen plasma. When the probe is biased more negatively than the plasma potential V_s, the probe repels all the electrons are surrounded by an ion sheath. The probe collects positive ion flux from the plasma and gives a positive ion saturation current I_{is}. Ideally, I_{is} is independent of the probe voltage and a plateau can be found. Actually, the positive ion current increases slowly with decreasing probe voltage due to the expanding of the ion sheath, and the plateau is difficult to find. Therefore, the *y*-intercept of the linear fitting of the positive ion current is used to determine I_{is}. In Figure 2-11, I_{is} is estimated to be 1.7 mA.

In order to obtain the electron current I_e, it is necessary to subtract the positive ion current I_i from the probe current I_p, since $I_p = I_e + I_i$. Therefore, $I_e = I_p - I_i$. This can be

done by subtract the linear fitting function of positive ion current in Figure 2-11 from the probe current. The electron saturation current I_{es} and plasma potential can be determined from the semi-logarithmic plot of I_e as shown in Figure 2-12. The electron saturation current, I_{es}, is defined as the electron current at plasma potential V_s [9]. In order to find V_s, linear fittings are applied to the semi-logarithmic plot of I_e. The line A is the linear fitting of $\ln(I_e)$ at high probe voltages at which electron current saturates. The line B is the linear fitting of $\ln(I_e)$ at low probe voltage at which the electron current experiences a transition process from non-saturation region to saturation region. The probe voltage at the cross point of line A and line B is defined as V_s. Therefore, the extrapolation of line A at this cross point is defined as the electron saturation current I_{es} [9]. In Figure 2-12, the estimated I_{es} and V_s are 24.5 mA and 3.3 V, respectively.

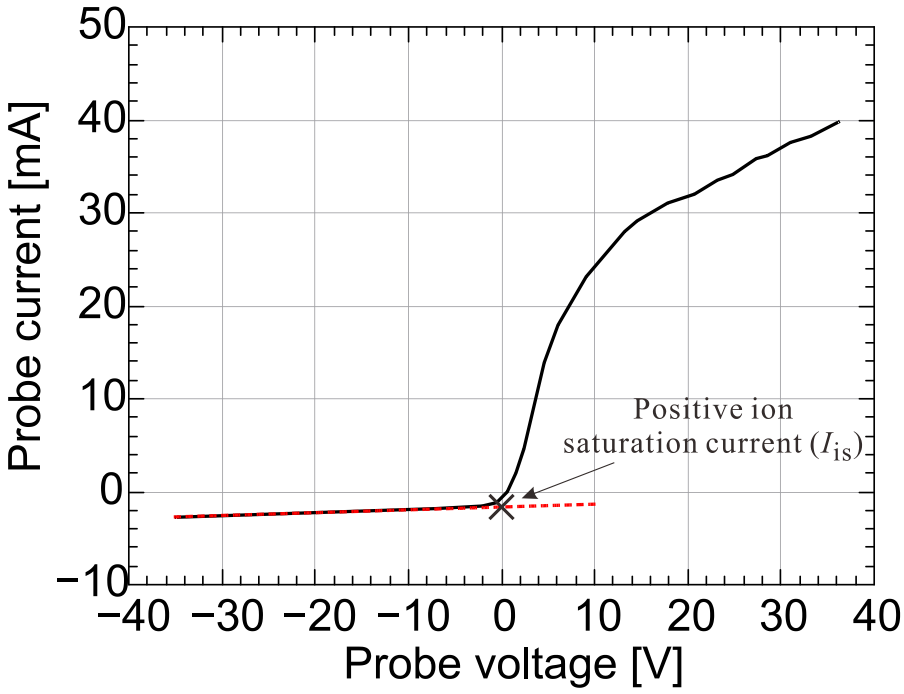

Figure 2-11. A typical *I-V* curve of single Langmuir probe. The positive ion saturation current I_{is} is defined by the *y*-intercept of the linear fitting of the positive ion current when the probe is negatively biased.

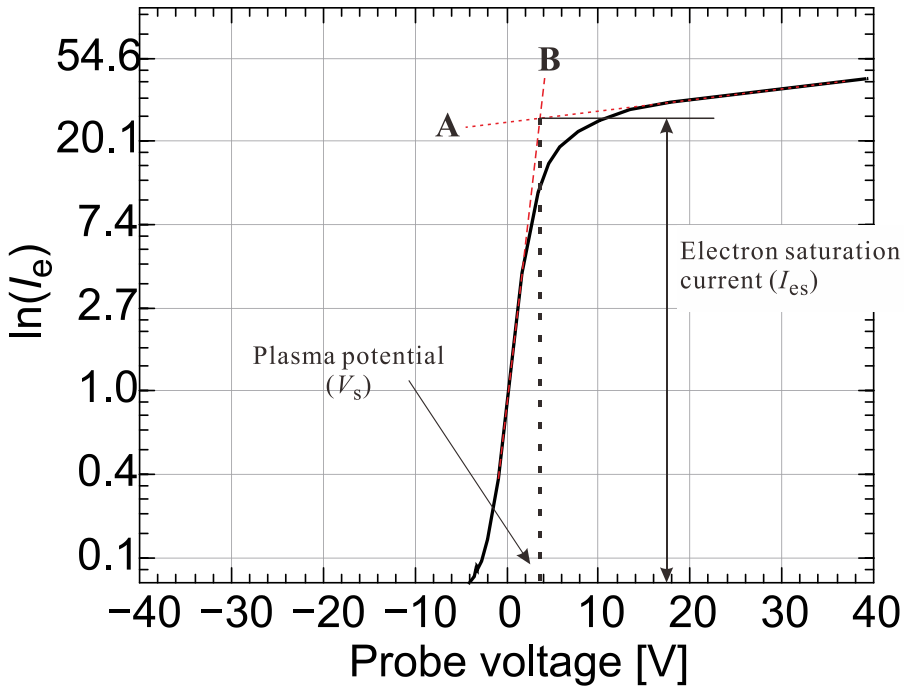

Figure 2-12. Semi-logarithmic plot of electron current I_e. Plasma potential V_s and electron saturation current I_{es} are defined.

2.3.2 Plasma potential

The plasma potential is defined as the cross point of line A and line B in Figure 2-12 described in Sec. 2.3.1.

2.3.3 Floating potential

One can image a floating object is located into the plasma. At stable condition, the object is at a potential at which the flux of positive ions to the surface of this object is equal to the flux of electrons. Therefore, the floating potential is defined as the zero-cross point of the probe *I-V* curve. At this point the electron current is equal to positive ion current and the probe current is 0. In the *I-V* curve shown in Figure 2-11, the floating potential is estimated to be 0.7 V.

2.3.4 Electron temperature

The electron current of the probe I_e in the transition region from non-saturation phase to saturation phase can be expressed as: [9]

$$I_e(V_p) = I_{es} \cdot \exp(\frac{-e(V_s - V_p)}{KT_e}), \quad (2\text{-}1)$$

where e donates the elementary charge.

It can be derived that

$$KT_e = \frac{d(eV_p)}{dI_e}. \quad (2\text{-}2)$$

The electron temperature KT_e is determined as the multiplicative inverse of the slope of line B in Figure 2-12. The electron temperature determined by the curve in Figure 2-12 is estimated to be 0.8 eV.

2.3.5 Electron density

The electron saturation current can be expressed as: [9]

$$I_{es} = \frac{1}{4} e n_e S_p \sqrt{\frac{8KT_e}{\pi m_e}}. \quad (2\text{-}3)$$

Where n_e donates the electron density, S_p donates the surface area of the probe tip and is 3.33794×10^{-6} m^2 for the example I-V curve shown in Figure 2-11, m_e is the mass of an electron. Since I_{es} is 24.5 mA and electron temperature KT_e is 0.8 eV, the electron density can be calculated to be 3.1×10^{17}/m^3.

2.4 Cavity ring-down

Cavity ring-down (CRD), also known as cavity ring-down laser absorption (CRLA), is an optical absorption technique which allows measuring the attenuation of light by absorption of samples and has been widely used to study the gaseous objects which absorb light at specific wavelengths. The line-averaged density of an object can be determined by CRD.

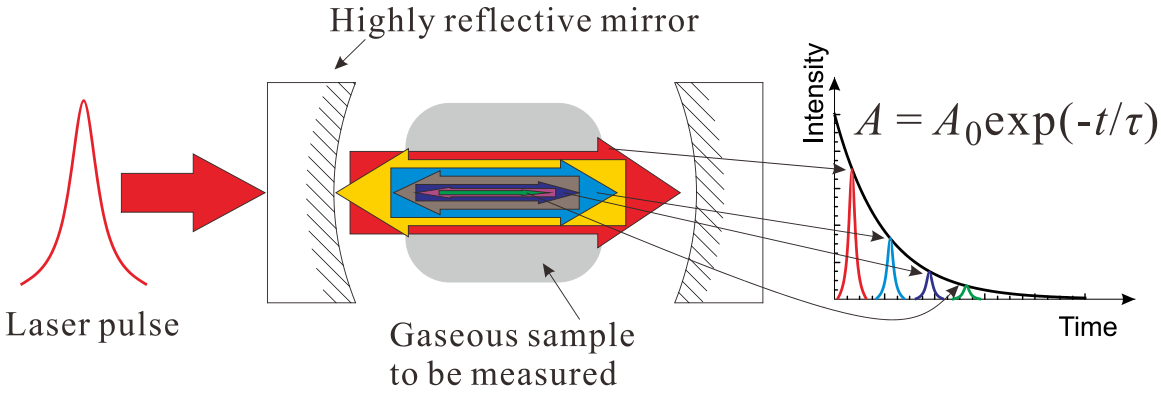

Figure 2-13. Schematic illustration of CRD setup.

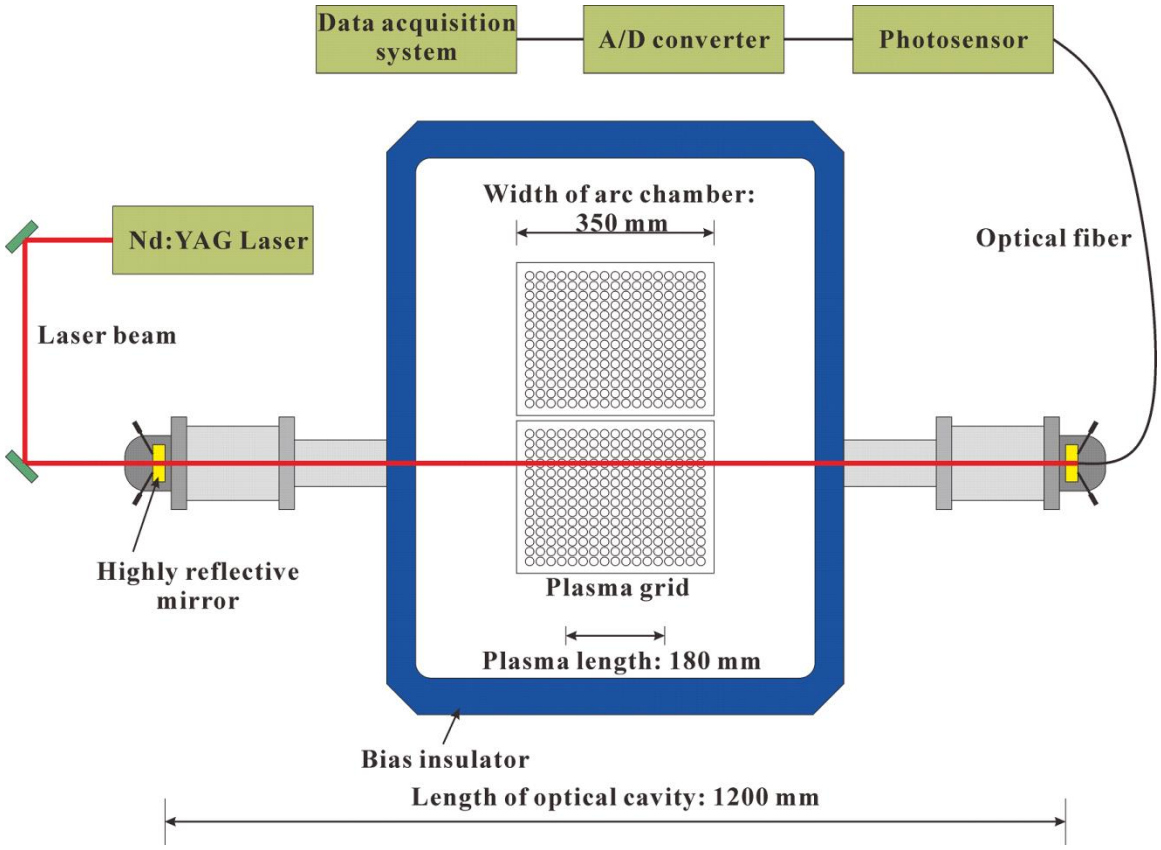

Figure 2-14. Schematic illustration of CRD setup on the RNIS [10].

In a typical CRD setup for line-averaged density, which is the averaged density along the laser column, an optical cavity which consists of a pair of highly reflective mirror is utilized and the object to be measured is located in the cavity. A laser beam with a short

duration is irradiated into the cavity and reflected back and forth thousands of times in the optical cavity. The intensity of the laser beam leaking through the cavity mirror decreases exponentially. The decay time is converted to the line-averaged density of the object in the optical cavity. The schematic illustration of the concept of CRD is shown in Figure 2-13.

By plotting the time evolution of the leaking laser intensity from the optical cavity, an exponentially decaying envelope curve can be obtained. Fitting this envelope with an exponentially decaying function $A = A_0\exp(-t/\tau)$, where A is the intensity of the envelope, A_0 is the maximum value of the envelope and t is time, the decay time also named ring-down time τ is determined. The line-averaged density can be estimated from the ring-down times without and with the gaseous sample in the optical cavity.

Figure 2-14 is the cross-sectional view of the ion source from the back plate side with the installation of a CRD system. The highly reflective mirrors with reflectivity 0.99994 are installed on the mirror mounts, which are installed on the bias insulator. In the experiments, the length of the optical cavity is 1200 mm. A laser pulse with wavelength of 1064 nm, time duration of 5 ns, repeat rate of 20 Hz and diameter of 7 mm, emitted from a Nd:YAG laser, is irradiated into the optical cavity. The pulse energy is lower than 50 mJ. The leaking light transmits through a collimator lens and a fiber to a photosensor which converts the light signal to analog electrical signal. The analog signal is then converted to digital signal by an A/D converter and acquired by a data acquisition system.

Since the line-averaged density of the gaseous sample can be determined the ring-down times of the leaking light without and with the sample, we can define the ring-down time without sample as τ_0. When H^- ions exist, an H^- ion in the laser column can be detached. That is because the photon energy of the Nd:YAG laser is 1.17 eV and it is enough to detach the electron of H^- ion in the affinity level of 0.754 eV below vacuum level. This photo neutralization process is indicated with the equation below

$$H^- + h\nu = H + e. \tag{2-4}$$

The laser intensity decreases in this process. In other words, the laser is absorbed by H^- ions. One can expect the detected intensity of the leaking light decreases, so does the

ring-down time. If the ring-down time with H^- ions is determined as τ, the line-averaged density of H^- ions is then calculated according to Ref. [10]:

$$n_{(CRD)} = \frac{1}{c} \cdot \frac{1}{\sigma} \cdot \frac{d}{L} \cdot \left(\frac{1}{\tau} - \frac{1}{\tau_0} \right). \quad (2\text{-}5)$$

where $n_{(CRD)}$ is the density of H^- ions, c is the speed of light in vacuum, σ is the cross section for the reaction in Equation 2-4, L is the plasma length in the ion source and d is the length of the optical cavity. For the detachment of H^- ions by laser of 1064 nm wavelength, σ is 3.5×10^{-21} m^2 [11]. On the RNIS, L is 0.18 m which is the full width at half maximum (FWHM) of the electron density profile measured by a single Langmuir probe. d is 1.2 m as shown in Figure 2-14. A typical ring-down signal is shown in Figure 2-15. For τ_0 = 114.81 μs and τ = 21.07 μs, the line-averaged H^- ion density is calculated to be 2.46×10^{17} $/m^3$.

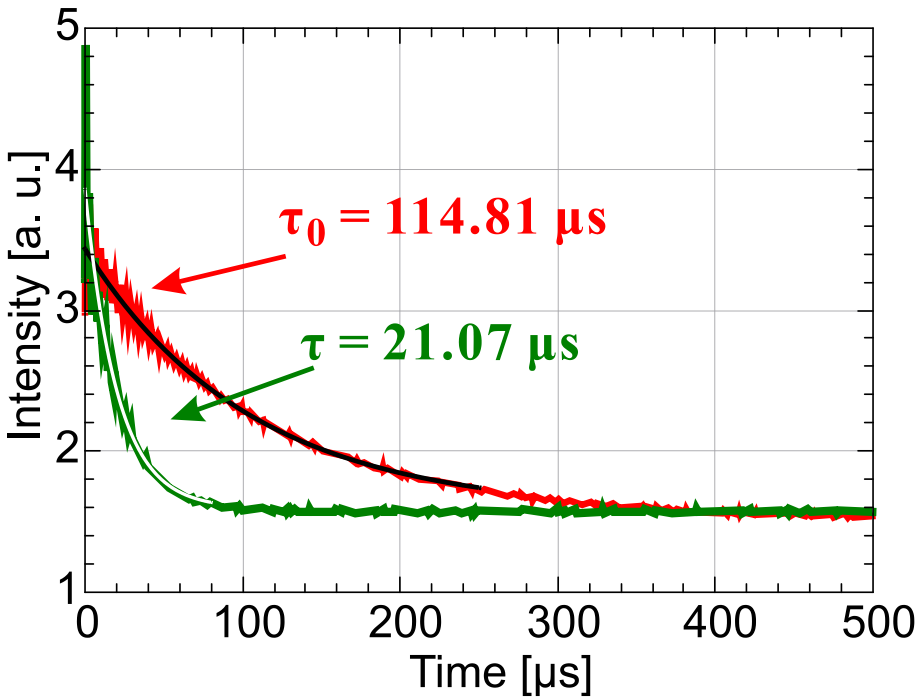

Figure 2-15. Ring-down signals with and without H^- ions. τ_0: decay time without H^- ions and τ: decay time with H^- ions [10].

2.5 Laser photodetachment

2.5.1 Configuration of laser photodetachment

Although the line-averaged H^- density can be obtained by the CRDS technique, the regular CRD method is not enough to obtain the H^- density at a specific point. It can be found that in Equation 2-4, an H^- ion is detached and an H atom and an electron are produced immediately without increase in positive ion density, because the detached electron density is equal to the original H^- ion density. If a positively biased probe tip is located inside the laser column, detached electrons flow to the biased probe tip and introduce an instantaneous increase in the probe current. This current increase (I_{pd}) is proportional to the density of the detached electrons, in other words, proportional to the original H^- density, and is applied to determine the H^- density at a specific point [11,12].

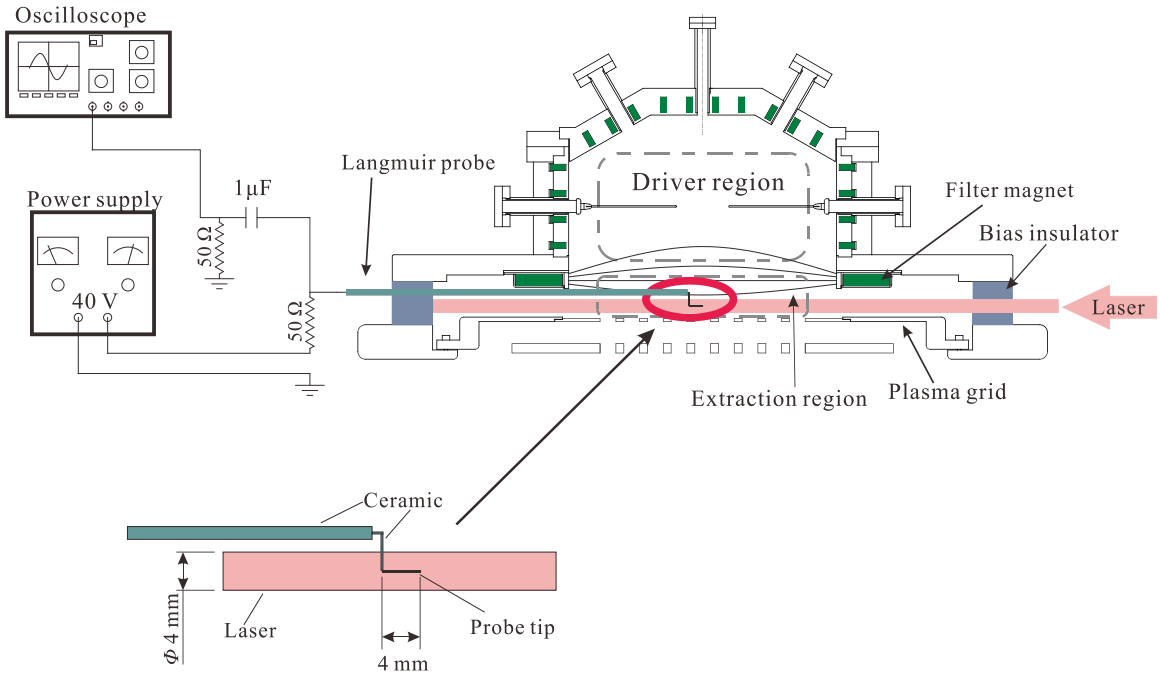

Figure 2-16. Configuration of laser photodetachment on the RNIS.

Figure 2-16 shows the laser photodetachment setup on the RNIS. A single Langmuir probe is installed into the extraction region through a port at the bias insulator. A laser pulse is irradiated into the ion source co-axially with the probe tip through a quartz

window. This probe tip with a length of 4 mm and diameter of 0.5 mm is bent to an L-shape and whole the part except for the tip is covered with ceramic. Therefore, the interaction of the laser beam and the probe stem can be avoided to reduce the influence of scattered laser light. A DC voltage is applied to the single Langmuir probe and an electron current I_e is drained. During the laser pulse, whose duration is 5 ns, H^- ions in the laser column release electrons of their affinity level and electron density in the laser column increase immediately. Consequently, the current transmitted though the probe has an instantaneous increase. The current increase I_{pd} transmits through a capacitor and recorded by a storage oscilloscope or a high-speed ADC with sampling rate of 1 GS/s.

A typical waveform of the photodetachment current is shown in Figure 2-17. The first spike of the waveform is because the radius of the probe sheath is the same as that before photodetachment and the distribution function of the detached electrons is not changed during the spike [11,13]. After the spike, the radius of the probe sheath shrinks and becomes stable. Then a plateau appears in the waveform. The photodetachment current is defined as the plateau part of the waveform as indicated in Figure 2-17.

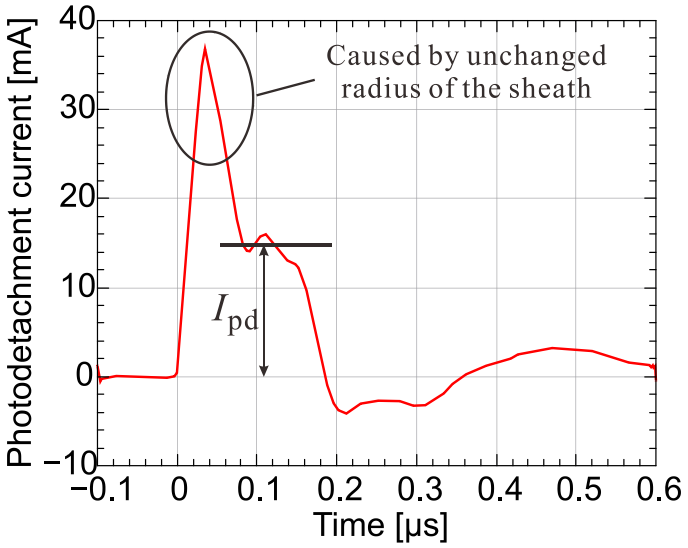

Figure 2-17. Waveform of the photodetachment current. Note that time 0 indicates the moment when laser pulse is irradiated.

In order to evaluate the H^- density from photodetachment current, it is necessary to detach all the H^- ions in the laser column and drain all the detached electrons in the collection region of the probe. These requirements represent the settings of laser wavelength, energy density, beam diameter and the probe voltage.

2.5.2 Wavelength of the laser

The energy of laser photons should be high enough to detach the H^- ions, and should be low in order to avoid ionization of other particles ablation of adsorbed atoms on the probe tip. An Nd:YAG laser is suitable for the detachment of H^- ions since the photon energy 1.17 eV is enough to detach the H^- ions with electron affinity of 0.754 eV, and too low to ionize other particles in the hydrogen plasma [11]. The cross section of photodetachment is $3.5\times10^{21}/m^2$. The choice of laser wavelength is the same as the CRD technique.

2.5.3 Energy density of the laser pulse

The laser beam is required have enough photons to detach all of the H^- ions in the laser column. In other words, the laser beam should have sufficient energy. The fraction of detached H^- ions $\Delta n_{H^-}/n_{H^-}$ increases with respect to increasing energy density of the laser pulse and is expressed as [11,12]:

$$\frac{\Delta n_{H^-}}{n_{H^-}} = 1 - \exp\left(-\frac{\sigma}{h\nu} \cdot \frac{E_{laser}}{S_{laser}} \right), \tag{2-5}$$

where σ is the cross section of photodetachment for H^- ions, E_{laser} is the energy of the laser pulse and S_{laser} is the cross sectional area of the laser beam. At high energy density of the laser pulse, the fraction of detached H^- ions $\Delta n_{H^-}/n_{H^-}$ saturates.

Figure 2-18 shows the measured fraction $\Delta n_{H^-}/n_{H^-}$ with increasing energy density of the laser pulse at hydrogen pressure of 0.3 Pa and 0.6 Pa. The fraction of detached H^- ions saturates when the power density of the laser pulse is higher than 40 mJ/cm^2. Then, at higher laser power density than ~90 mJ/cm^2, the slope of the photodetachment current gradually starts to increase. This is caused by the interaction of the laser pulse and the

probe tip. The probe tip is heated up by laser irradiation with high energy density, which ablates the probe tip surface [14,15]. In the experiments, the power density of the laser pulse was set to 40 mJ/cm^2 to avoid over-estimation of the H^- density.

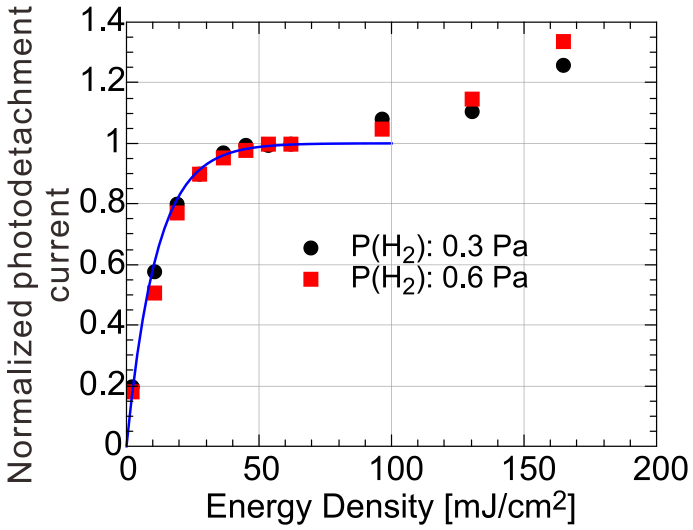

Figure 2-18. Fraction of detached H^- ions vs. energy density of laser pulse at hydrogen pressure of 0.3(black solid circle) and 0.6 Pa (red solid square).

2.5.4 Voltage of the probe

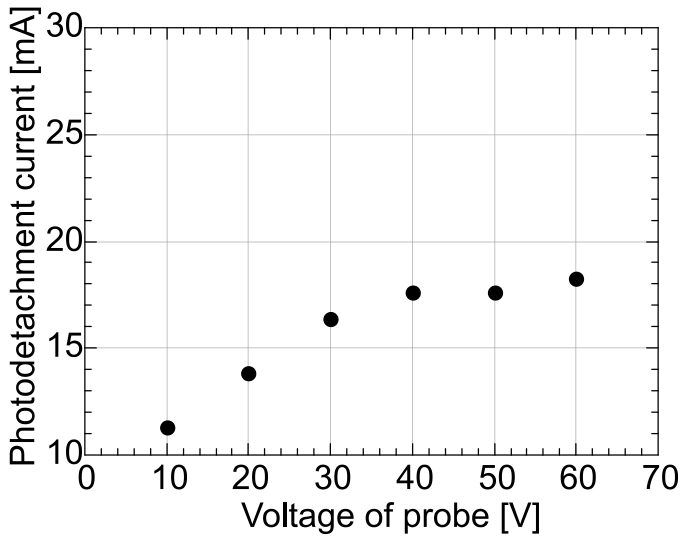

Figure 2-19. Photodetachment current as a function of probe voltage with respect to the arc chamber.

The probe tip should be applied voltage high enough to drain all the detached electrons. Figure 2-19 shows the dependence of phtodetachment current on the voltage of probe with respect to the arc chamber. It can be found that the photodetachment current saturates when the probe voltage is higher than 40 V. Therefore, in the experiments, the voltage applied to the probe for photodetachment was set to 40 V.

2.5.5 Diameter of the laser beam

In order to obtain the H^- ion density at specific points, the radius of the laser beam should be larger than the collection distance of the probe. The dependence of the photodetachment current on the diameter of the laser beam is shown in Figure 2-20. The photodetachment current saturates at 2 mm of laser beam diameter. This result is consistent with Bacal's experiment [11]. Laser with 4 mm of beam diameter was chosen for the photodetachment experiments.

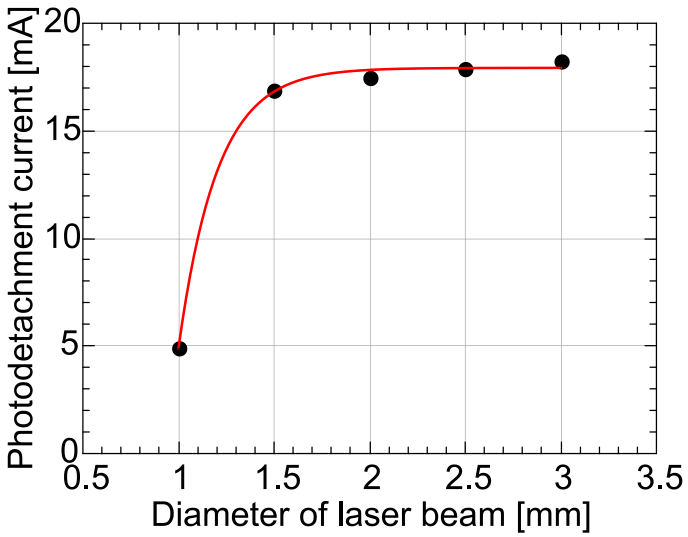

Figure 2-20. Dependence of photodetachment on the diameter of laser beam.

2.5.6 H^- density

Traditionally, the H^- density is calculated from the photodetachment current according to the probe current before laser irradiation $I_{e(DC)}$ and electron density n_e. $I_{e(DC)}$ is proportional to the background electron density n_e. The laser irradiation causes an instantaneous increase of electron density Δn_e and $\Delta n_e = n_{H^-}$ is proportional to the photodetachment current. If the energy density of the laser pulse is sufficient to detach all the H^- ions in the laser column, the H^- ion density can be calculated according to [11,12]

$$\frac{n_{H-}}{n_e} = \frac{I_{pd}}{I_{e(DC)}}, \tag{2-6}$$

where I_{pd} donates to the photodetachment current. n_{H^-} is hence expressed as:

$$n_{H-} = \frac{I_{pd}}{I_{e(DC)}} \cdot n_e . \tag{2-7}$$

The electron density n_e is determined by the single Langmuir probe working in sweeping voltage mode in advance.

The method in Equation 2-7 is available for the plasma in which n_{H^-} is low since the probe current is contributed by electrons and the contribution of H^- ions to the probe current can be ignored. However, in a Cs-seeded ion source, n_{H^-} is high and negative-ion-rich plasma of which n_e is one order lower than n_{H^-} can be found in the extraction region. The contribution of the H^- ions to the probe current cannot be ignored. The probe current is expressed as:

$$I_{probe} = I_e + I_{H-}, \tag{2-8}$$

where I_e and I_{H^-} are the contribution of electrons and H^- ions to the probe current, respectively. During photodetachment process, I_{probe} increases to

$$I'_{probe} = I_e + I_{pd\_e}, \tag{2-9}$$

where I_{pd_e} is the component of the probe current caused by the detached electrons. Then the photodetachment current is

$$I_{\mathrm{pd}} = I'_{\mathrm{probe}} - I_{\mathrm{probe}} = I_{pd\_e} - I_{\mathrm{H-}}. \tag{2-10}$$

Since the probe current has a component caused by H^- ions according to Equation 2-8, the method to calculate H^- ion density by Equation 2-7 is not available. Equation 2-10 indicates that I_{pd} is still proportional to the H^- ion density. A method to determine the coefficient for the calculation of $n_{\mathrm{H-}}$ from I_{pd} is required. This coefficient has been obtained by calibrating the photodetachment current with line-averaged H^- density by means of CRD method.

The CRD mehtod allows the measurement of line-averaged H^- ion density or line-integrated H^- ion density. In photodetachment, a profile of photodetachment current is obtained by scanning the probe along the laser beam. The comparison of the integral of this profile and the line-integrated H^- ion density from the CRD gives the coefficient to evaluate the H^- density at specific point from photodetachment current.

Figure 2-21 shows the profile of photodetachment current in pure hydrogen plasma at 1.2 Pa of hydrogen pressure, 5.7 V of bias voltage of the plasma grid and 50 $\pm$2.5 kW of input arc power. The comparison of the integral of this profile and line-integrated H^- density is

$$k_{\mathrm{pd}} \cdot \int I_{\mathrm{pd}} \cdot dx = n_{\mathrm{H-(CRD)}} \cdot L, \tag{2-11}$$

where $n_{\mathrm{H-(CRD)}}$ is the line-averaged H^- density from CRD and L = 0.18 m is the plasma length indicated in Section 2.4 and k is the required coefficient for the calculation of H^- density. $n_{\mathrm{H-(CRD)}}$ is $1.16\times10^{17}/\mathrm{m}^3$ with the ion source working parameters indicated in Figure 2-21. k_{pd} is then calculated to be $0.105\times10^{17}\cdot\mathrm{m}^{-3}\cdot\mathrm{mA}^{-1}$. Figure 2-22 shows the comparison of H^- density by photodetachment and CRD. It can be found that k_{pd} is independent on the H^- density and does not change even in the case of Cs-seeded plasma.

The H^- density is thus:

$$n_{\mathrm{H-}} = k_{\mathrm{pd}} \cdot I_{\mathrm{pd}}. \tag{2-12}$$

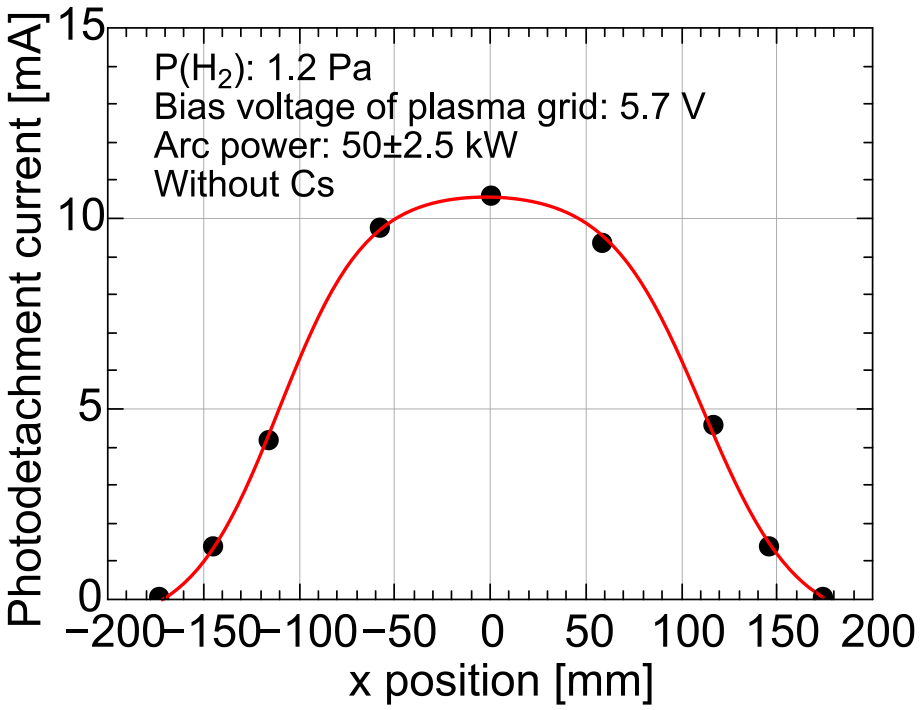

Figure 2-21. Profile of phtotdetachment current in pure hydrogen plasma.

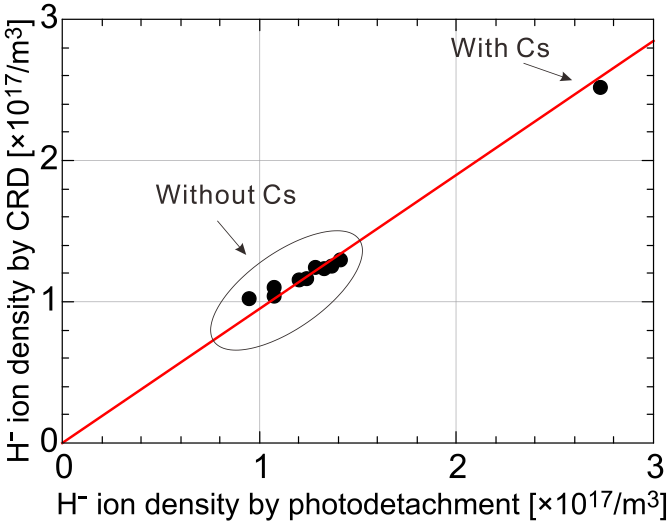

Figure 2-22. Comparison of H^- density by photodetachment and CRD.

2.6 Summary

The RNIS is an arc-driven negative hydrogen ion source equipped with 12 hair-pin-type filaments and the plasma is confined with multicusp magnetic field. An external filter field is applied to separate the driver region and the extraction region. The electron temperature decreases in the diffusion process from the driver region to the extraction region. A bias voltage is applied to the plasma grid to suppress near the plasma grid. A magnetic field generated by electron deflection magnets, named EDM field is utilized to deflect the extracted electron beam. Experiments using Langmuir probe, CRD and photodetachment were carried out on the RNIS for the diagnostics of the plasma in the extraction region. Basic plasma parameters such as plasma potential, electron density and electron temperature has been obtained with Langmuir probe. The CRD provided line-averaged H^- density. The photodetachment technique was adopted to measure the H^- density at a specific point. In the negative-ion-rich plasma, conventional method based on the probe current and electron density to evaluate H^- density from the photodetachment current is not available. Therefore, a new calibration method with use of CRD and the photodetachment technique has been developed. As, a result, the coefficient $k_{pd} = 0.105 \times 10^{17} \cdot m^{-3} \cdot mA^{-1}$ has been estimated by the comparison of line-integrated H^- density and the integral of the profile of the photodetachment current along the laser beam. Using this new method, the H^- density at a specific point can be determined not only in the plasma with low density H^- ions but also in negative-ion-rich plasma, even in ion-ion plasma in which essentially no electrons exist. For photodetachment of H^- ions, laser pulse with wavelength of 1064 nm is applied. In order to gather all the detached electrons to the probe tip, the DC voltage applied to the probe should be higher than 40 V. The laser spot for photodetachment should have larger than 2 mm of the diameter, which corresponds to the collection length of the probe tip. The energy density of laser pulse should be 40 – 90 mJ/cm^2 to detached all the H^- ions in the laser column and avoid over-estimation of the H^- density.

References

[1] K. Tsumori, Y. Takeiri, O. Kaneko, M. Osakabe, A. Ando, K. Ikeda, K. Nagaoka, H. Nakano, E. Asano, M. Shibuya, M. Sato, T. Kondo, and M. Komada, Fusion Sci. Technol. **58,** 489 (2010).

[2] H. Nakano, K. Tsumori, K. Nagaoka, M. Shibuya, U. Fantz, M. Kisaki, K. Ikeda, M. Osakabe, O. Kaneko, E. Asano, T. Kondo, M. Sato, S. Komada, H. Sekiguchi, and Y. Takeiri, AIP Conf. Proc. **1390,** 359 (2011).

[3] K. W. Ehlers and K. N. Leung, Rev. Sci. Instrum. **50,** 1353 (1979).

[4] K. W. Ehlers and K. N. Leung, Appl. Phys. Lett. **38,** 287 (1981).

[5] J. P. Boeuf, B. Chaudhury, and L. Garrigues, Phys. Plasmas **19,** 113509 (2012).

[6] J. M. Wadehra, Phys. Rev. A **29,** 106 (1984).

[7] R. K. Janev, W. D. Langer, K. J. Evans, and D. E. J. Post, *Elementary Processes in Hydrogen-Helium Plasmas: Cross Sections and Reaction Rate Coefficients* (Springer Science & Business Media, 2012).

[8] I. G. Brown, *The Physics and Technology of Ion Sources* (John Wiley & Sons, 2004).

[9] H. Amemiya, J. Plasma Fusion Res. **69,** 934 (1993).

[10] H. Nakano, K. Tsumori, M. Shibuya, S. Geng, M. Kisaki, K. Ikeda, K. Nagaoka, M. Osakabe, Y. Takeiri, and O. Kaneko, Journal of Instrumentation **11,** C03018 (2016).

[11] M. Bacal, Rev. Sci. Instrum. **71,** 3981 (2000).

[12] M. Bacal, G. W. Hamilton, A. M. Bruneteau, H. J. Doucet, and J. Taillet, Rev. Sci. Instrum. **50,** 719 (1979).

[13] F. E. Balghiti‐Sube, F. G. Baksht, and M. Bacal, Rev. Sci. Instrum. **67,** 2221 (1996).

[14] Z. Kiss'ovski, S. Kolev, S. Müller, T. Paunska, A. Shivarova, and T. Tsankov, Plasma Phys. Control. Fusion **51,** 015007 (2009).

[15] S. Kajita, S. Kado, and S. Tanaka, Plasma Sources Sci. Technol. **14,** 566 (2005).

3. Characteristics of the plasma in the extraction region

In the extraction region, the plasma consists of positive ions, electron, and H^- ions additionally. Properties of this plasma change with the ratio of H^- ion density and electron density. This ratio is dominated by the external conditions including Cs-seeding, bias voltage of the plasma grid and hydrogen pressure. In addition, the complicated magnetic field such as electron deflection magnetic field, filter field can affect the profile of the plasma. Basic characteristics of the plasma in the extraction region are shown in this chapter.

3.1 Normal and negative-ion-rich plasma

Conventionally, plasma refers to a gas which consists of neutral particles, electrons, and positive ions. In the extraction region of a negative hydrogen ion source, plasma is different from the normal plasma due to the existence of H^- ions. The normal plasma is changed to negative-ion-rich plasma as the H^- ion density increases. A simple approach to identify the normal and negative-ion-rich plasma is the *I-V* curve of a single Langmuir probe.

In normal hydrogen plasma, the electron saturation current of a single Langmuir probe is more than 20 times higher than the positive ion saturation current. This is caused by the huge mass difference between electron and positive hydrogen ion. If H^- ions exist in the plasma, electron density decrease since $n_+ = n_e + n_{H^-}$, where n_+ is the density of positive ions. Consequently, electron saturation current of probe decreases. In extreme case, if n_{H^-} increases to almost equal to positive ion density, $n_{H^-} \approx n_+$, and the temperatures of H^- and positive ions are in the same order, probe negative saturation current is almost equal to the positive ion saturation current [1]. The term “negative

saturation current" refers to the probe current carried by negatively charged particles. The *I-V* curve becomes quasi symmetric [1,2]. The plasma contains positive and negative ions, essentially no electrons, is named "ion-ion plasma". Figure 3-1 shows the comparison of *I-V* curves of normal and ion-ion plasmas.

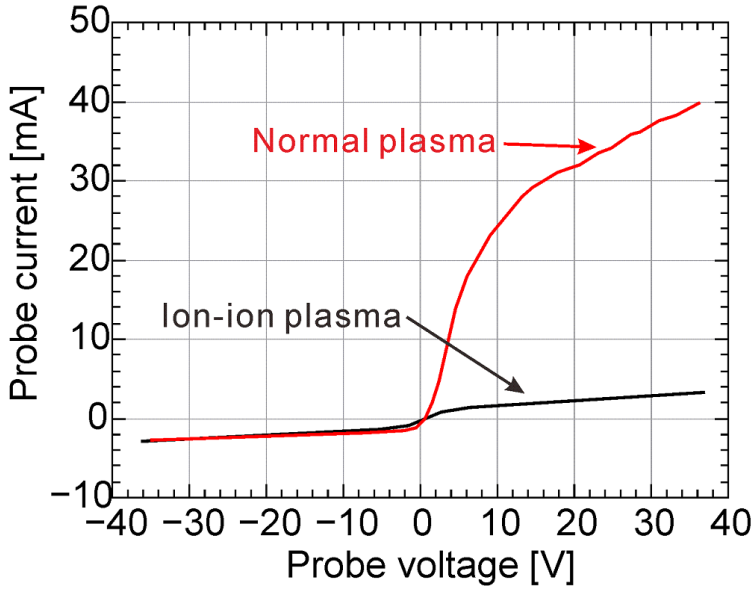

Figure 3-1. I-V curves of normal and ion-ion plasmas.

In practical operation of the RNIS, some electrons exist in the extraction region. Typically, the density of electrons n_e is one order lower than n_{H^-}. This plasma is named "negative-ion-rich plasma". This plasma is produced when Cs is seeded into the negative ion source and long time conditioning process is required in order to obtain well Cs-coated plasma grid surface.

3.2 Cs effect

The Cs line, whose tip is covered with a diffuser nozzle, is installed on the back plate of the negative ion source as illustrated in Figure 2-1. A complicated Cs transport process occurs after starting to seed Cs into the ion source. During experiments, the valve of Cs line is kept on, and Cs vapor flows to the ion source continuously. Research about Cs transport by Yoshida et al. [3] indicated that in the beginning phase of the Cs

injection, thick Cs layer are mainly covered on the wall of the plasma chamber closed to the Cs nozzle. After the covered Cs is saturated near the nozzle, the Cs layer starts to evaporate and expand to the area far from the back plate due to heating by incident particle and filament and/or plasma radiation. Evaporated Cs atoms ionize in the arc plasma and evaporation continues for a while after arc discharge due to remaining heat of the inner wall of the chamber. The Cs covered on the plasma grid surface mainly comes from the evaporated Cs atoms from the wall of the plasma chamber. In order to obtain appropriate Cs coating on the plasma grid, long time conditioning is necessary in the case of the RNIS.

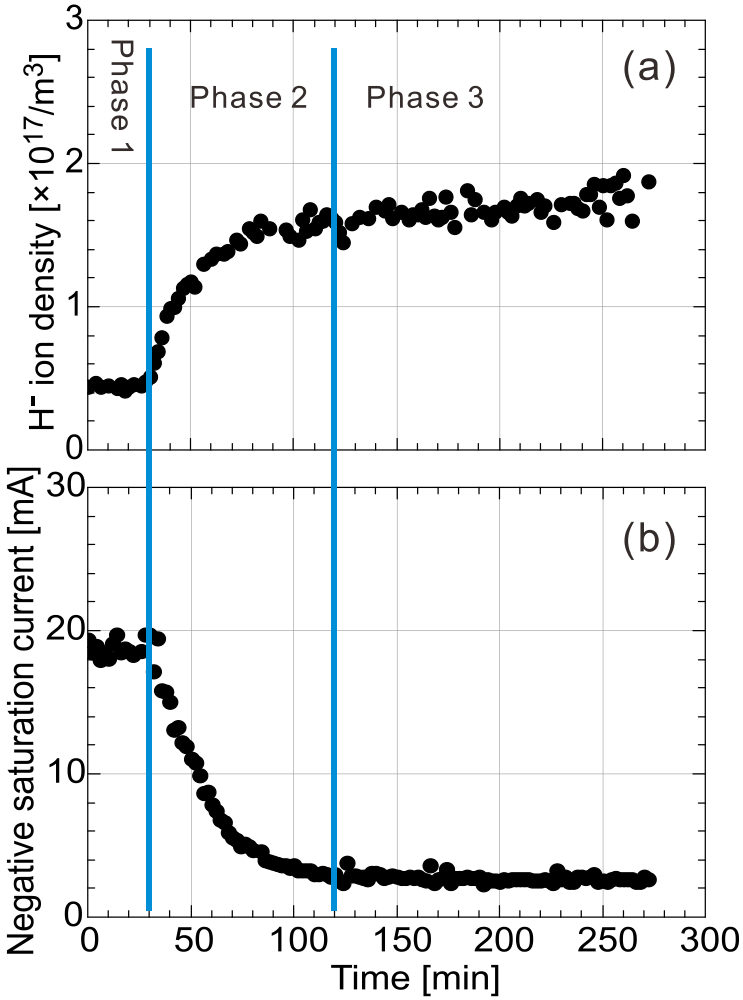

Figure 3-2. Time evolution of plasma parameters during Cs conditioning. (a) H^- density measured by CRD and (b) negative saturation current of Langmuir probe. Note that time 0 indicates the moment when Cs injection starts.

Figure 3-2 shows the time evolution of plasma in the extraction region during Cs-conditioning on the RNIS. The conditioning process is divided into three phases: phase 1 (time < ~30 min), phase 2 (~30 min < time < ~120 min) and phase 3 (time > 120 min). In phase 1, the H^- ion density keeps stable as shown in Figure 3-2 (a). It suggests that the Cs coverage on the plasma-grid surface is insufficient to enhance the production of H^- ions. Correspondingly, the probe negative saturation current shown in Figure 3-2 (b) keeps stable too in phase 1.

In phase 2, H^- ion density starts to increase. It indicates that the Cs coverage on the plasma-grid surface is sufficient to decrease the work function of the plasma-grid surface and H^- ion production is enhanced. Meanwhile, the Langmuir probe measurement shows that probe negative saturation current decreases. In the extraction region of the negative ion source, the charge neutrality is conserved by positive ions, electrons and negative ions. During phase 2, more and more electrons are replaced by H^- ions. Therefore, the increment in H^- ion density causes decrease in electron density and probe negative saturation current. The decrement in probe negative saturation current corresponds to the difference of extraction current and acceleration current I_{ext} - I_{acc}, which is roughly extracted electron current.

In phase 3, the H^- ion density and probe negative saturation current become flat.

During Cs-conditioning the time evolution of plasma potential is shown in Figure 3-3. The tendency of plasma potential during Cs-conditioning corresponds to those of H^- ion density and probe negative saturation current. It is shown that the plasma potential decreases as increasing H^- ion density. One of the possibilities is the emission of the H^- ions from the surface of the plasma grid can modify the flux of the positive ions to the plasma grid [4]. The sheath potential is determined by the flux of negatively and positively charged particles to the plasma grid. Emission of H^- ions from the plasma grid to the plasma causes a decrease in the net flux of negatively charged particles towards to the plasma grid. Consequently, flux of positive ions decreases too and causes a reduction of charge density in the sheath. Then the electric field in the sheath decreases following the reduction of the charge density and bring a decrement of the sheath potential.

Because the plasma grid is biased at a fixed potential, the plasma potential decrease as the decrease of the sheath potential.

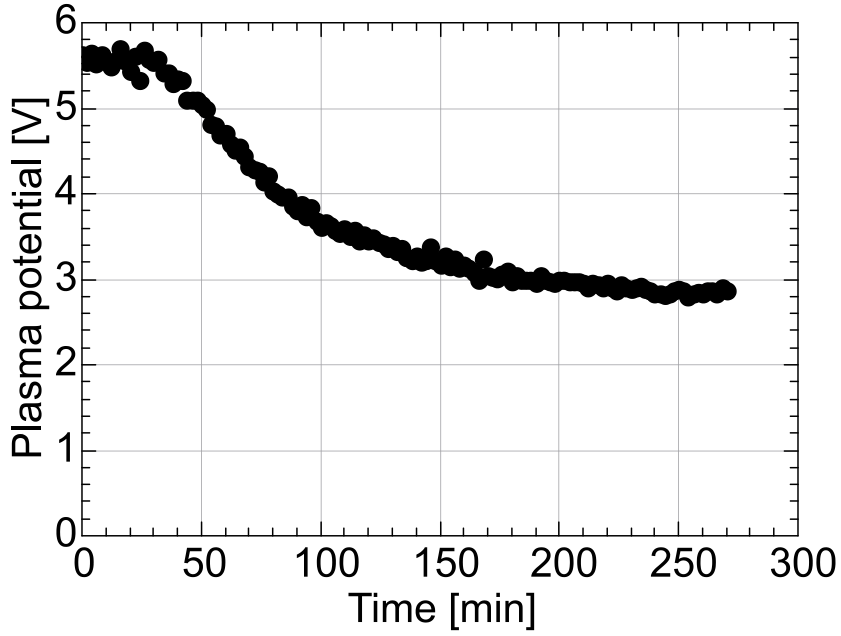

Figure 3-3. Time evolution of plasma potential during Cs-conditioning.

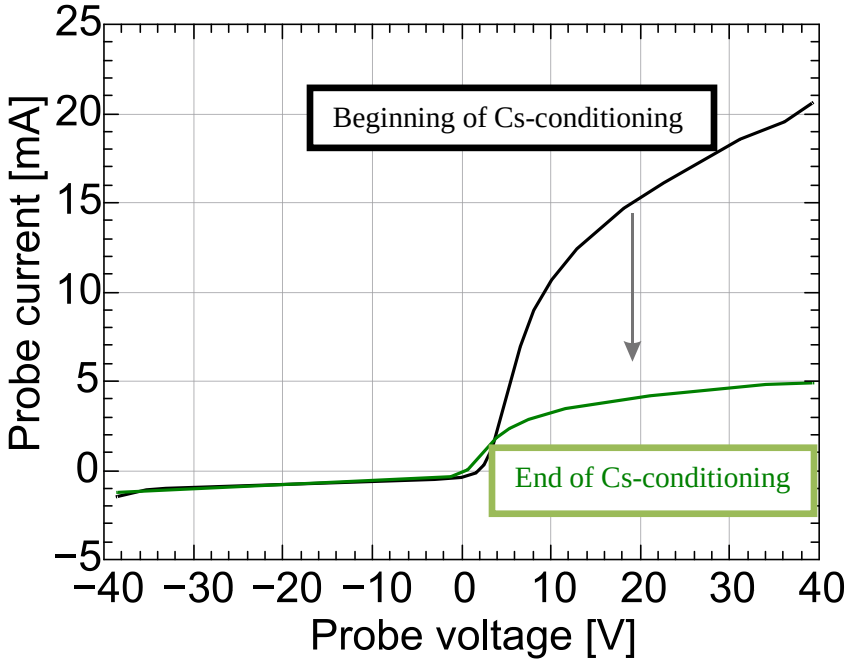

Figure 3-4. Variation of probe *I-V* curve during Cs-conditioning. These two curves are at the beginning and end of Cs-conditioning.

Figure 3-4 shows the variation of the probe *I-V* curve during Cs-conditioning. The two curves are at the beginning and end of the Cs-conditioning process. The negative saturation current decreases with the conditioning time. In this process the positive saturation current carried by positive ions keeps stable. Decrement of the negative saturation current is caused by the reduction of electron density. At the end phase of the Cs-conditioning, negative-ion-rich plasma is obtained in the extraction region.

3.3 Effect of controlling parameters

The performance of the N-NBI system is determined by the negative ion source. The fundamental requirements for the negative ion source are effective H^- ion extraction for high H^- ion beam current and suppression of the co-extracted electrons. It is required to understand the basic dependence of the plasma in the extraction region on the external controlling parameters including bias voltage of the plasma grid and gas pressure of hydrogen. Furthermore, the optimized working condition can be found.

3.3.1 Dependence on bias voltage of the plasma grid

The plasma grid is biased by a DC voltage with respect to the plasma chamber to suppress the electrons in the extraction region by absorbing the electrons or repelling the positive ions. Therefore, the bias voltage of the plasma grid V_{bias} plays an important role on the charged particle flux of the plasma in the extraction region [5].

Figure 3-5 shows the dependence of H^- ion density n_{H^-} measured by photodetachment, on the bias voltage of the plasma grid V_{bias} before and during beam extraction. It can be found that if V_{bias} is negative, n_{H^-} keeps stable before and during beam extraction. At positive V_{bias}, n_{H^-} decreases with increasing V_{bias}. The reduction of n_{H^-} deceases at positive V_{bias}. When V_{bias} is higher than 4 V, n_{H^-} during beam extraction is equal to that of before beam extraction.

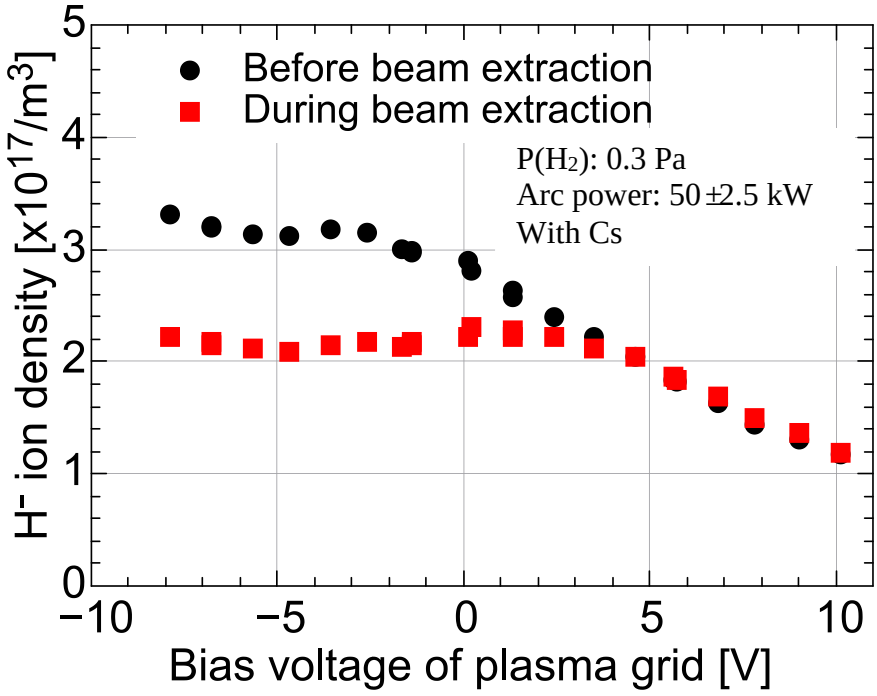

Figure 3-5. Dependence of H^- density on the bias voltage of plasma grid.

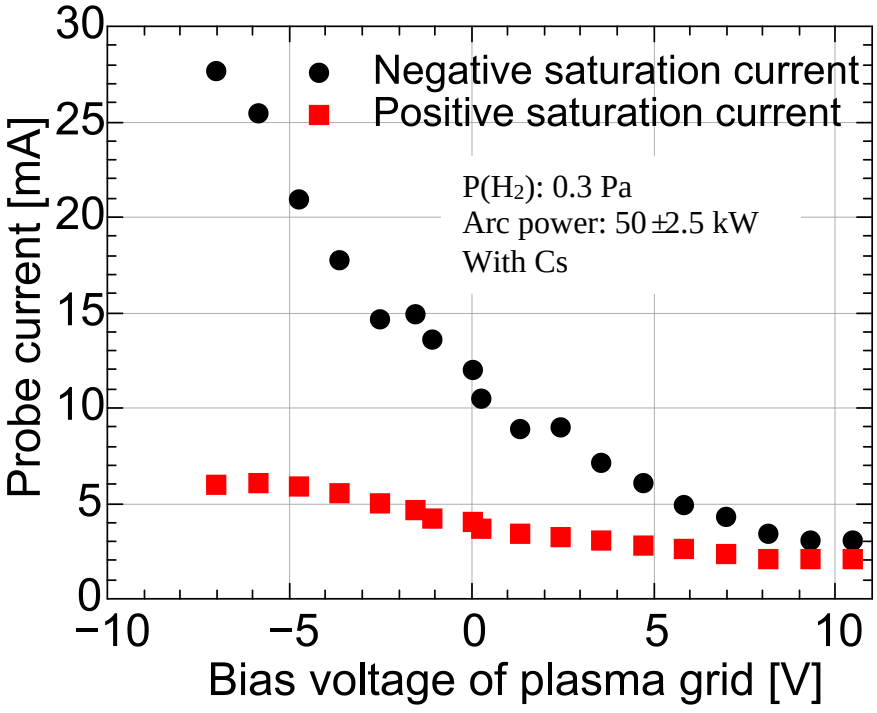

Figure 3-6. Probe saturation current changes with the bias voltage of plasma grid.

The measurement of a single Langmuir probe shows in Figure 3-6 indicate the behavior of negative and positive saturation currents when V_{bias} is changing. The decreasing negative saturation current reveals the depletion of electrons by the plasma

grid. On the other hand, positive ions are repelled by the plasma grid when the bias voltage is increasing.

Variation of the plasma including electrons, H^- ions and positive ions causes the changes of extracted and accelerated currents. Figure 3-7 is the dependence of extraction and acceleration current on the bias voltage of plasma grid. The extraction and acceleration current is measured as the drain current of the power suppiesy of the accelerator grid system (see Figure 2-2). The extraction current contains both electron and H^- ion components. Electrons in the extracted beam are deflected and absorbed by the extraction grid. Therefore, the acceleration current can represent the H^- current. The extraction current decreases with increasing V_{bias}. This phenomenon is consistent with the dependence of probe negative saturation current on the bias voltage of the plasma grid. Similar as the behavior of the H^- density during beam extraction, the acceleration current keeps almost stable at the bias voltage of lower than 4 V and decreases with higher V_{bias}.

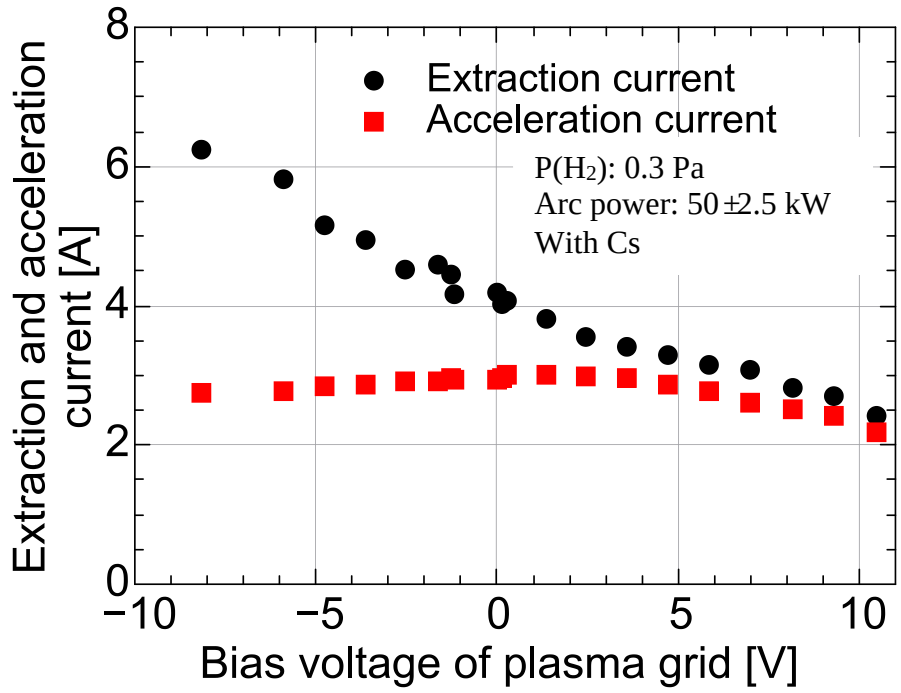

Figure 3-7. Dependence of extraction and acceleration current on the bias voltage of plasma grid.

Applying bias voltage to the plasma grid with respect to the plasma chamber is an effective method to decrease the electron density in the extraction region and to decrease

the electron component in the extracted beam. The extraction grid can be protected from the heat load and the damage can be avoided by increasing V_{bias}. However, H^- density in extraction region is also affected by V_{bias}. In order to obtain H^- beam current as high as possible and electron beam current as low as possible, it is better to apply a positive bias voltage lower than 4 V to the plasma grid.

3.3.2 Dependence on hydrogen pressure

For the negative hydrogen ion source applied for an NBI system, low operational hydrogen pressure is essential to reduce the stripping loss of H^- ions due to collisions with neutral molecules and atoms during the acceleration of H^- ions [6]. Figure 3-8 shows the dependence of n_{H^-} on the hydrogen pressure. At the pressure of 0.3 Pa n_{H^-} reaches maximum and then decreases with increasing pressure before beam extraction. At the lower pressure, n_{H^-} decreases due to the beam extraction. At the higher pressure, the beam extraction cannot lead to reduction of n_{H^-}.

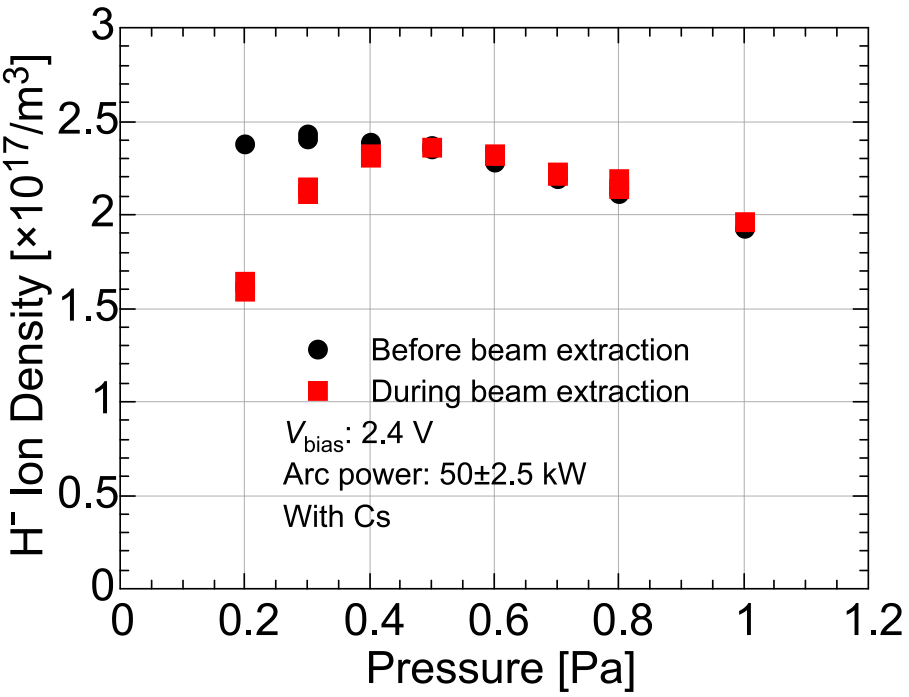

Figure 3-8. H^- density versus hydrogen pressure in Cs-seeded plasma.

By increasing the hydrogen pressure, positive ion temperature decreases because of their collision with neutral particles. Since the cross section for mutual neutralization process of H^- ions is higher at low energy of positive ions [7]. Reduction of positive ion

temperature causes enhancement of mutual neutralization [8,9]. As a consequence, n_{H^-} decreases at higher pressure.

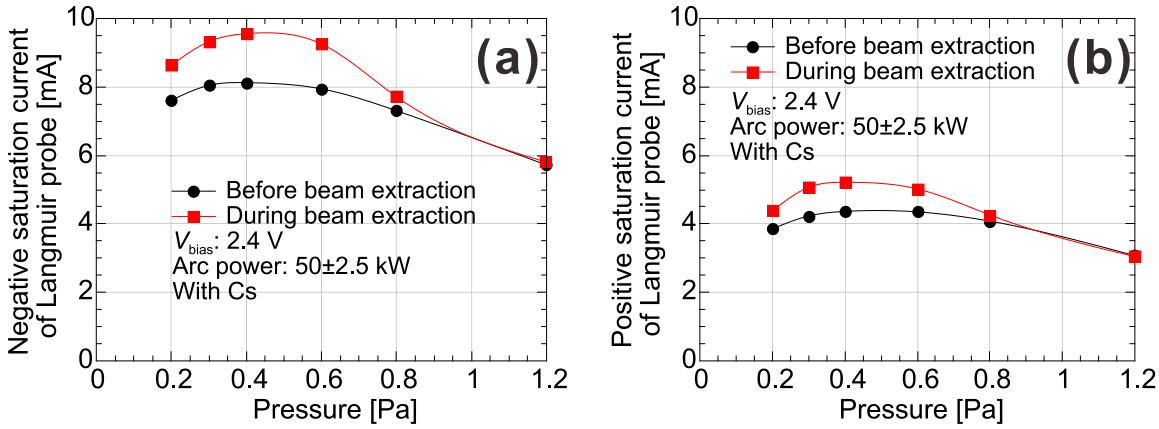

Figure 3-9. Negative (a) and positive (b) saturation currents of Langmuir probe versus hydrogen pressure in Cs-seeded plasma.

Figure 3-9 shows the variation of negative saturation current of Langmuir probe with hydrogen pressure. It can be found that the negative and positive saturation currents show the similar trend as n_{H^-}. One of the possibilities is that the mutual neutralization depletes not only H^- ions but also positive ions.

Figure 3-10 shows the dependence of extraction and acceleration currents on the hydrogen pressure. Note that at pressure higher than 0.8 Pa, the acceleration voltage was turned off due to breakdown at acceleration gap. The extraction and acceleration currents follow the behaviors of negative saturation current of the Langmuir probe and n_{H^-}. It indicates that the extraction and acceleration currents are determined by the density of negatively charged particle and H^- ions, respectively.

It is better to keep the operational pressure as low as possible to reduce the stripping loss of H^- ions. The plasma of the ion source is sustained by the electron-impact ionization, and the discharge at extremely low pressure is unstable, because the mean free paths of electrons become larger at lower pressure. Consequently, 0.2 to 0.4 Pa of hydrogen pressure is a proper choice for the operation of the negative ion source.

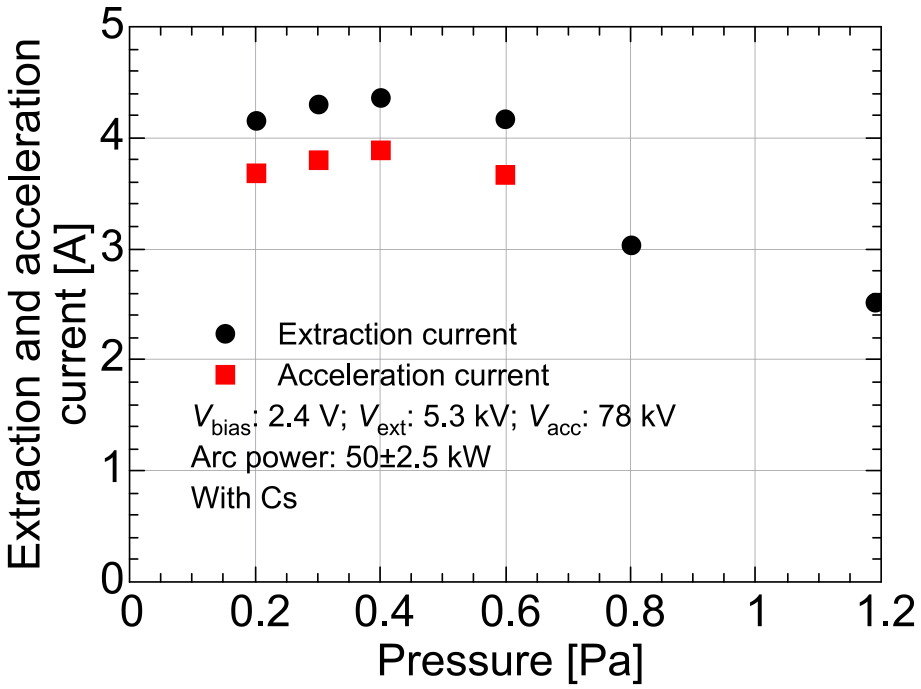

Figure 3-10. Extraction and acceleration currents versus hydrogen pressure.

3.4 Spatial profile

In the extraction region of the negative ion source, both of the filter field and electron deflection magnetic field (EDM field) exist. The magnetic field near plasma grid is complicated due to the linkage of these magnetic fields. The distribution of charged particles in the magnetic field is influenced by the field. Experiments using Langmuir and photodetachment probes have been conducted to investigate the spatial profile of the charged particles in the extraction region.

3.4.1 Profile along the filter field in extraction region

As mentioned in Chapter 2, the width of the ion source is 350 mm. The origin of *x*-axis is defined as the center of the ion source. The Langmuir probe scanned its measurement position from -175 mm to 175 mm. The scanning direction is also

indicated in Figure 3-11. As shown in Figure 3-12, the plasma is not uniform in *x*-direction. Both profiles of the negative and positive saturation currents indicate the bell type distribution of the plasma. The full width at half maximum (FWHM) of the profiles is ~180 mm, and the peak positions are near the center of the ion source. Density of charged particles decreases at the edge of the ion source. The plasma potential shows a flat profile at the central region and decreases at the edge of the ion source. In the central part of the extraction region, the electric field in *x*-direction can be ignored.

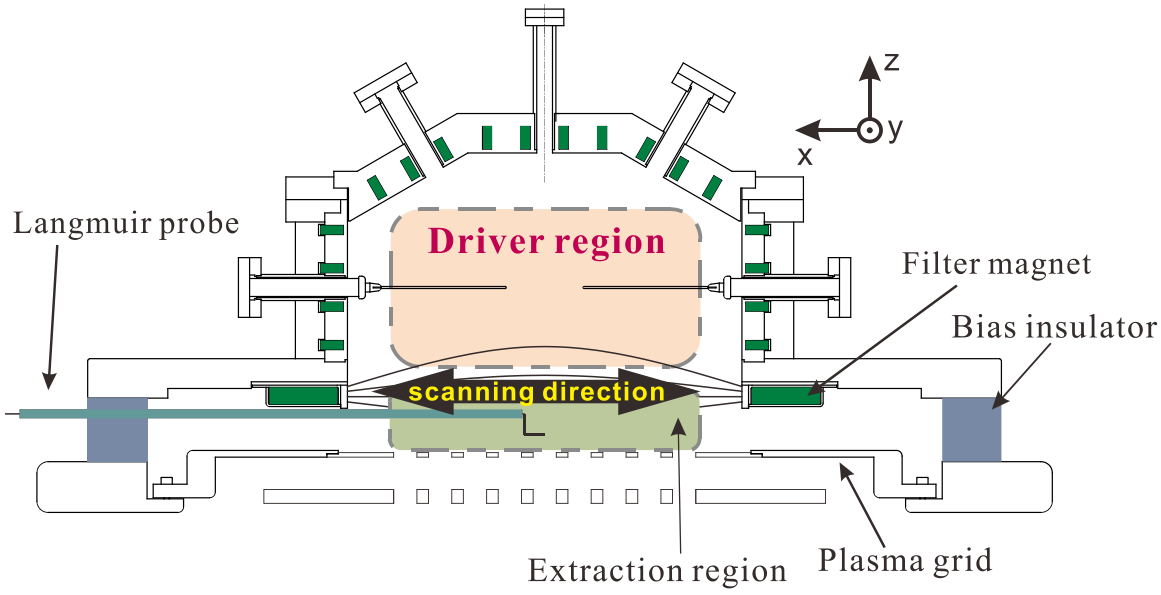

Figure 3-11. Scanning direction of Langmuir probe for the profile measurement in x direction.

The profile of n_{H^-} measured by photodetachment in *x*-direction is shown in Figure 3-13. The distribution of n_{H^-} is similar as that of negative and positive saturation currents measured using a Langmuir probe. By comparing Figure 3-12 with Figure 3-13, it can be found that H^- ions concentrate into the high plasma potential region in which electrons and positive ions also concentrate. The measured profiles are possible to relate to the distribution of filter magnetic field.

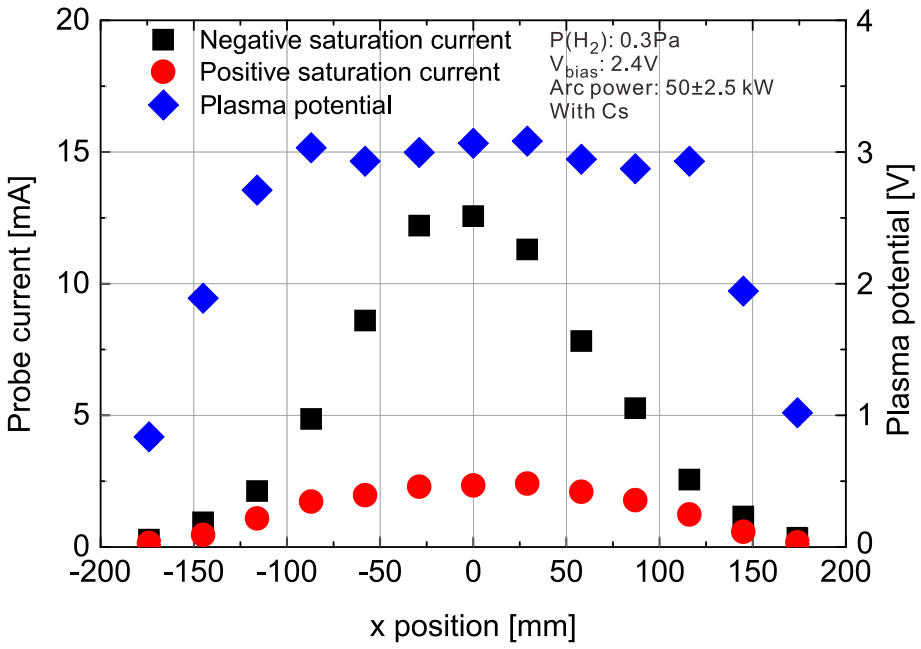

Figure 3-12. Spatial profile of charged particles and plasma potential in x direction measured by a Langmuir probe.

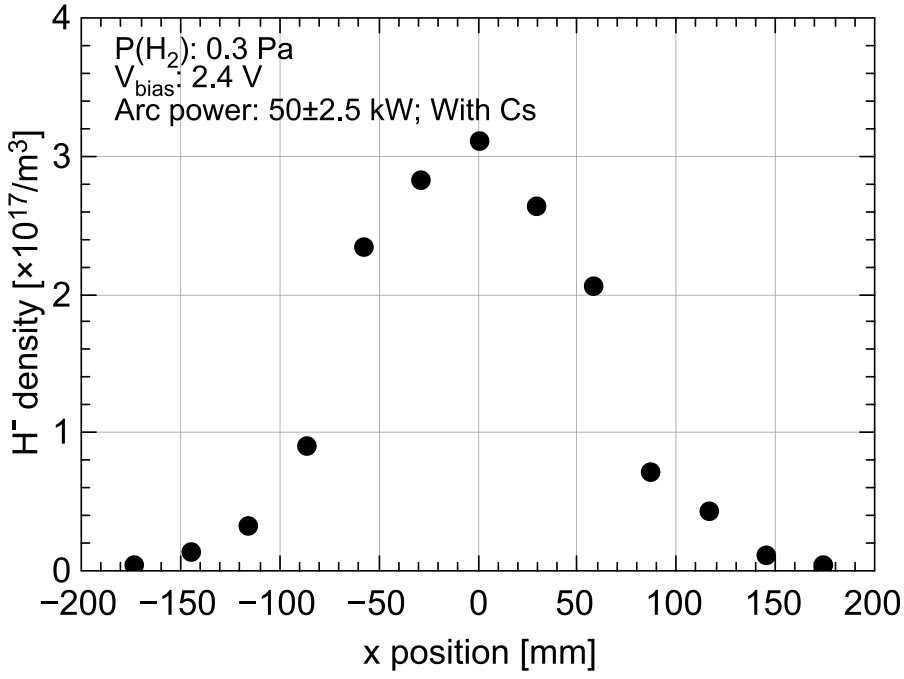

Figure 3-13. Profile of H^- density in *x*-direction measured by photodetachment.

The filter field is generated by a pair of permanent-magnet brocks installed on the plasma chamber. Close to the edge of the ion source, the strength of the filter field is high and in the central part of the beam extraction region, the strength of the filter field is low. It indicates that the filter field has a magnetic mirror structure as illustrated in Figure 2-5. The profile of the filter field in x direction is shown in Figure 3-14. Normalized profiles of plasma potential V_s, negative saturation current of Langmuir probe I_{neg}, and H^- density n_{H^-} are also plotted in Figure 3-14. It can be found that the profile of the filter field has a plateau in the central part of the extraction region and increases steeply near the both sides of the chamber wall. The region of the plateau corresponds to the flat part of the plasma potential profile. In addition, plasma density is high in the plateau region of the filter field profile. This phenomenon indicates that the plasma profile is governed by the profile of the filter field.

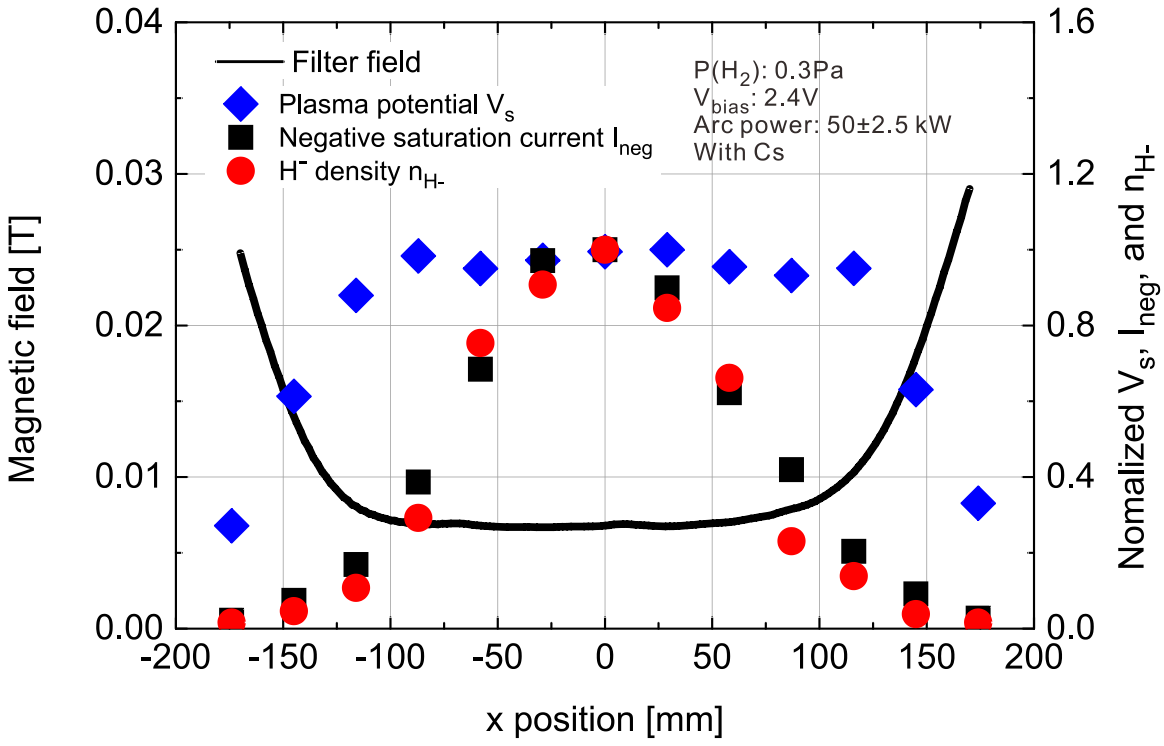

Figure 3-14. Profile of filter field in x direction. Normalized profiles of plasma potential V_s, negative saturation current of probe I_{neg}, and H^- density n_{H^-} are also plotted.

The direction of the filter field is perpendicular to the diffusion direction of electrons and positive ions. The plasma generated in driver region diffuses across the filter field to the extraction region. The diffusion process is strongly affected by the strength of the filter field, and the mobility of plasma diffusing across the filter field is proportional to $1/B^2$ for simple case [10], where B is the strength of the filer field. At the edge of the ion source, the filter field is high and prevents the diffusion of the plasma from the driver region to the extraction region. Consequently, the plasma profile in the extraction region is dominated by the distribution of filter field.

The distance between filter field and plasma grid affects to the plasma profile. When the distance is wider, profile becomes narrower because of the larger magnetic thickness of filter field. Compared with the negative ion source for LHD-NBI, the thickness of the bias insulator is 19 mm thicker in the case of NIFS-RNIS for the purpose to install the diagnostic on the insulator, and the plasma profile is expected much wider in the case of LHD ion source. Actually, five beamlet intensities are flat in the direction along the filter field of LHD source [11].

3.4.2 Profile near an extraction aperture

In Chapter 2, the electron deflection magnetic field (EDM field) has been introduced. The EDM field is generated by the permanent-magnet bars embedded into the extraction grid and to filter the electron component from the extracted beam. The polarities of the magnets are flipped alternatively row by row, and the magnets form a multiple loop fields on the both sides of the extraction grid. The loop field on the plasma grid penetrates into the extraction region across the plasma grid shown in Figure 2-7, which indicates a cross-sectional view of plasma and extraction grids with EDM loops in the *y-z* plane. The EDM field was considered to affect the plasma parameters near the plasma grid. Plasma profile near an extraction aperture has been investigated. Plasma near the plasma grid can be influenced by the EDM field. Plasma profile near an extraction aperture has been investigated.

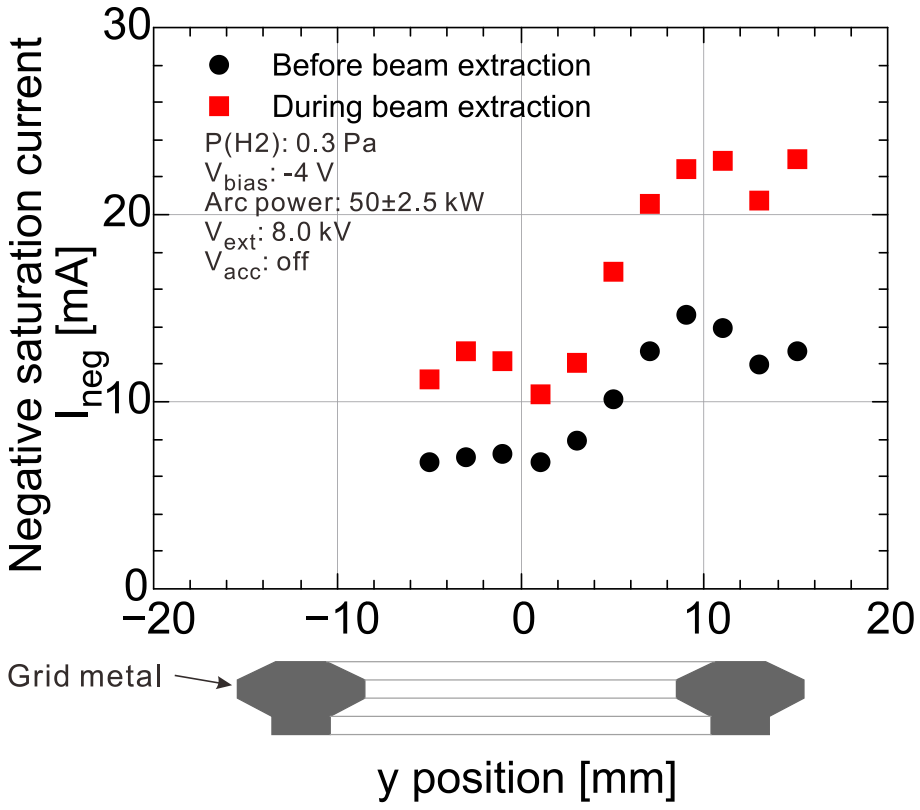

Figure 3-15. Profile of negative saturation current in y direction together with cross sectional view of plasma grid at z = 4 mm. Note that the horizontal axis indicates y position.

Figure 3-15 shows the profile of negative saturation current I_{neg} by scanning the probe-tip position in *y* direction near the plasma grid. The horizontal axis of Figure 3-15 indicates the *y* position and 0 means the central line of the extraction aperture. The probe tip was scanned parallel to the surface of the plasma grid by fixing the *z* distance at 4 mm apart from the grid. Negative saturation current I_{neg} is higher above the metal part of the plasma grid than that above the aperture. Since magnetic cusps exist on the grid metal parts as shown in Figure 2-7, higher I_{neg} suggests that electrons are trapped into the cusp field. During beam extraction, whole the profile of I_{neg} increases and it suggests more electrons flow from driver region to the extraction region. The increment of I_{neg} is obviously higher above the grid metal than that above the extraction aperture due to the magnetic cusp line, which is almost normal to the surface of plasma grid at the location and electrons comes along the field line. The profiles of I_{neg} before and during beam

extraction are not symmetric around $y = 0$. It indicates a possible plasma flow exists in y direction.

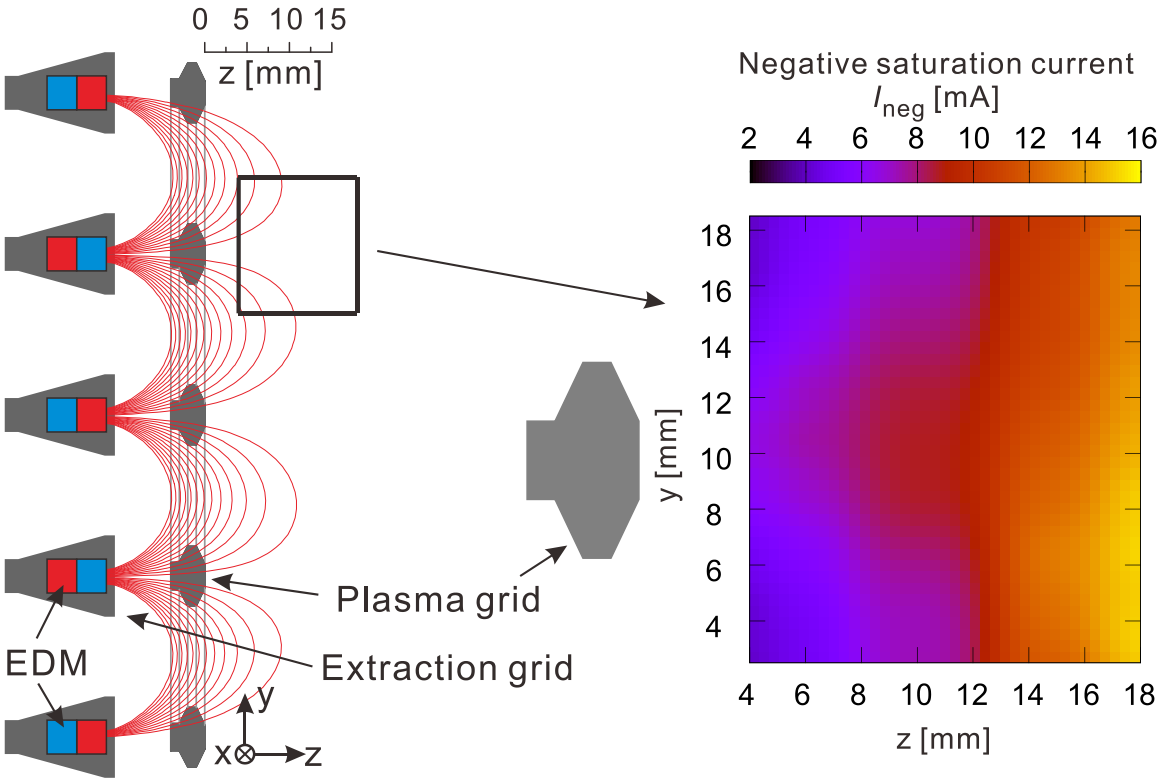

Figure 3-16. Two-dimensional profile of negative saturation current of a Langmuir probe. The EDM field is also shown. The measurement region is indicated by the square frame near the plasma grid.

Two-dimensional profile of the negative saturation current of a Langmuir probe has been obtained by scanning the probe tip near the plasma grid. The result is shown in Figure 3-16. In this figure, the EDM field is also plotted to illustrate the magnetic field in the measured region. Note that the horizontal axis is *z* position and the vertical axis is y position. $z = 0$ and $y = 0$ indicate the surface of the plasma grid and the center of the extraction aperture, respectively. The result shows that the negative saturation current is higher above the grid metal than that above the extraction aperture. It is consistent with the result shown in Figure 3-15. The result shown in Figure 3-16 suggests electrons are trapped into the magnetic cusp of the EDM field since electrons are magnetized (the

Larmor radius of electron at $z = 0$ is ~0.2 mm), and electrons flow the plasma grid. Far away from the plasma, the profile of the negative saturation current becomes flat. This flat distribution indicates the boundary of the EDM loop. This boundary is estimated to be ~ 10 mm apart from the plasma grid according Figure 3-16. In z direction, electron density increases with the increasing distanced apart from the plasma grid, because the region far from the plasma grid is close to the drive region.

3.5 Plasma profile perpendicular to plasma grid and response to extraction field

The plasma in the extraction region of the negative ion source is affected by the applied extraction electric field. The results above in this chapter have revealed the increment of electron density and decrement of H^- density during beam extraction. The details of this process are illustrated in the time evolution of probe negative saturation current I_{neg} and H^- density as shown in Figure 3-17. The H^- density was measured by means of photodetachment technique. Before beam extraction, the H^- density and probe negative saturation current I_{neg} are stable. After the extraction voltage is applied, H^- density decreases immediately, and meanwhile, I_{neg} increases. This indicates that the plasma in the extraction region is influenced by the extraction electric field.

Investigation about the response of the plasma to the extraction electric field is necessary to understand the extraction process. For this purpose, a Langmuir probe with four tips was utilized to the experiment as shown in Figure 3-18. In the experiment, the probe was rotated by 30^o, so that each probe tip had different positions in y direction. Four profiles are possible to obtain at the same time by a single scan. The four probe tips are here marked as A, B, C, and D, respectively.

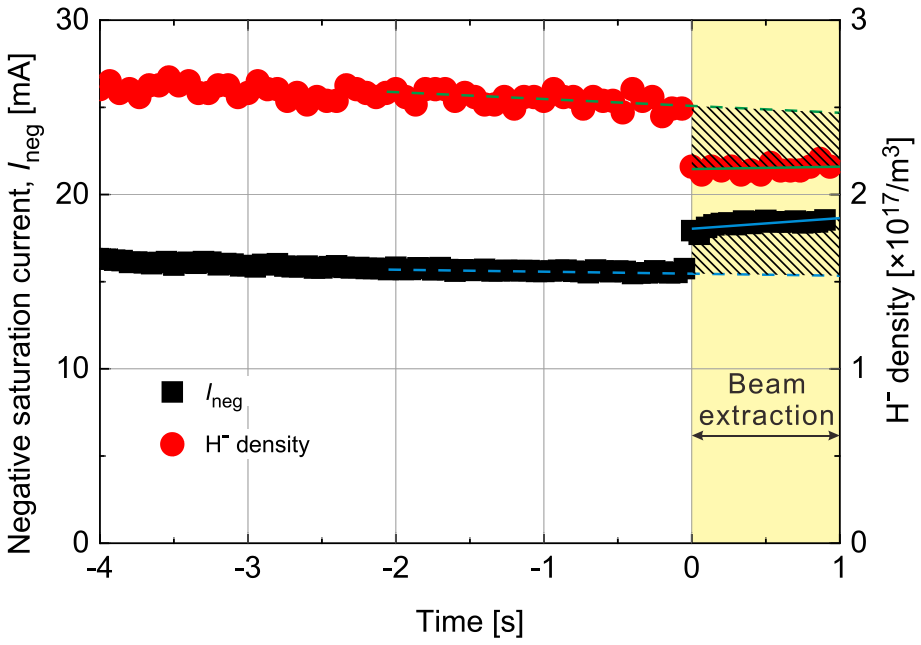

Figure 3-17. Time evolution of negative saturation current of a Langmuir probe and H^- density. Time 0 indicates the moment when the extraction voltage is applied.

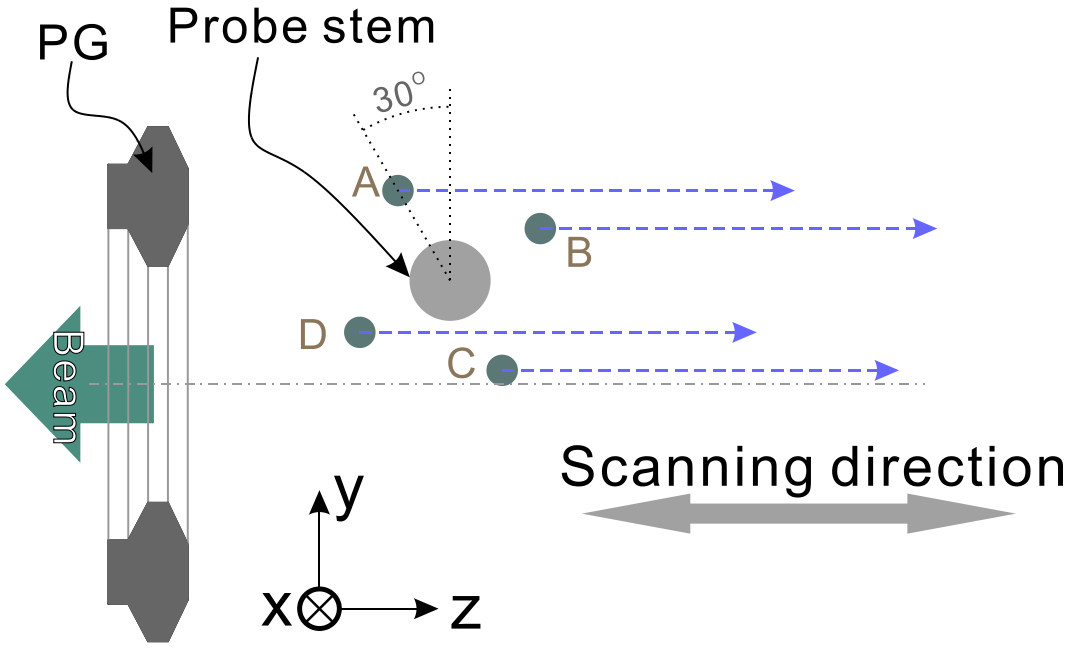

Figure 3-18. Location and scanning direction of each probe tip. The probe is rotated by 30°.

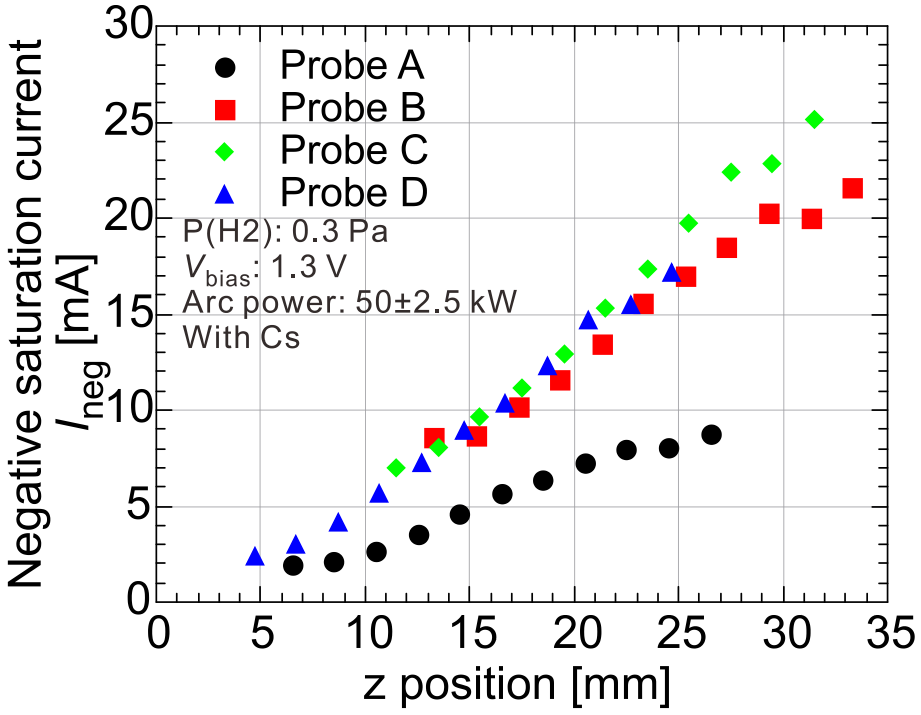

Figure 3-19. Profile of negative saturation current I_{neg} of each probe tip in z direction before beam extraction. The position z = 0 indicates the surface of the plasma grid.

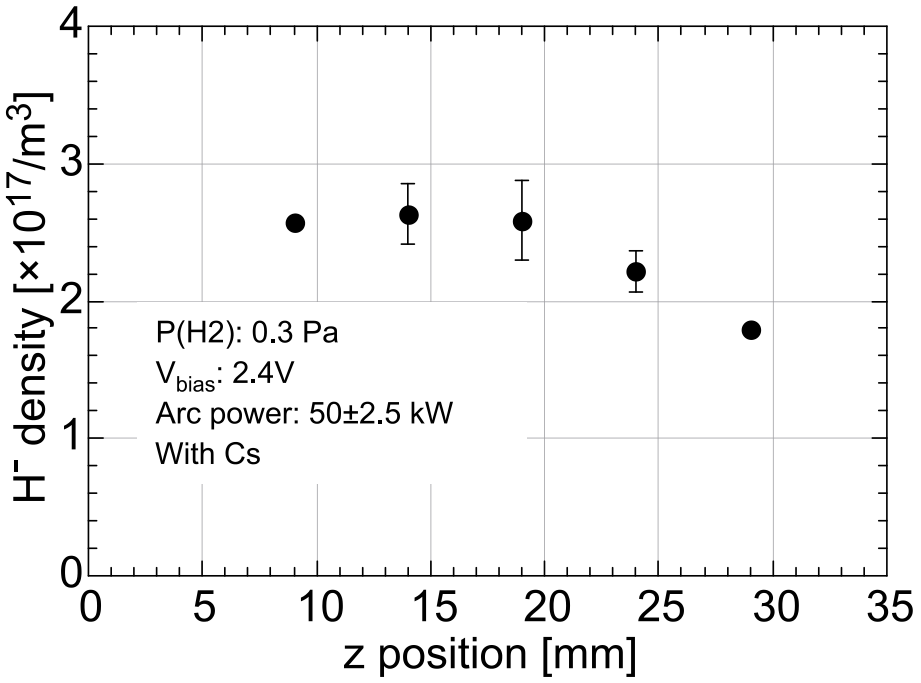

Figure 3-20. Profile of H^- density in z direction before beam extraction. The position z = 0 indicates the surface of the plasma grid.

The profiles of negative saturation current I_{neg} measured by each probe tip in z direction are shown in Figure 3-19. It is shown that I_{neg} increases almost linearly by separating from the plasma grid. This phenomenon is consistent with the result indicates in the two-dimensional distribution of I_{neg} shown in Figure 3-16. On the other hand, H^- density n_{H^-} indicated in Figure 3-20 shows a slight increase as the position moves from z = 0 mm to z = ~20 mm, and decreases when z > ~20 mm. According to the results, the extraction region is possible to be divided into three regions schematically shown in Figure 3-21. Close to the plasma, negative-ion-rich plasma is generated, because H^- ions are mainly produced on the surface of the plasma grid. Far from the plasma grid, the plasma is electron-rich plasma since this region is close to the driver region. Between the negative-ion-rich and electron-rich regions, a transition region exists.

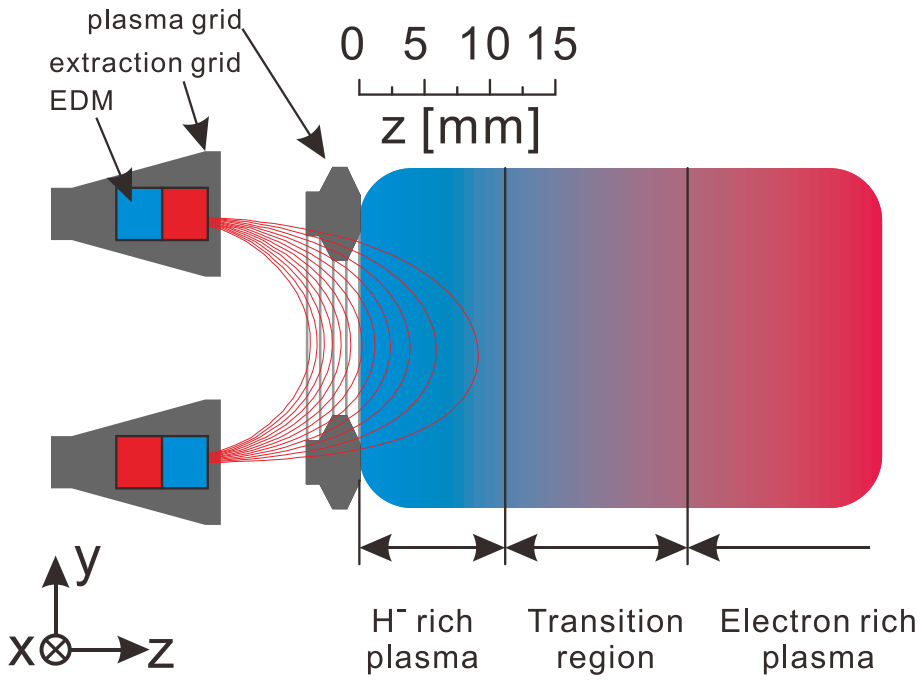

Figure 3-21. Physical picture for plasma in the extraction region.

The increment of the probe negative saturation current ΔI_{neg} cause by beam extraction is shown in Figure 3-22. Because H^- density n_{H^-} decreases during beam extraction, ΔI_{neg} represents the response of electrons to the extraction electric field. The origin of the horizontal axis z = 0 mm indicates the surface of the plasma grid. Near the plasma grid, ΔI_{neg} is lower and has a peak as the increasing distance from the plasma grid. The peak ΔI_{neg} appears at ~20 mm apart from the plasma grid. Far away from the plasma grid,

ΔI_{neg} decreases with increasing distance from the plasma grid. The linear extrapolations of the profiles diminish to 0 at $z \approx 40$ mm.

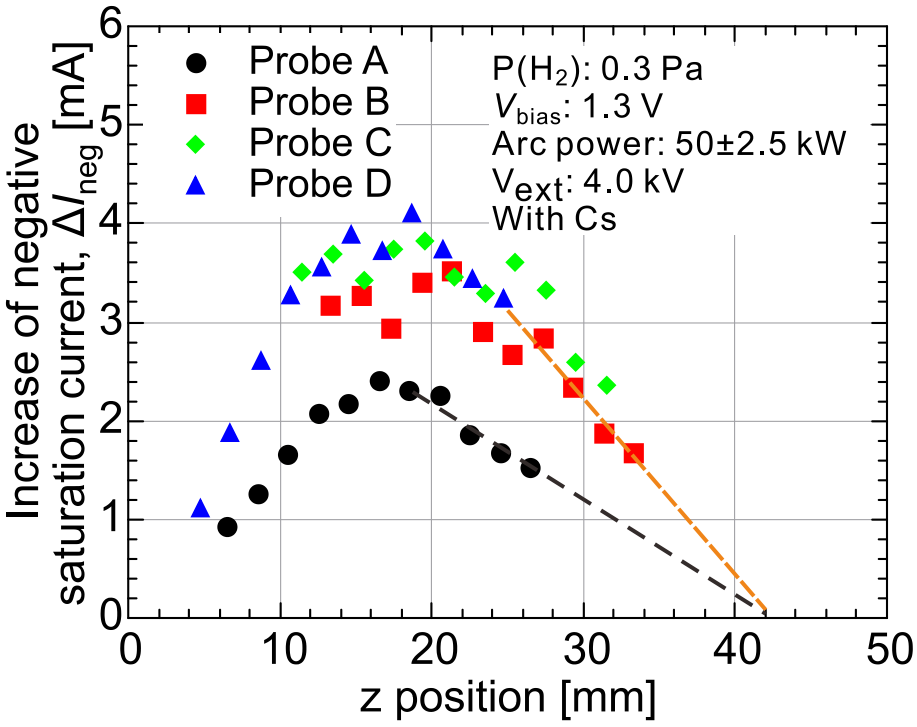

Figure 3-22. Profile of probe negative saturation current increase ΔI_{neg} due to beam extraction in z direction.

Figure 3-23 shows the profile of decrement of H^- density Δn_{H^-} caused by beam extraction in z direction. Change of H^- ion density Δn_{H^-} is low close to the plasma grid, has a peak at $z \approx 20$ mm, and decreases far from the plasma grid. This characteristic is consistent with the behavior of ΔI_{neg}. The linear extrapolation of the profile decreases to 0 at $z \approx 40$ mm, same as the position where ΔI_{neg} diminishes to 0. The results indicate the depth of the influence of the extraction electric field on the plasma reaches ~40 mm apart from the plasma grid. In addition, the maximum plasma response to the extraction electric field is at $z \approx 20$ mm

In the negative hydrogen ion source, plasma is produced in the driver region and diffuses to the extraction region across the filter field. Therefore, the plasma has low density and low temperature in the extraction region. During beam extraction the plasma

in the extraction region is indirectly influenced by the extraction electric field. On the other hand, the plasma in the driver region has high density and high temperature. This plasma is not influenced by the beam extraction electric field. Therefore, the position $z \approx$ 40 mm can be regarded as the boundary of extraction and driver regions in the RNIS.

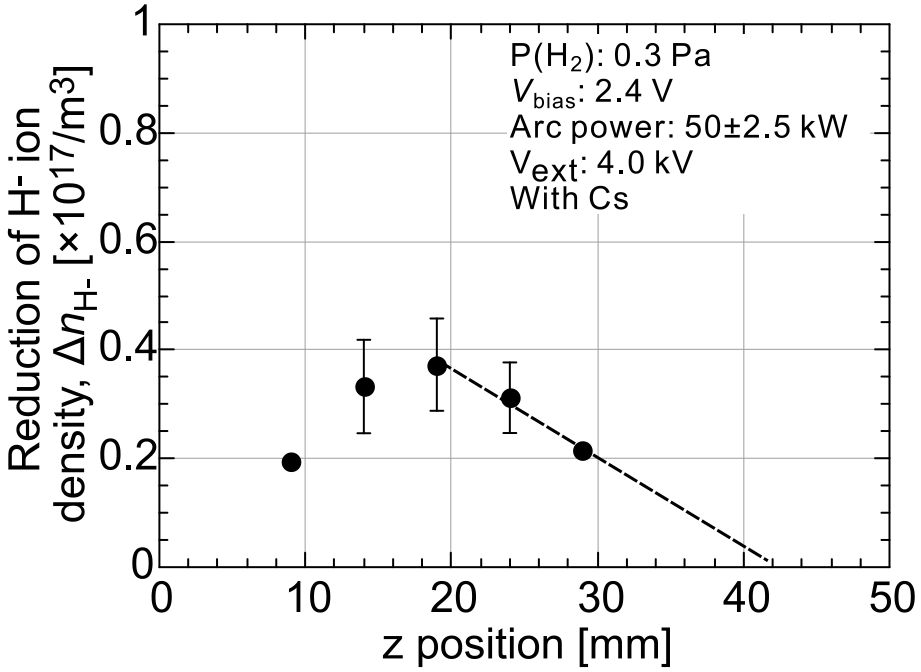

Figure 3-23. Profile of decrement of H^- density Δn_{H^-} due to beam extraction in z direction.

In the Cs-seeded negative ion source, H^- ions are mainly produced on the surface of the plasma grid. Negatively charged particles are extracted from the apertures. It is expected that the maximum response of the plasma to the extraction electric field is close to the aperture. However, the experimental results show that, far away from the plasma grid, the plasma has the maximum response to the extraction electric field. In order to understand this anomalous phenomenon, investigations on charged particle flows are required.

3.6 Summary

The characteristics of the plasma in the extraction region of the RNIS have been investigated using a Langmuir probe and photodetachment. By seeding Cs into the ion source, the H^- density n_{H^-} shows significant increase. Long Cs-conditioning time is

required for the ion source because of the complicated and slow Cs expansion. During Cs-conditioning, the plasma potential V_s decreases due to the emission of H^- ions from the plasma-grid surface. It was observed that surface-produced H^- ion density increases comparable to electron density and electron density n_e decreases as increasing H^- ion density n_{H^-} during Cs-seeding.

The plasma grid is electrically biased with respect to the plasma chamber. This bias voltage plays an important role on the plasma in the extraction region and the extraction and acceleration currents. The negative saturation current of probe I_{neg} decreases monotonically with the increasing bias voltage of the plasma grid V_{bias}. Correspondingly, the extraction current shows the same characteristic as I_{neg}. H^- ion density n_{H^-} keeps stable at negative V_{bias} and decreases slowly when V_{bias} is positive. The acceleration current shows the same behavior as that of n_{H^-}. The main function of the bias voltage applied to the plasma grid is to deplete the electrons near the plasma grid and to optimize the extraction current. Since n_{H^-} is lower at higher V_{bias}, it is necessary to apply low bias voltage to the plasma grid in order to obtain high H^- beam current with the premise of avoiding damage on the extraction grid.

Low operational gas pressure is essential for a negative ion source applied to a NBI system to reduce the stripping loss of H^- ions due to collisions with molecules and atoms. In the extraction region, n_{H^-} decreases at high pressure due to the mutual neutralization with positive ions. Decrement of temperature of positive ions due to increasing gas pressure enhances the mutual neutralization. In this process, positive ions are also depleted. Negative and positive saturation currents of the probe then shows similar tendency as n_{H^-}. As a consequence, extraction and acceleration currents are lower at higher pressure. Low operational gas pressure is beneficial to the RNIS. However, the discharge is unstable in extremely low gas pressure, because the plasma of the RNIS is sustained by electrons impact ionization and the mean free paths of the electrons become larger at lower pressure. Consequently, 0.2 to 0.4 Pa of hydrogen pressure is a proper choice for the operation of the negative ion source.

The filter field of the RNIS is a transverse magnetic field. Plasma produced in the driver region diffuses across the filter field to reach the extraction region. Therefore, the

profile of the filter field affects the distribution of the plasma in the extraction region. In the central part of the extraction region, the strength of filter field is low. Plasma easily diffuses to the extraction region. On the other hand, near the both sides of the chamber wall, the strength of the filter field is high, and the diffusion of the plasma to the extraction region is suppressed. Plasma in the extraction region concentrates in the central part of the extraction region.

Near the plasma grid, EDM filed exists. Electrons are trapped into the magnetic field on the grid metal and absorbed by the metal part of the plasma grid. The boundary of the EDM field is estimated to be ~10 mm apart from the plasma grid.

In *z* direction perpendicular to the plasma grid, the experimental results show the maximum plasma response to the extraction electric field is at ~20 mm apart from the plasma grid. The boundary of extraction region and driver region is estimated to be at ~40 mm apart from the plasma grid. During beam extraction, one can expect the maximum plasma response is close to the plasma grid. However, the results indicate that the plasma far away from the plasma has the maximum response. The understanding of this unexpected phenomenon requires the information of charged particle flows in the extraction region.

References

[1] R. L. Merlino, Am. J. Phys. **75,** 1078 (2007).

[2] K. Tsumori, H. Nakano, M. Kisaki, K. Ikeda, K. Nagaoka, M. Osakabe, Y. Takeiri, O. Kaneko, M. Shibuya, E. Asano, T. Kondo, M. Sato, S. Komada, H. Sekiguchi, N. Kameyama, T. Fukuyama, S. Wada, and A. Hatayama, Rev. Sci. Instrum. **83,** 02B116 (2012).

[3] M. Yoshida, M. Hanada, A. Kojima, M. Kashiwagi, N. Umeda, J. Hiratsuka, M. Ichikawa, K. Watanabe, L. R. Grisham, K. Tsumori, and M. Kisaki, Rev. Sci. Instrum. **87,** 02B144 (2016).

[4] R. Friedl and U. Fantz, AIP Conf. Proc. **1515,** 255 (2013).

[5] M. Bacal, M. Sasao, M. Wada, and R. McAdams, AIP Conf. Proc. **1655,** 020001 (2015).

[6] Y. Takeiri, A. Ando, O. Kaneko, Y. Oka, K. Tsumori, R. Akiyama, E. Asano, T. Kawamoto, T. Kuroda, M. Tanaka, and H. Kawakami, Rev. Sci. Instrum. **66,** 2541 (1995).

[7] R. K. Janev, C. L. Liu, J. G. Wang, and J. Yan, Europhysics Letters (EPL) **74,** 616 (2006).

[8] M. Bacal, Rev. Sci. Instrum. **79,** 02A516 (2008).

[9] A. M. Bruneteau and M. Bacal, J. Appl. Phys. **57,** 4342 (1985).

[10] G. J. M. Hagelaar and N. Oudini, Plasma Phys. Control. Fusion **53,** 124032 (2011).

[11] K. Tsumori, M. Osakabe, Y. Takeiri, O. Kaneko, K. Nagaoka, K. Ikeda, H. Nakano, Y. Oka, M. Shibuya, E. Asano, S. Komada, T. Kondo, and M. Sato, Rev. Sci. Instrum. **81,** 02B117 (2010).

4. Electron and positive ion flows

During beam extraction, it is expected that the maximum plasma response is close to the plasma grid. However, the experimental results show the influence of the extraction electric field on the plasma reaches maximum far from the plasma grid. In order to understand this anomalous phenomenon, measurements of charged particle flow are necessary.

4.1 Directional Langmuir probe

A Langmuir probe is a powerful tool for the diagnostics in low temperature plasmas. However, any general single Langmuir probes cannot give the information about plasma flow. If the tip of the Langmuir probe is partially shielded, the collection area of the probe tip is nonsymmetrical. In plasma flow, the probe saturation current is higher when the collecting surface directs to the incoming plasma flow (upstream position) and is lower when the collection surface directs to the flow direction (downstream position). The flow amplitude is then obtained from the difference of the probe saturation current at upstream and downstream positions. This special probe is named “Directional Langmuir probe” [1]. The Langmuir probes based on this concept are also called “split Langmuir probe” or “Mach probe” [2]. The directional Langmuir probe has been utilized for the measurement of plasma flow in a fusion device [2-4], ion sources [5], and other plasma devices [6]. Both of diffusion and drift caused plasma flows can be measured by the directional Langmuir probe [7]. By this tool, complicated flow structures, for example, plasma halo and plasma vortex, have also been observed [8,9].

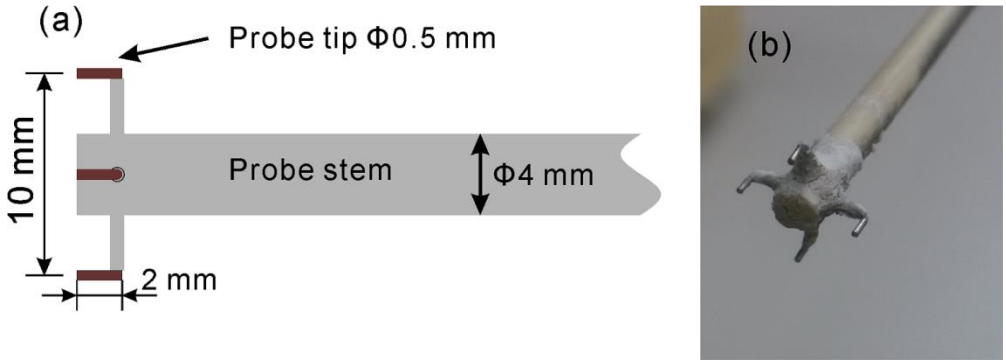

Figure 4-1. (a) Schematic illustration and (b) photograph of the four-pin directional Langmuir probe.

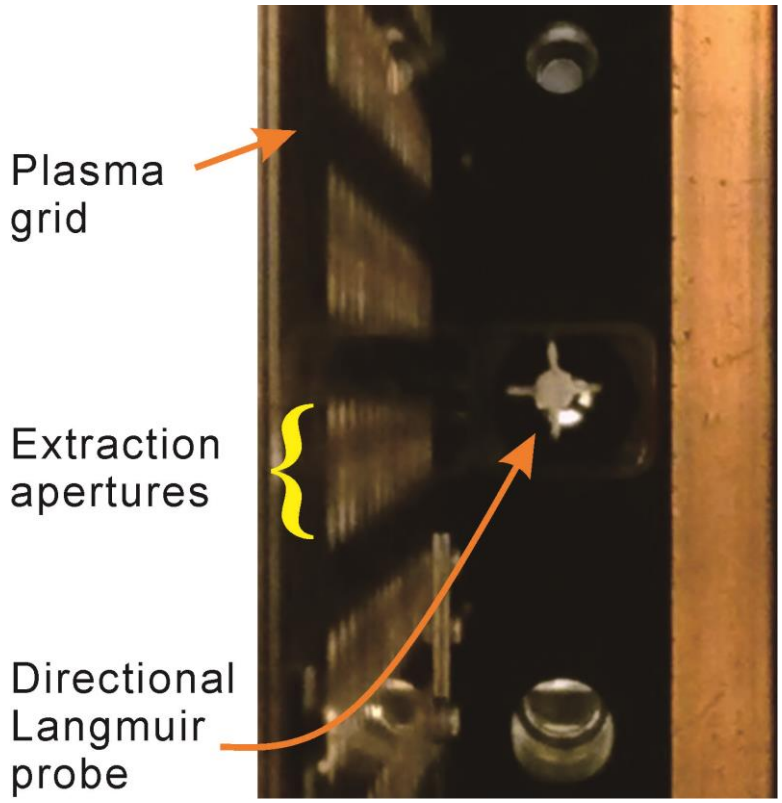

Figure 4-2. Photograph of the four-pin directional Langmuir probe in the extraction region of the RNIS.

The directional Langmuir probe applied for the measurements of charged particle flows in the extraction region of RNIS is shown in Figure 4-1. This probe has four probe

tips made of tungsten wires, whose tips are 0.5 mm in diameter and 2 mm in length and their arms are covered by ceramic. The distance between two opposite tips is 10 mm and the four tips are arranged at rectangle positions with the same distances of 5 mm from the center ceramic stem. The purpose of this distance is to leave a space for the laser beam, because photodetachment technique is also applied to this four-pin directional Langmuir probe for the measurement of H^- ion flow. Interaction of the laser beam and the probe stem can be avoided to reduce the influence of the scattered laser to the experiment by the L-shaped probe tips. Figure 4-2 shows the four-pin directional Langmuir probe installed in the extraction region of the RNIS through the bias insulator. On the left side of this photograph, the plasma grid is shown. On the plasma grid, extraction aperture series can also be observed. A cupper-colored vertical band on the right side in this photograph is the protector for the filter magnet, and driver region is located at further right of the protector. The plasma grid is shown on the left side, and the arrays of extraction apertures are seen on the plasma grid.

4.2 Identification of electron and positive ion flows

4.2.1 Flow direction

If the plasma is not flowing, a directional Langmuir probe should collect the same saturation currenst I_{sat} to all the tips by turning the probe facing to any direction. In a plasma flow with the existence of a magnetic field as illustrated in Figure 4-3, I_{sat} measured by a directional Langmuir probe is not isotropic in any direction, and is corrected to be [6,10]

$$I_{sat}(n) = I_{sat} \cdot (1 + F_v(v, n)) \cdot (1 + F_B(B, n)), \tag{4-1}$$

where n is a unit vector indicating the normal direction of the directional Langmuir probe, F_v is a correction coefficient for the effect of plasma flow, v is the flow velocity, F_B is a coefficient for the effect of magnetic field, and B is the magnetic field. The directional Langmuir probe can collect the maximum current if it is facing to the incoming direction of the flow ($n \parallel -v$) and the minimum current if it is facing to the downstream direction of

the flow ($n \parallel v$). With the assumption of constant flow in the probe position, F_v is expressed as [6,10]:

$$F_v = -\alpha(v \cdot n), \tag{4-2}$$

where α is a positive coefficient.

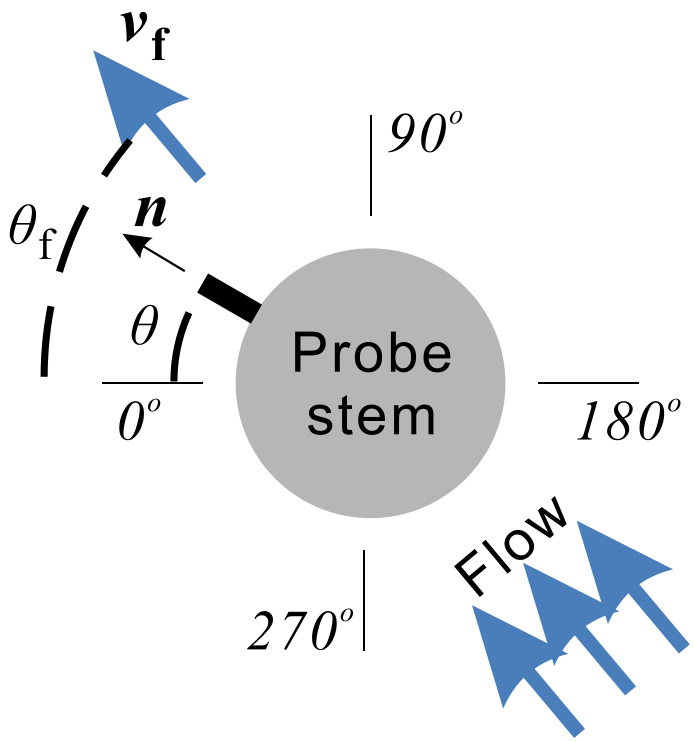

Figure 4-3. A directional Langmuir probe in a plasma flow.

Considering the effect of the magnetic field, the probe can collect maximum current if its normal vector is parallel to the magnetic field ($n \parallel B$ or $n \parallel -B$), and minimum current if the normal direction of the directional Langmuir probe is perpendicular to the magnetic field ($n \perp B$). With the assumption of constant magnetic field, F_B is expressed as [6,10]:

$$F_B = \beta(B \cdot n)^2, \tag{4-3}$$

where β is a coefficient.

By collecting the expressions of F_v and F_B indicated in Equation 4-2 and 4-3, Equation 4-1 is then rewritten as:

$$I_{\text{sat}}(n) = I_{\text{sat}} \cdot (1 - \alpha' \frac{v}{C_s} \cdot n) \cdot (1 + \beta' \frac{\rho^2}{r_p^2} (b \cdot n)^2), \tag{4-4}$$

where C_s is the ion sound speed, ρ is the Larmor radius, and r_p is the radius of the tip of the directional Langmuir probe. These three quantities are introduced to normalize the correction coefficients. ***b*** is the unit vector of the magnetic field ***B***.

Since $F_B(n) = F_B(-n)$, the effect of magnetic field to the measurement can be eliminated by considering the quantity $I_{sat}(n) / I_{sat}(-n)$ [6,10]:

$$\frac{I_{\text{sat}}(n)}{I_{\text{sat}}(-n)} = \frac{I_{\text{sat}}(\theta)}{I_{\text{sat}}(\theta + \pi)} = \frac{1 - \alpha' \frac{v}{C_s} \cdot n}{1 + \alpha' \frac{v}{C_s} \cdot n}, \tag{4-5}$$

where θ is the rotation angle of the directional Langmuir probe defined in the experiment. It can be derived from Equation 4-5 that:

$$\alpha' \frac{v}{C_s} \cdot n = \alpha' \frac{v \cdot \cos(\theta - \theta_f)}{C_s} = \frac{I_{\text{sat}}(\theta + \pi) - I_{\text{sat}}(\theta)}{I_{\text{sat}}(\theta + \pi) + I_{\text{sat}}(\theta)}. \tag{4-6}$$

Equation 4-6 can also be written as:

$$\frac{I_{\text{sat}}(\theta + \pi) - I_{\text{sat}}(\theta)}{I_{\text{sat}}(\theta + \pi) + I_{\text{sat}}(\theta)} = \alpha \cdot v \cdot \cos(\theta - \theta_f). \tag{4-7}$$

The term $I_{sat}(\theta+\pi)$-$I_{sat}(\theta)$ is the difference of the probe saturation current at two opposite positions, and can be written as δI_{sat}. On the other hand, the term $I_{sat}(\theta+\pi)+I_{sat}(\theta)$ represent the average probe saturation current $\langle I_{sat} \rangle$, and $I_{sat}(\theta+\pi)+I_{sat}(\theta) = 2\langle I_{sat} \rangle$. Then Equation 4-7 is modified to be

$$\frac{\delta I_{\text{sat}}}{< I_{\text{sat}} >} = \frac{I_{\text{sat}}(\theta + \pi) - I_{\text{sat}}(\theta)}{\frac{I_{\text{sat}}(\theta + \pi) + I_{\text{sat}}(\theta)}{2}} = 2\alpha \cdot v \cdot \cos(\theta - \theta_f). \tag{4-8}$$

Equation 4-8 shows a characteristic of a shifted cosine function. Therefore, the flow angle θ_f can be determined by performing function fitting to the experimental data of $\delta I_{sat}/\langle I_{sat} \rangle$.

4.2.2 Flow speed

Flow angle θ_f in Equation 4-8 is possible to be determined by applying function fitting method to the experimental data of directional probe. However, the flow velocity is impossible to obtain in this process because of the two unknown variables α and v. One of the methods to obtain the coefficient α is to calibrate the directional Langmuir probe in the plasma with a known flow. A preferable approach is to put the directional Langmuir probe in a crossed field ($E \times B$ field) with specific magnetic field B and known electric field E. Since the flow speed of the plasma in the cross field is $v = E/B$ [11], α is determined from the data of directional Langmuir probe. The flow speed v can be derived with known α and θ_f. In the RNIS, the plasma flow in the extraction region is not dominated only by $E \times B$ drift. This calibration method is thus not available in this case.

An alternative of the calibration method is to estimate the flow speed from the saturation current of the directional Langmuir probe directly. Several works has been conducted to interpret the data of a directional Langmuir probe and to evaluate the flow speed [1-3,12,13].

The fundamental concept of the operation of a directional Langmuir probe is that the flow speed of charged particles is possible to evaluate by the difference of the saturation current collected by the probe which faces to two opposite directions. If the saturation current densities of the directional Langmuir probe facing to the upstream and downstream directions are j^+ and j^-, a relation between the ratio $R = j^+/ j^-$ and Mach number of the flow $M = v/C_s$ can be developed. v is the flow speed and C_s is the ion sound speed

$$C_s = \sqrt{\frac{k(T_e + T_i)}{\pi m_i}}, \tag{4-9}$$

where k is the Boltzmann constant, T_e and T_i are temperatures of electrons and positive ions, and m_i is the mass of a positive ion.

Chung et al. showed that the ratio R can be written quite accurately as [12,14]

$$R = \frac{j^+}{j^-} = e^{KM}. \tag{4-10}$$

Note that K is in uppercase and is a new constant and is introduced to determine the flow speed in the plasma.

In the case of positive ion, the current density is indicated as the following equation [2]

$$j^{\pm} = q\sqrt{kT_e / m_i}\left(n_i / \sqrt{e}\right)\exp\left[\frac{\left(v_{\text{th}}^2 + v^2\right)m_i}{2kT_e}\right]\exp\left(\frac{\pm v_{th} v m_i}{kT_e}\right). \tag{4-11}$$

where q is the charge, v_{th} is the thermal speed, e is the Euler's number and ln e = 1, n_{i} is the density of positive ions.

By Equation 4-11, the ratio R is given by

$$R = \frac{j^+}{j^-} = \exp\left(\frac{2v_{th} v m_i}{kT_e}\right) = \exp\left(2M\frac{\sqrt{2(T_e T_i + T_i^2)}}{T_e}\right). \tag{4-12}$$

The required K is then derived as [2]

$$K = 2\frac{\sqrt{2(T_e T_i + T_i^2)}}{T_e}. \tag{4-13}$$

The Mach number of the flow in plasma is then given by

$$M = \frac{\ln R}{K}. \tag{4-14}$$

The flow speed can be calculated by M and C_{s}

4.3 Electron and positive ion flow in pure hydrogen plasma

4.3.1 Flow direction

In the experiments, the directional Langmuir probe had four probe tips as described in Section 4.2.1. Since the four tips have the same surface area and the angle between two neighbor tips is 90$^{\text{o}}$, the polar distribution of the probe saturation current can be obtained by rotating the directional Langmuir probe by 90$^{\text{o}}$. The probe data at four different

azimuthal angles were obtained at the same time and it reduced the total experimental time to obtain full angular distribution significantly.

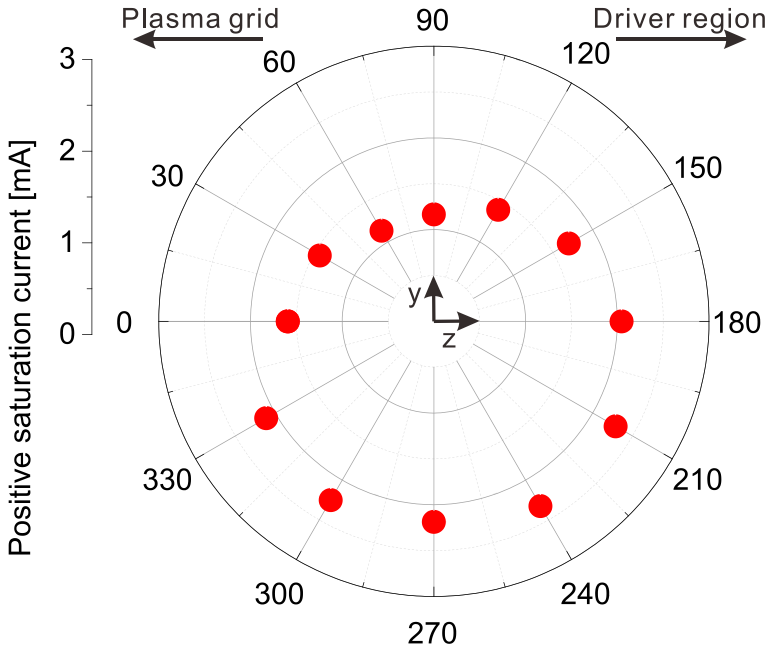

Figure 4-4. Polar distribution of probe positive saturation current at 19 mm apart from the plasma grid (z = 19 mm).

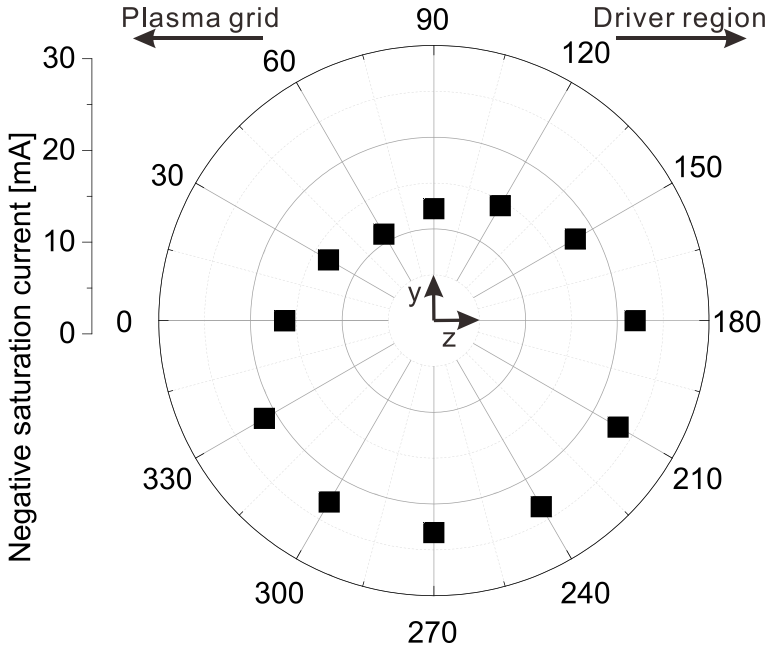

Figure 4-5. Polar distribution of probe negative saturation current at 19 mm apart from the plasma grid (z = 19 mm).

In Cs-seeded plasma, the plasma in the extraction region of the RNIS forms negative-ion-rich plasma. The negative saturation current of the probe contains both electron and H^- ion components. Information about electron flow is difficult to obtain directly from the data of the directional Langmuir probe. For this reason, pure hydrogen plasma, not including Cs, is applied for the measurements of electron and positive ion flows.

Four polar distribution of probe data was obtained by rotating this probe every 30° in the azimuthal direction around the axis of the ceramic stem. The results at 19 mm apart from the plasma grid are shown in Figure 4-4 and Figure 4-5, which are the distributions of positive saturation current and negative saturation current, respectively. The negative saturation current is one order higher than the positive saturation current, because electron current is included in the former current. Both of the two distributions have the maximum values at ~240°. This phenomenon suggests possible incoming flows of electrons and positive ions are from this direction.

Equation 4-8 indicates that the quantity $\delta I_{sat}/\langle I_{sat}\rangle$ has a form of $\cos(\theta-\theta_f)$. Also, the probe saturation current $I_{sat}(\theta)$ shows a periodic distribution with a period of 2π as shown in Figure 4-4 and Figure 4-5. $I_{sat}(\theta)$ can be resolved into Fourier series

$$I_{sat}(\theta) = \sum_{m=1}^{N} A_m \cdot \cos(m \cdot (\theta - \theta_m)) \quad (m = 1, 2, 3 \ldots). \tag{4-14}$$

For $m = 1$, $\theta_1 = \theta_f$. Taking the positive saturation current data shown in Figure 4-4 as an example, the amplitude for each component $m = 1$ to 6 is shown in Figure 4-6. For $m = 1$, A_1 is ~0.62 and for $m = 2$, A_2 is ~0.07. The Fourier amplitude for $m \geq 2$ is one order lower than that of $m = 1$. It is reasonable that the Fourier components for $m \geq 2$ can be omitted. Function fitting to the quantity $\delta I_{sat}/\langle I_{sat}\rangle$ gives the flow direction. It has been mentioned in Chapter 3 that the plasma in z direction is not uniform and has a distribution. Deviation of the saturation current δI_{sat} includes a component caused by the spatial profile of the plasma in z direction which is shown in Figure 4-7.

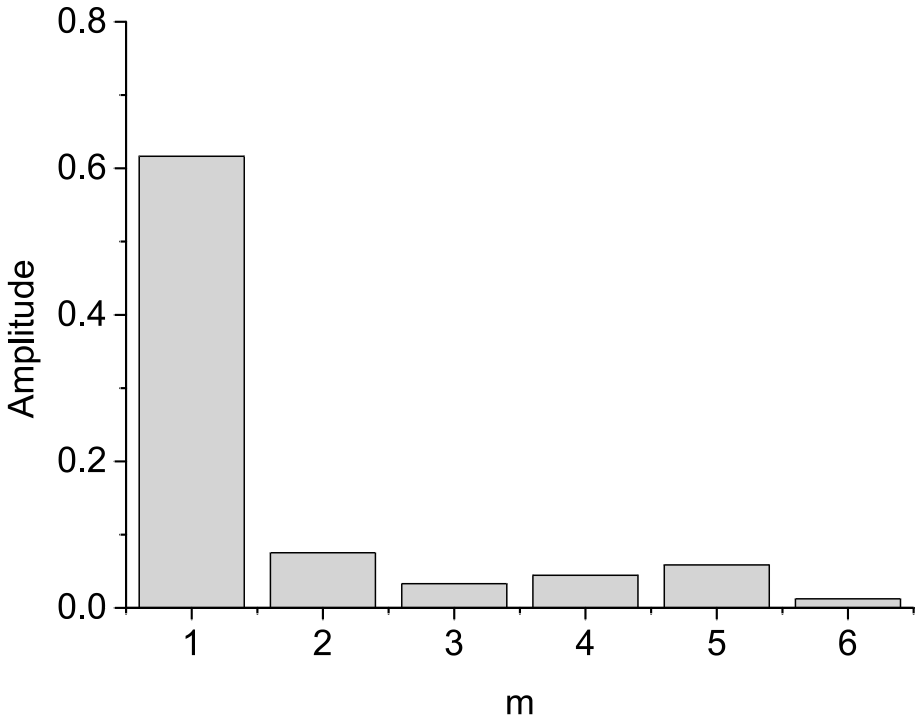

Figure 4-6 Fourier amplitude for m = 1 to 6.

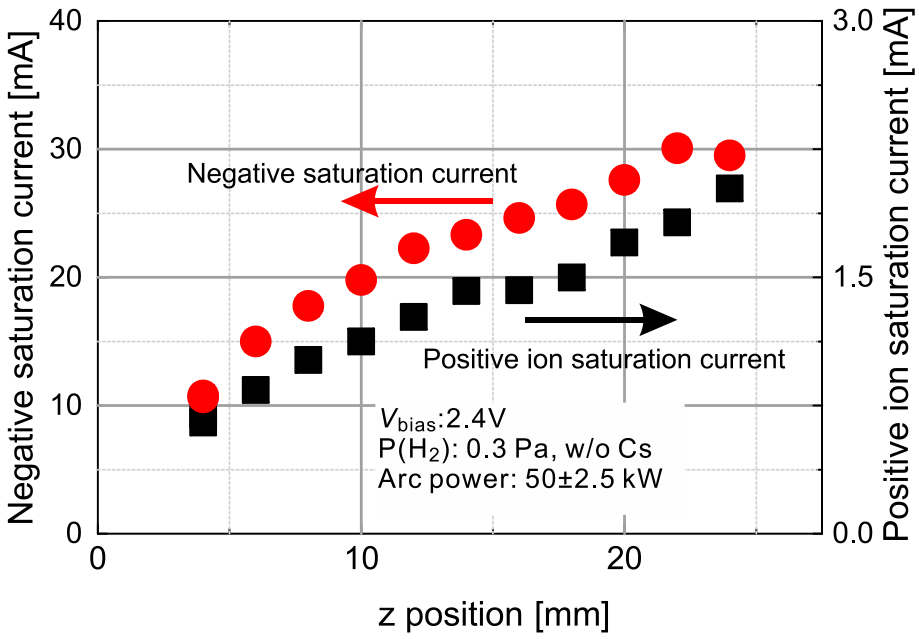

Figure 4-7. Profiles of negative and positive saturation currents in z direction.

Linear correction is applicable for the deviation δI_{sat} as schematically illustrated in Figure 4-8. The solid line indicates the linear profile of positive or negative saturation current and is expressed as $I_{sat} = k' L + D$, where k' is a factor for the linear relation, L is the distance from the plasma grid, and D is the saturation current at $z = 0$. The quantity

$\langle I_{sat} \rangle = [I_{sat}(\theta+\pi)+I_{sat}(\theta)]/2$ is not affected by the linear profile. At the angle $\theta = 0$, the deviation $\delta I_{sat} = I_{sat}(\theta+\pi)-I_{sat}(\theta)-\Delta I_{sat}$, by subtracting the influence ΔI_{sat} caused by the profile. ΔI_{sat} varies with the azimuthal angle θ, and is expressed as $\Delta I_{sat}(\theta) = k' \cdot \Delta L \cos(\theta) = \Delta I_{sat} \cos(\theta)$. Finally, the required δI_{sat} is given by

$$\delta I_{sat}(\theta) = I_{sat}(\theta + \pi) - I_{sat}(\theta) - \Delta I_{sat} \cdot \cos(\theta) . \qquad (4\text{-}15)$$

The corrected quantity $\delta I_{sat}/\langle I_{sat} \rangle$ is then fitted by function $A_1 \cos(\theta-\theta_f)$ as shown in Figure 4-9. The function fitting provide the flow angle $\theta_f = 82.9 \pm 1.7^o$. The direction of the flow at z = 19 mm is then determined.

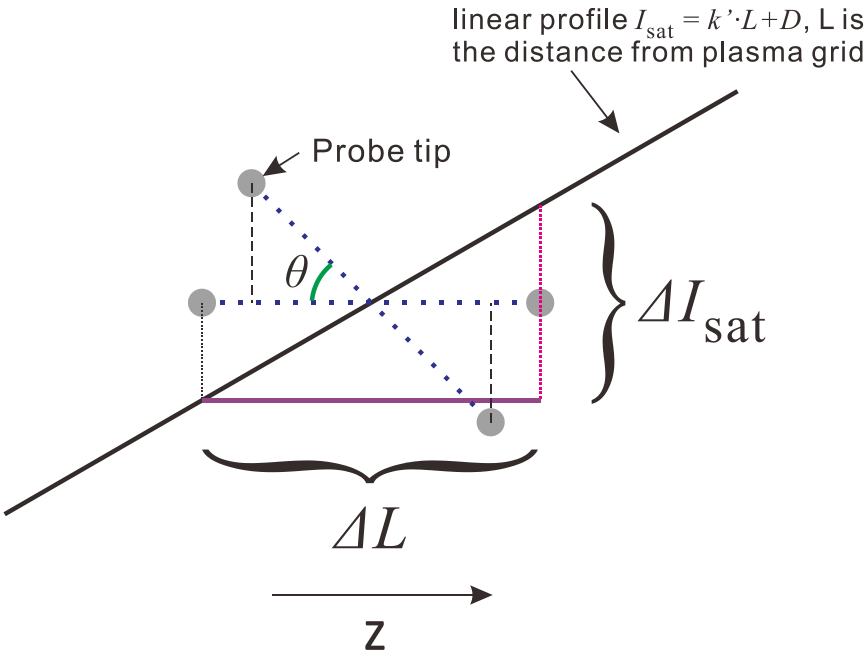

Figure 4-8. Correction method for δI_{sat}.

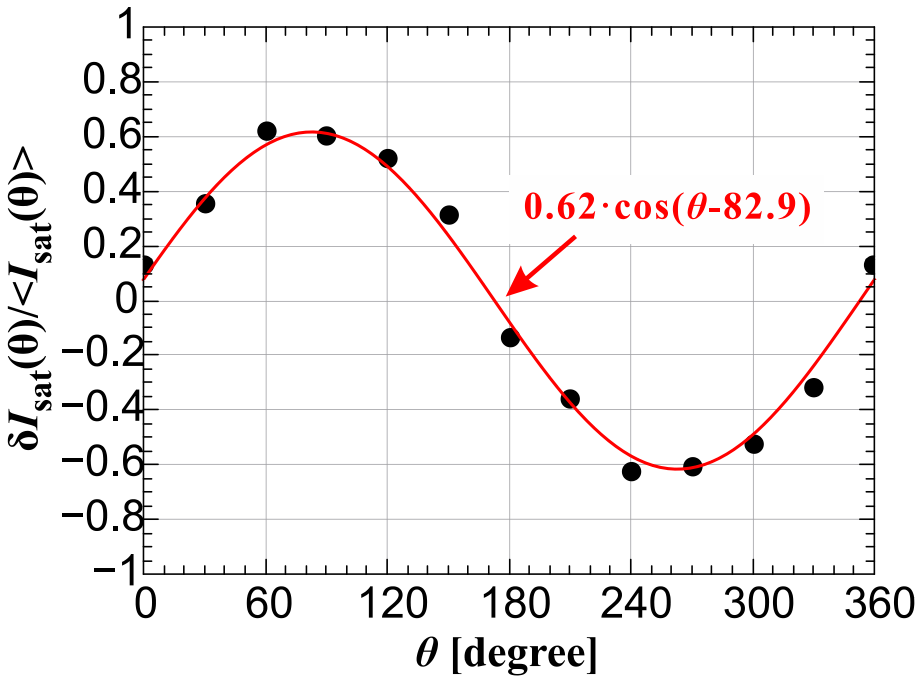

Figure 4-9. The quantity $\delta I_{sat}/\langle I_{sat}\rangle$ fitted by function $A_1 \cos(\theta-\theta_f)$.

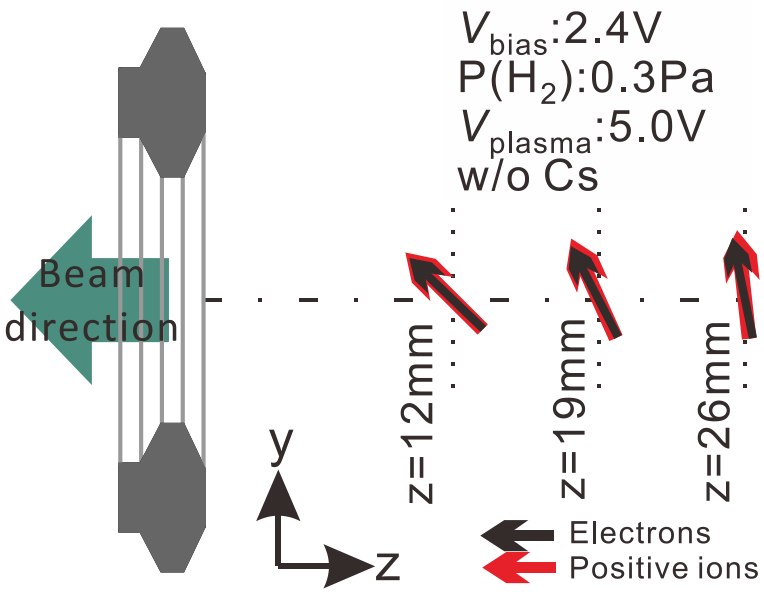

Figure 4-10. Flow directions of electrons and positive ions in pure hydrogen plasma.

The non-centrosymmetric characteristic of the polar distribution of negative saturation current indicates the electron flow. By the same procedure as calculating the positive ion flow direction, the electron flow direction also has been obtained. Both flow

directions of electrons and positive ions at z = 12, 19, and 26 mm are shown in Figure 4-10. Almost the same flow directions of electrons and positive ions were ontained in the expeiments. It indicates the movement of electrons and positive ions is ambipolar.

4.3.2 Flow speed

Figure 4-10 shows that the plasma flow can be separated into y and z components. In y direction, the flow speed is estimated from the discussion in Section 4.2.2. In the pure hydrogen plasma at 2.4 V of bias voltage of the plasma grid Vbias and 0.3 Pa of hydrogen pressure, the electron temperature is evaluated to be 0.65 eV by a Langmuir probe. The positive ion temperature is assumed to be 0.3 eV which is the same as the temperature of the filaments of the ion source. In addition, the hydrogen atom temperature has been measured by means of laser absorption spectroscopy and has been evaluated to be ~0.3 eV [15]. It is reasonable to assume positive ions have the same temperature as hydrogen atoms. According to Equation 4-9, the ion sound speed is $\sim 1 \times 10^4$ m/s. The ratio of the saturation current densities of the directional Langmuir probe measured by probe tips at upstream and downstream positions is R=2.4. The important coefficient K is calculated to be K = 2.32 according to Equation 4-13. The Mach number is then estimated as M = 0.38 according to Equation 4-14. Finally, flow speed in y direction is $v_y = M \cdot C_s$ = 3800 m/s. The speed of flow in z direction v_z can be calculated from $v_z = v_y/\tan(\theta_f)$ = -470 m/s, where $\theta_f = 83^o$ is the flow angle at z = 26 mm.

In the extraction region of the RNIS, the profile of plasma potential suggests an electric field E = 25 V/m exists as shown in Figure 4-11. Since the filter field perpendicular to this electric field is 0.006 T. The crossed electric and magnetic field causes a drift in y direction to the charged particles. The speed of the drift is $v_d = E/B \approx$ 4200 m/s which is consistent with the measured flow speed in y direction. This suggests electron and positive ion flows in y direction is dominated by $E \times B$ drift.

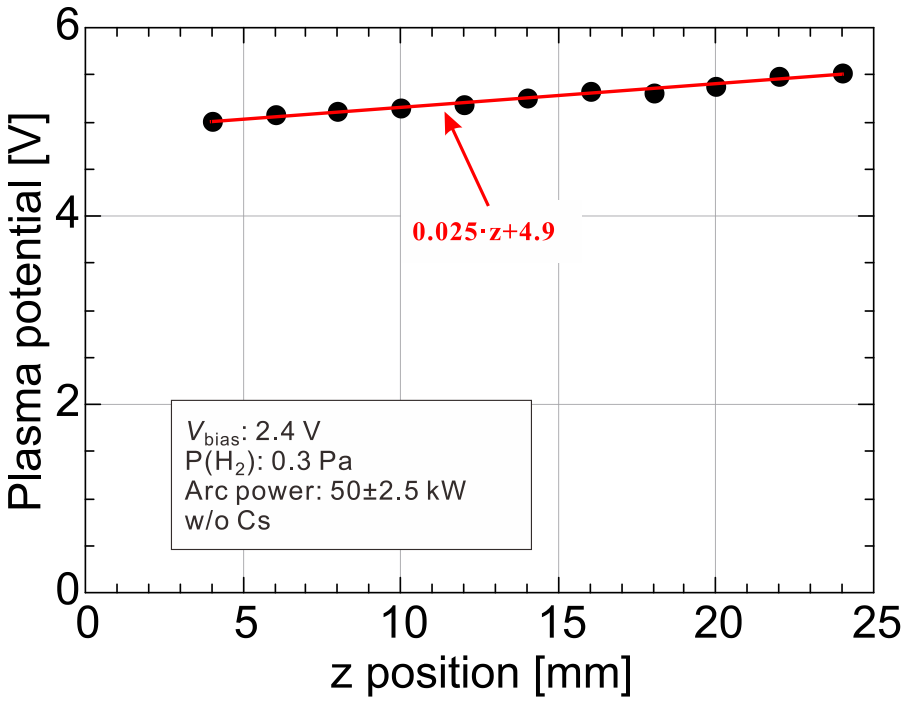

Figure 4-11. Profile of plasma potential in z direction.

The flow in *z* direction towards plasma grid and is considered to be caused by collisions. The flow speed is [11]

$$v_z = \mu \cdot E + D\frac{-\nabla n}{n}, \tag{4-16}$$

where μ is the mobility of electrons. With the assumption of ambipolar diffusion across the magnetic field, electron flow has the same speed as positive ion flow Diffusion coefficient and plasma density are denoted with *D* and *n*, respectively. Without magnetic field, the electron mobility is given by

$$\mu_0 = \frac{q}{m \cdot \nu_m}, \tag{4-17}$$

where *q* and *m* are the charge and mass of an electron, respectively. ν_m is the effective collision frequency for momentum transfer. In a magnetic field, electron mobility decreases because of the confinement by the magnetic field and is given by [11,16,17]:

$$\mu = \frac{q}{m \cdot \nu_m} \cdot \frac{1}{1+\frac{\omega_e^2}{\nu_m^2}}, \tag{4-18}$$

where ω_e is the electron-cyclotron frequency.

Both of the electron-neutral collision and electron-positive ion collision transfer the momentum. The electron-neutral collision frequency is proportional to the hydrogen pressure. For 0.3 Pa of hydrogen, the collision frequency is ~1×10^7/s [18]. The frequency for momentum transfer between electrons and positive ions is given by [19]

$$\nu_{ei} = 2.9\times10^{-12} n_i \left(\frac{kT_e}{q}\right)^{-3/2} \ln\Lambda, \tag{4-19}$$

where n_i is the density of positive ions and is assumed equal to the electron density since the plasma is pure hydrogen plasma without Cs and the position is far away from the plasma grid, and $n_i = n_e = 3\times10^{17}/m^3$ is measured by the Langmuir probe. For Equation 4-19, $\ln\Lambda$ is given by $\ln\Lambda = 10$ which is sufficiently accurate regardless of the type of the plasma [11]. The electron-ion collision frequency ν_{ei} is then calculated to be $\nu_{ei} = 1.7\times10^7$/s. Therefore, the effective momentum transfer frequency is $\nu_m = 2.7\times10^7$/s. According to Equation 4-18 the electron mobility is $\mu = 4\ m^2/(V\ s)$.

The diffusion coefficient D is given by

$$D = \nu_m \left(1 + \frac{T_i}{T_e}\right) r_e^2, \tag{4-19}$$

where r_e is the Larmor radius of electrons. Finally, the flow speed in z direction is estimated to be -240 m/s. The symbol "-" indicates the flow is to the negative direction of z.

Table 4-1. Summary of electron and ion flow velocities at z = 26 mm.

	v_y (m/s)	v_z (m/s)
Probe measurement	3.8×10^3	-470
Crossed-field and ambipolar diffusion estimations	4.2×10^3	-240

The flow speeds in both *y* and *z* directions are summarized in Table 4-1. The results suggest the electron and positive ion flows are dominated by crossed-field drift in *y* direction and ambipolar movement in *z* direction.

4.4 Two-dimensional flow pattern

From the one-dimensional flow measurement results discussed in Section 4.3, it became clear that electron and positive ion flows are dominated in y direction by crossed-field drift and ambipolar diffusion in z direction. Consequently, flow of electrons follows that of positive ions.

The flow in negative-ion-rich plasma with Cs-seeding is more interesting. Therefore, flow measurements were conducted in the plasma with well Cs-conditioning. The measurement points were scanned two-dimensionally, and flow patterns of electrons and positive ions have been obtained.

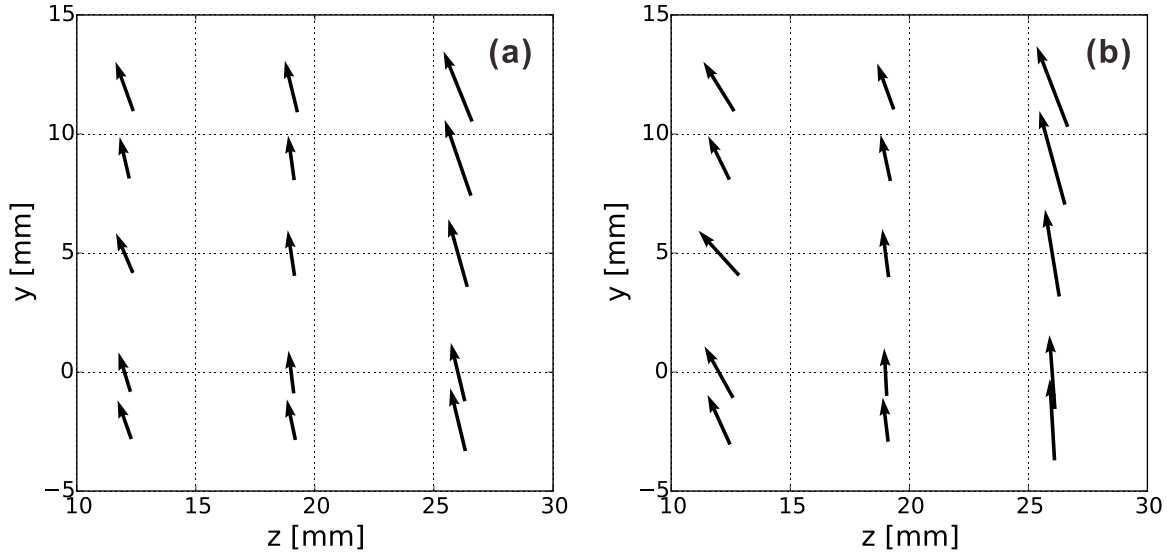

Figure 4-12. Arrow plot of the two-dimensional flow pattern. (a) before beam extraction and (b) during beam extraction

Figure 4-12 shows the two-dimensional flow pattern of positive ions before and during beam extraction in negative-ion-rich plasma with Cs-seeding. Since electron flow follows positive ion flow, the flow pattern shown in Figure 4-12 is possible to represent the electron flow. Note that in y direction, $y = 0$ indicates the central axis of the extraction aperture. However, this arrow plot includes only fifteen measurement points. In order to obtain clear feature of the two-dimensional flow pattern, interpolation was applied to the arrow data and streamline plot of the flow pattern has been acquired.

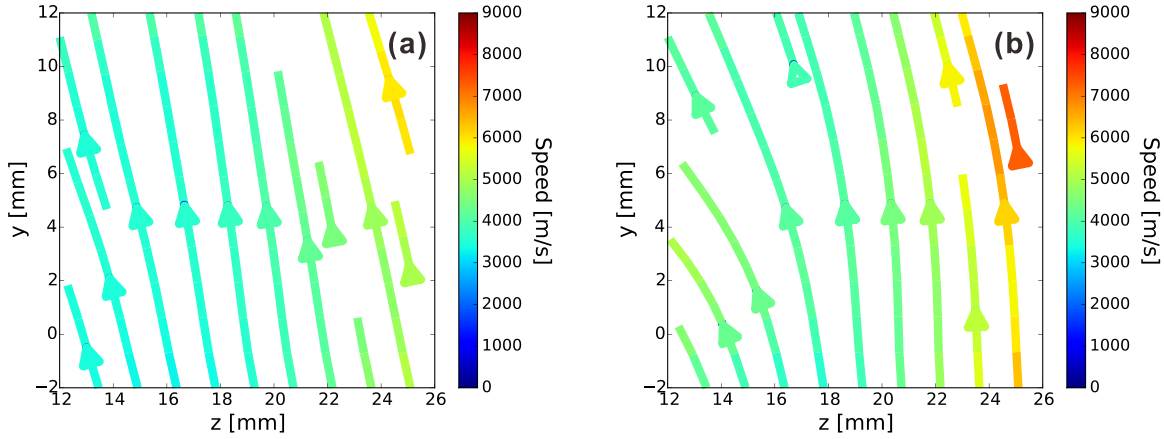

Figure 4-13. Steamline plot of the two-dimensional flow pattern. (a) before beam extraction and (b) during beam extraction

Figure 4-13 shows the flow pattern of positive ions with more details before and during beam extraction. It can be found that in negative-ion-rich plasma, the streamlines are almost parallel in the measurement region. During beam extraction, H^- density decreases and additional electrons appear in the measurement region. The streamlines near the plasma grid bend to the metal part of the plasma grid. A possibility is that the additional electrons induced by beam extraction are affected by the EDM field illustrated in Figure 3-16 and Figure 3-21. In order to put forward a clear physical picture, the flow pattern is plotted with the plasma grid and shown in Figure 4-14. In this figure, the measurement region with respect to the plasma grid is demonstrated. The flow pattern in Figure 4-14 is the flow during beam extraction and same as Figure 4-13 (b).

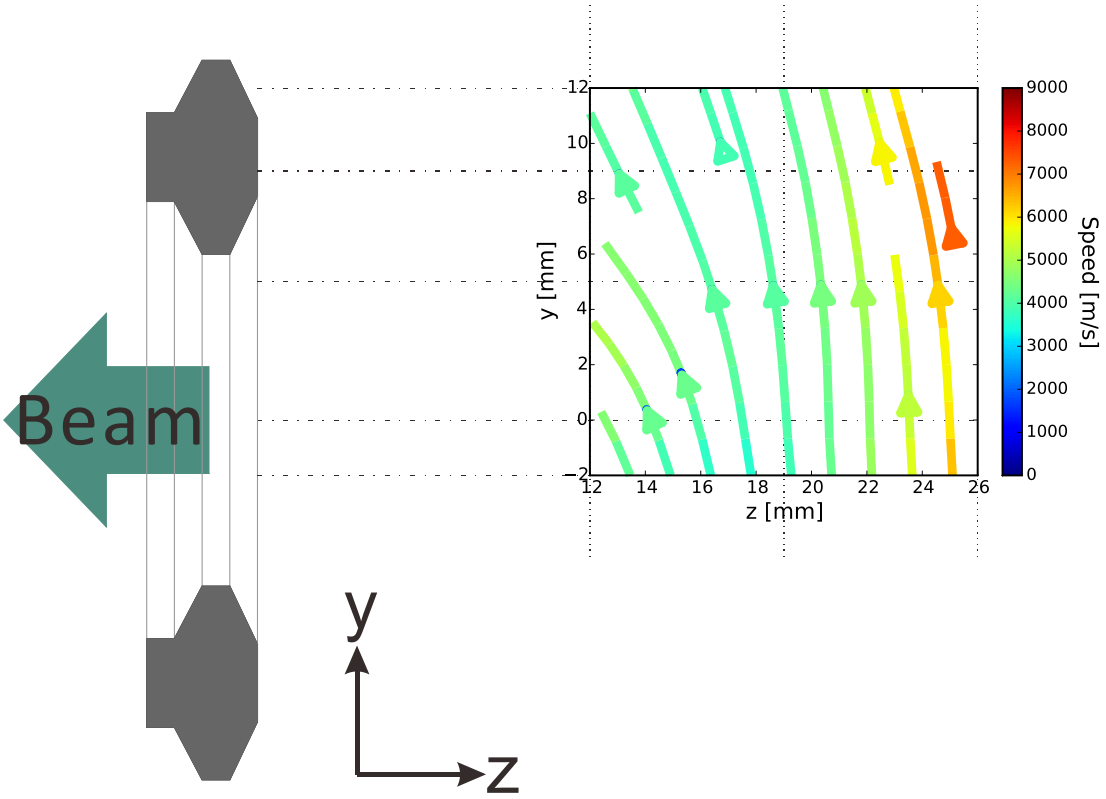

Figure 4-14. Two-dimensional flow pattern of positive ions during beam extraction. The measurement region is indicated. The cross points of dash lines are the measurement positions.

The influence of the extraction electric field to the plasma can be investigated by the change of the positive ion flow caused by the beam extraction. Subtracted pattern of the flow before beam extraction from that during beam extraction is obtained and indicated in Figure 4-15. In this figure, both of the EDM field and plasma grid are plotted. Considering the flow pattern before beam extraction as a background and the transition of flow occurs is in a finite time, the change of the flow velocity can be regarded as the additional fluxes of electrons and positive ions induced by beam extraction. The flux increases come from lower side to upper side in this figure and are flowing in a channel which is ~20 mm apart from the plasma grid. If a Langmuir probe is located in this channel, the maximum plasma response can be detected. This characteristic is consistent with the plasma response shown in Figure 3-22. The change of the flow goes the cusp region of the EDM field. During beam extraction, additional electrons and positive ions flow to the extraction region from the driver region, and cause the flux increases. The extraction induced additional electrons and positive ions, included in the flux increments,

are trapped into the magnetic cusp and absorbed by the metal part of the plasma grid. The two-dimensional flow pattern shown in Figure 4-15 does not show a source of the flux. This phenomenon suggests these electrons and positive ions may come from perpendicular direction of the *y*-*z* plane following the filter field, because charged particles have higher mobility along the magnetic field lines than that perpendicular to the magnetic field lines.

The flow change is the difference between the stable plasma flows before and during beam extraction with a time interval Δt. If Δt is considered as the time interval just before and after the extraction voltage is applied. The force direction can be derived since $a = \Delta v/\Delta t$, where a is the acceleration and Δv is the change of the flow velocity. Therefore, the streamlines shown in Figure 4-15 also indicate the direction of force applied to the positive ions caused by beam extraction.

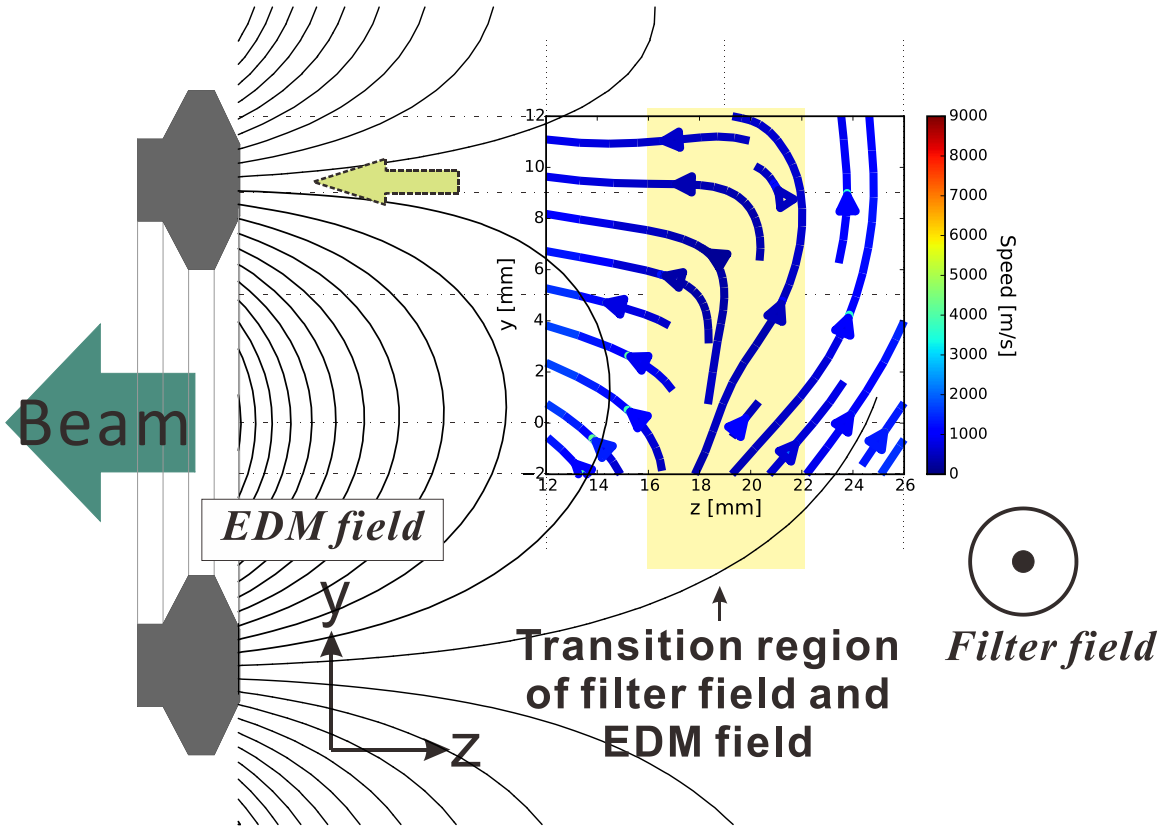

Figure 4-15. Change of positive ion flow due to beam extraction. The EDM field is also shown.

In the beam extraction region of the RNIS, both of the EDM field and filter field exist. Close to the plasma grid, the dominant magnetic field is the EDM field and the region far from the plasma grid is dominated by the filter field which is perpendicular to the EDM field. The filed lines of the magnetic filter connect to those of EDM near the plasma grid as shown in Figure 4-16. Therefore, a transition region of the filter field and the EDM field exists. The flow channel for electrons and positive ions of the flux increments is in this transition region as indicated in Figure 4-15.

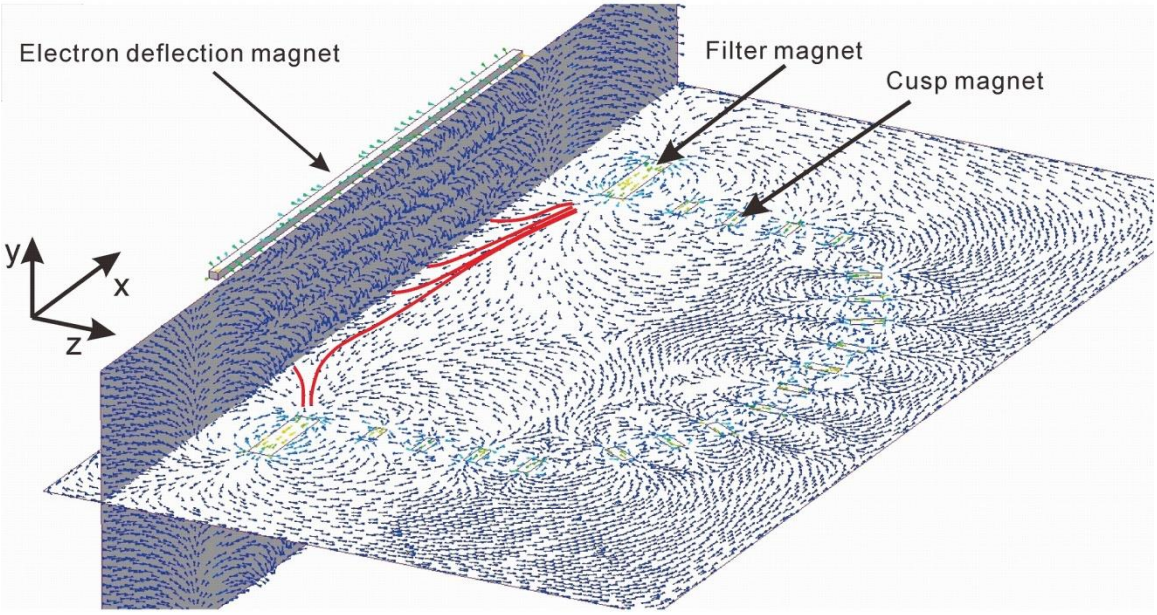

Figure 4-16. Three-dimensional structure of magnetic field of the RNIS.

From the two-dimensional flow pattern of electrons and positive ions, a physical picture of electron and positive ion movements during beam extraction is interpreted as follows.

After the extraction voltage is applied, a part of H^- ions are extracted. To conserve the charge neutrality, electrons flow from the driver region to the extraction region together with some positive ions, since the movements of electrons and positive ions are ambipolar. The mobility along the linkage field from the filter magnet to EDM is larger

than that perpendicular to the magnetic fields induced with both of the magnetic fields. As a consequence, electrons and positive ions mainly flow along the filer field and the linkage field illustrated in Figure 4-16 to the transition region. In this region, electrons and positive ions experience drift in crossed field mainly and are trapped by the magnetic cusp of the EDM field. Finally, electrons and positive ions flow onto the plasma-grid surface guided by the cusp field.

4.5 Summary

In order to understand the mechanism of the flows of electrons and positive ions from the driver region to the extraction region and the unexpected position of the maximum plasma response due to beam extraction, experiments about electrons and positive ion flow were conducted in the extraction region of the RNIS. A four-pin directional Langmuir probe has been utilized for the experiments. The flow direction has been determined by the periodic distribution of the probe saturation current by rotating the directional Langmuir probe. The flow speed has been determined by the difference of probe saturation currents at upstream and downstream positions.

In the extraction region, the flows of electrons and positive ions are dominated by $E \times B$ drift in y direction and ambipolar diffusion in z direction. In Cs-seeded plasma, the two-dimensional flow pattern has been obtained by scanning the measurement position. Subtracting the flow pattern before beam extraction from that during beam extraction, the change of the flow velocity caused by the extraction electric field has been obtained. This flow change indicates the increments of electron and positive ion fluxes. The electrons and positive ions, included in the flux increments, come from the driver region caused by the beam extraction. The process of these electrons and positive ion flowing from the driver region to the extraction region is as follows.

1) The extraction induced electrons and positive ions carrying the flux increments move mainly along the filter field.

2) Following the linkage field, these electrons and positive ions reach the transition region of the EDM field and the filter field.
3) In this transition region, these electrons and positive ions flow from lower side to upper side.
4) These electrons and positive ions are trapped into the magnetic cusp of the EDM field and absorbed by the grid metal.

The transition region acts as a flow channel which is ~20 mm apart from the plasma grid, and is regarded as a source region of the electrons and positive ions. If a Langmuir probe is located in this channel, the maximum plasma response can be detected. This is consistent with the profile measurement in *z* direction described in Chapter 3.

References

[1] M. Hudis and L. M. Lidsky, J. Appl. Phys. **41,** 5011 (1970).

[2] B. J. Peterson, J. N. Talmadge, D. T. Anderson, F. S. B. Anderson, and J. L. Shohet, Rev. Sci. Instrum. **65,** 2599 (1994).

[3] P. C. Stangeby, Phys. Fluids **27,** 2699 (1984).

[4] M. Rack, Y. Liang, H. Jaegers, J. Aßmann, G. Satheeswaran, Y. Xu, J. Pearson, Y. Yang, P. Denner, and L. Zeng, Rev. Sci. Instrum. **84,** 083501 (2013).

[5] A. Tanga, M. Bandyopadhyay, and P. McNeely, Appl. Phys. Lett. **84,** 182 (2004).

[6] K. Nagaoka, A. Okamoto, S. Yoshimura, and Masayoshi Y. Tanaka, J. Phys. Soc. Jpn. **70,** 131 (2001).

[7] Y. Amagishi and T. Miyazaki, J. Phys. Soc. Jpn. **67,** 3774 (1998).

[8] K. Nagaoka, A. Okamoto, S. Yoshimura, M. Kono, and M. Y. Tanaka, Phys. Rev. Lett. **89,** 075001 (2002).

[9] A. Okamoto, K. Nagaoka, S. Yoshimura, J. Vranjes, S. Kado, M. Kono, and M. Y. Tanaka, IEEE Trans. Plasma Sci. **33,** 452 (2005).

[10] K. Nagaoka, T. Ishihara, A. Okamoto, S. Yoshimura, and M. Y. Tanaka, J. Plasma Fusion Res. SERIES **4,** 359 (2001).

[11] F. F. Chen, *Introduction to Plasma Physics and Controlled Fusion* (Springer, 2006).

[12] K.-S. Chung, I. H. Hutchinson, B. LaBombard, and R. W. Conn, Phys. Fluids B **1,** 2229 (1989).

[13] I. H. Hutchinson, Phys. Fluids **30,** 3777 (1987).

[14] K.-S. Chung and I. H. Hutchinson, Phys. Rev. A **38,** 4721 (1988).

[15] H. Nakano, S. Nishiyama, M. Goto, K. Tsumori, M. Kisaki, K. Ikeda, K. Nagaoka, M. Osakabe, Y. Takeiri, O. Kaneko, and K. Sasaki, AIP Conf. Proc. **1655,** 020018 (2015).

[16] M. A. Lieberman and A. J. Lichtenberg, *Principles of Plasma Discharges and Materials Processing* (John Wiley & Sons, 2005).

[17] J. W. Koo and I. D. Boyd, Physics of Plasmas (1994-present) **13,** 033501 (2006).

[18] Y. P. Raizer, *Gas Discharge Physics* (Springer Berlin Heidelberg, 2011).

[19] J. P. Boeuf, B. Chaudhury, and L. Garrigues, Phys. Plasmas **19,** 113509 (2012).

5. H^- ion flow

The measurements of electron and positive ion flows have given a physical picture for the transport processes of electron and positive ions during beam extraction. The two-dimensional patterns of electron and positive-ion flows show that plasma in the extraction region responds to extraction electric field not in the vicinity of the extraction aperture but far from the aperture unexpectedly. The next question is how H^- ions responds to the extraction field and behave in the electron and positive ion flows. Those data lead to the understanding of the mechanism of H^- ions extraction through their production in the extraction region. For this purpose, measurements on the H^- flow are required.

5.1 Possible extraction mechanisms for the extraction of H^- ions

In a Cs-seeded negative hydrogen ion source, H^- ions are mainly produced on the surface with low work function. In a negative hydrogen ion source with converter shown in Figure 5-1, the surface, on which H^- ions are produced, is facing to the extraction aperture [1,2]. The converter is negatively biased. H^- ions produced on the converter surface are accelerated to the plasma by the electric field and extracted directly without collisions [2].

In the negative hydrogen ion source for NBI systems, the plasma grid acts as a converter. H^- ions are produced on the plasma grid surface, which is facing to the plasma, as illustrated in Figure 2-1. The initial directions of the surface produced H^- ions point to the plasma, and the process from production to extraction is not clear.

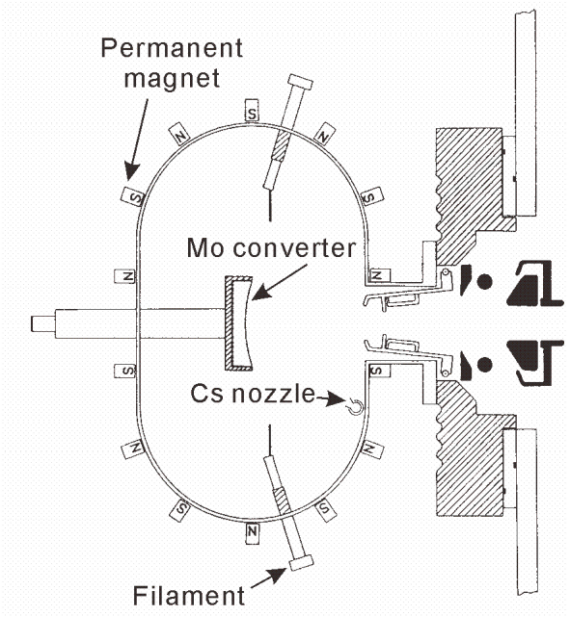

Figure 5-1. Multi-cusp negative hydrogen ion source with converter [1,2].

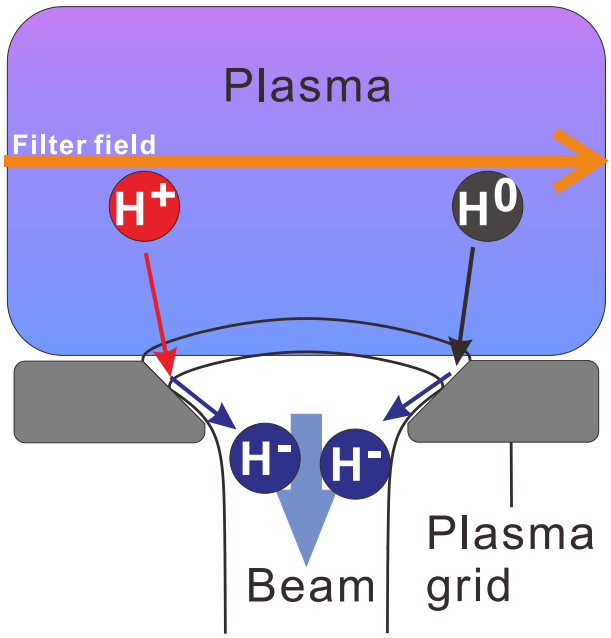

Figure 5-2. Candidate (1) for the mechanism of H^- ion extraction. H^- ions are produced on the conical surface of the aperture and extracted directly.

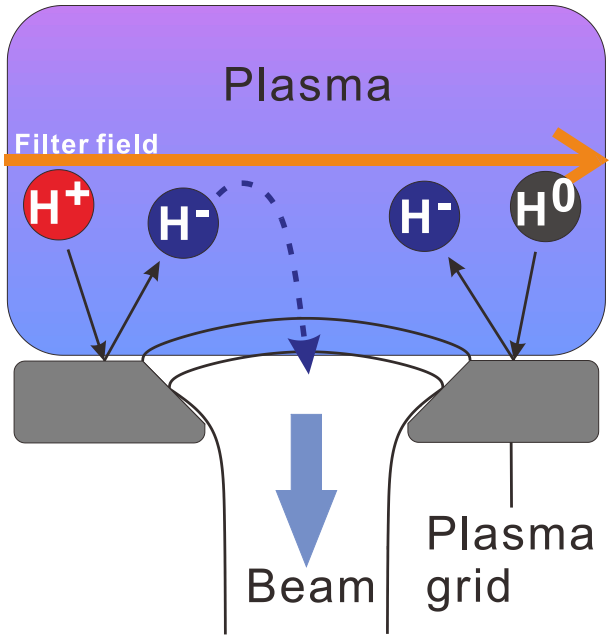

Figure 5-3. Candidate (2) for the mechanism of H^- ion extraction. H^- ions are produced on the plasma grid surface and turn to the extraction aperture in the plasma.

There are two possible extraction mechanisms for H^- ions in Cs-seeded negative hydrogen ion source for NBI:

(1) H^- ions are produced on the conical surface of the plasma-grid aperture and extracted directly to the accelerator as shown in Figure 5-2. This mechanism is similar as the extraction process in the converter-type negative ion source shown in Figure 5-1 [1,2]. By this mechanism, H^- ions do not go through the plasma. Destruction of H^- ions due to collisions is possible to reduce.

(2) H^- ions are produced on the surface of the plasma grid, flow to the plasma in the extraction region, and then turn to the extraction aperture. By this mechanism, a bending process exists from the production to extraction as shown in Figure 5-3. The result obtained with two-dimensional CCD image through H_α filter suggests H^- ions are extracted from wide region in the extraction region [3].

Therefore, experiments on the H^- flow in the extraction region of the RNIS are required to confirm the extraction mechanism of H^- ions.

5.2 Identification of H^- ion flow

5.2.1 Recovery time

In photodetachment, the pulse duration of the laser irradiation is only several nanoseconds. H^- ions in the laser column are detached to H atoms and electrons. An immediate and sharp increase of the photodetachment current is observed due to the swarm of the detached electrons [4] as shown in Figure 5-4 (a). Meanwhile, because the radius of the probe sheath is the same as that before photodetachment in the beginning phase, a spike appears in the waveform of the photodetachment current as discussed in Chapter 2. Photo-detached electrons in the collection region of the probe tip are depleted by the probe and those outside the collection region flow out the laser column [4,5]. H^- ions surrounding the laser column flow into this region to conserve the charge neutrality and recover to its original state as shown in Figure 5-4 (b). In this process the decrement of the photo-detached electron density is affected by the flow-in speed of the negative ions [6]. Thus a plateau appears in the trace of the photodetachment current [7]. After most of the photodetached electrons are depleted, the photodetachment current decreases rapidly. An overshoot appears in the photodetachment current. One of the possibilities is that the overshoot is induced by the combination of the capacitor and the external circuit.

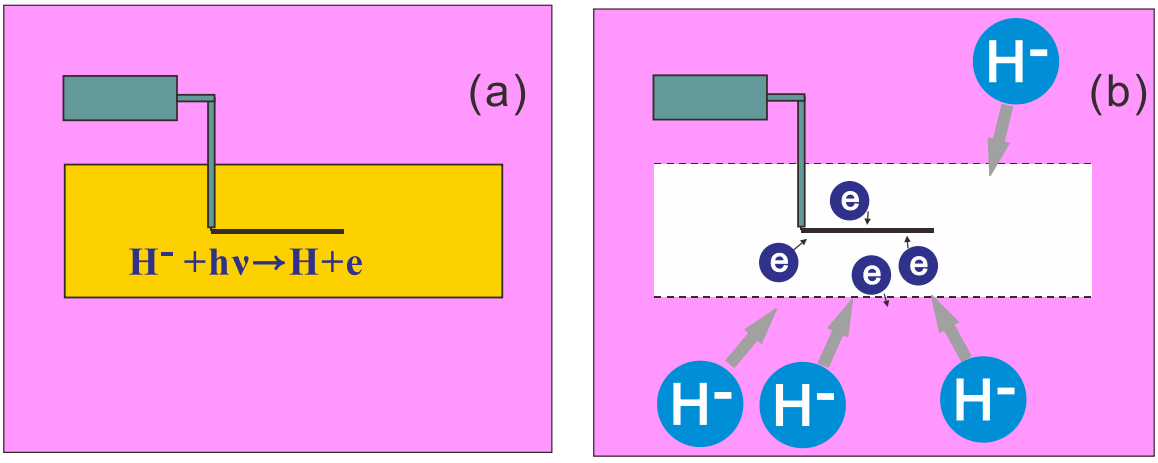

Figure 5-4. Schematic illustration of photodetachment process. (a) during laser irradiation and (b) just after the laser irradiation.

When the negative ions coming from the boundary of the photodetachment region reaches the edge of the probe sheath, all the photo-detached electrons are replaced by negative ions. The photodetachment current then decreases to 0. Therefore, the 0 cross point of the signal is defined as the recovery time [6] as illustrated in Figure 5-5.

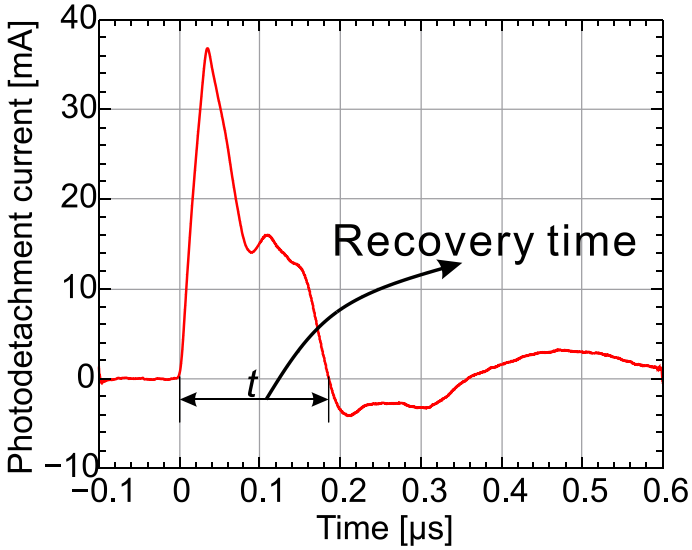

Figure 5-5. Trace of photodetachment current with indication of recovery time.

5.2.2 Recovery speed

With the determination of the recovery time, the recovery speed is then calculated by $v_r = D/t$, where D is the distance from the boundary of the laser column to the edge of the probe sheath, and t is the recovery time. In the laser column, the typical electron density is ~$2.5\times10^{17}/m^3$, and photodetached-electron temperature is ~0.4 eV. The Debye length is on the scale of micrometer. Comparing with the dimension of the probe tip which has a radius of 0.5 mm, the sheath thickness is ignorable. Therefore the recovery speed is then given by $v_r = (R_L - r_p)/t$, where R_L is the radius of the laser beam which is 1.7 mm for the flow measurement and r_p is the probe tip radius of 0.5 mm.

Combining the photodetachment and directional Langmuir probe, Kado et al. proposed a method named Laser Photodetachment Velocimetry (LPDV) to determine the temperature and flow velocity of H^- ions [6]. Due to the shadow effect of the directional Langmuir probe, a difference of the recovery speed at two opposite positions of the

directional Langmuir probe can be observed if the flow of H^- ions exists and the flow velocity and temperature of H^- ion is possible to determine. This method is introduced in Section 5.2.4.

5.2.3 Alignment of laser beam and probe tip

Since the recovery speed is calculated by $v_r = (R_L - r_p)/t_r$, it is essential to align the probe tip in the laser beam co-axially. This work is a challenge in engineering because the probe is enclosed in the ion source and it is impossible to check the positions of laser beam and probe tip directly. Therefore, a method has been developed to check the position of the laser beam as illustrated in Figure 5-6 and Figure 5-7.

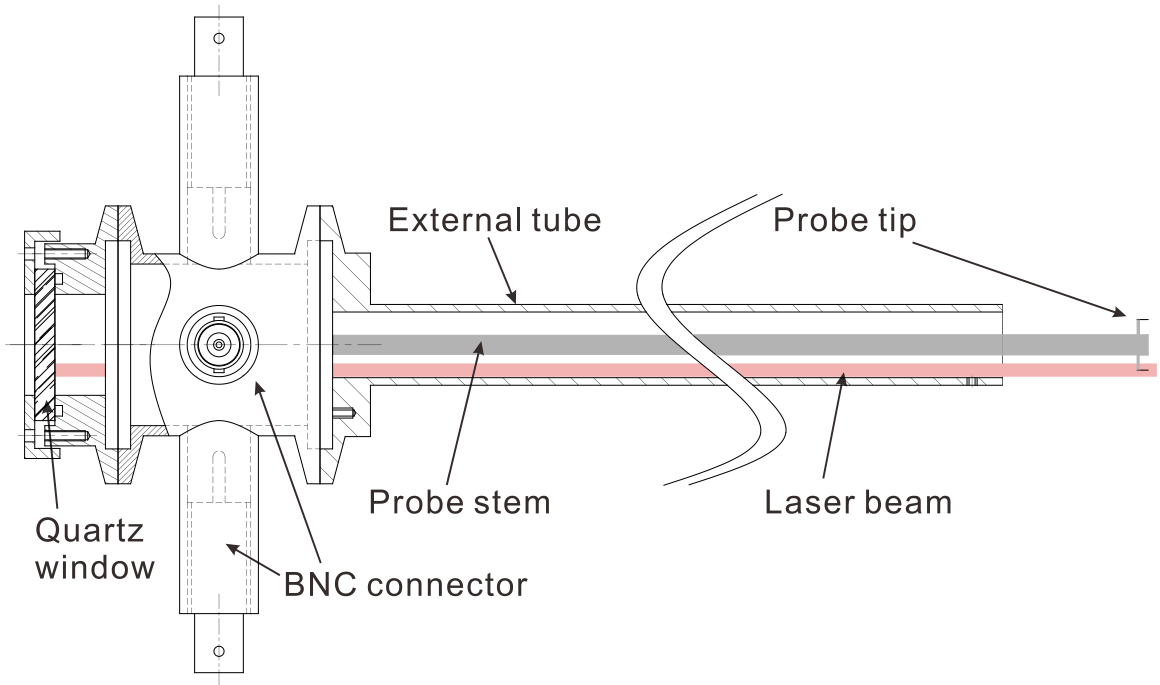

Figure 5-6. Configuration of the four-pin directional Langmuir probe for H^- ion flow measurement.

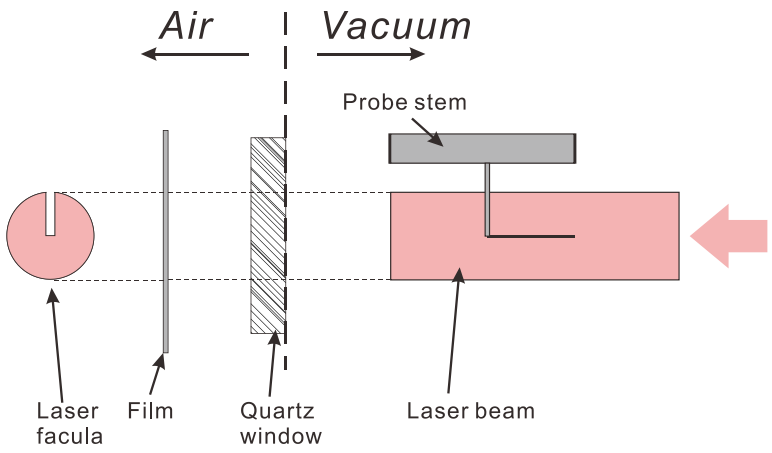

Figure 5-7. Schematic demonstration of the alignment of laser and probe tip. The laser beam position is confirmed from the shade of the probe tip in the laser facula on the film.

The main structure of the system is the external tube as shown in Figure 5-6. Inside this tube the four-pin directional Langmuir probe is installed co-axially. Between the probe stem and the external tube, there is a space. Laser beam irradiated though the probe tip passes through the gap and then the quartz window at the opposite end of the system. Then the laser facula is recorded on a heat sensation film facing to the laser as shown in Figure 5-7. The position of the probe tip in the laser beam is monitored as the shade in the laser facula. If the probe tip is just in the center of the laser beam, the edge of the tip shade is in the center of the laser facula. By this method, the laser was aligned perfectly to make sure the probe tip is co-axial with the laser beam.

5.2.4 Determination of H^- flow and temperature

As introduced in Section 5.2.2, the recovery speed at two opposite positions of the directional Lagnmuir probe is applicable to determine the flow velocity and the temperature of H^- ions. The laser beam was irradiated to each probe tip, respectively, as illustrated in Figure 5-8. Recovery speeds of v_{rA}, v_{rB}, v_{rC}, and v_{rD}, corresponding to probe tip indicated as A, B, C and D, respectively, are obtained from the measurements of recovery times. The H^- flow is assumed to have an x component v_x and a y component v_y, and v_x is from left side to right side. In the flow measurement of positive ions and electrons, it has been found that the thermal velocity is higher than the flow velocity. It is reasonable to assume that thermal velocity of H^- is also higher than its flow velocity.

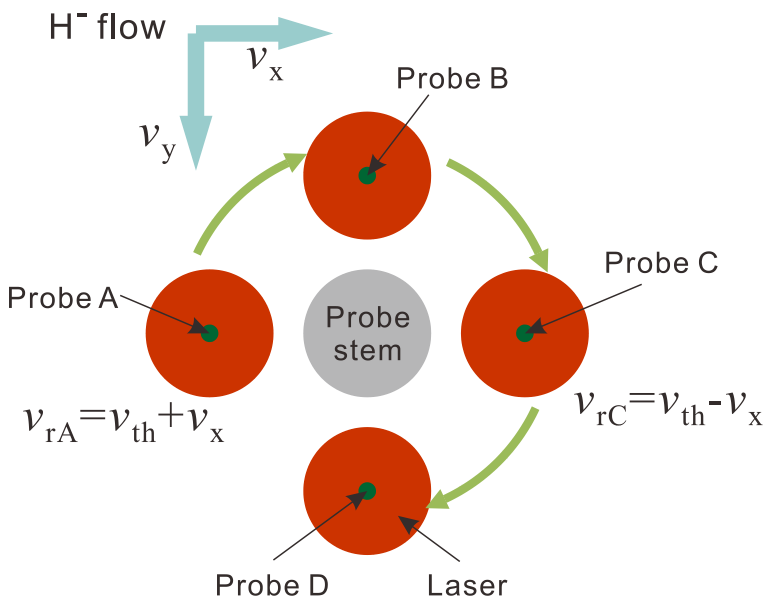

Figure 5-8. Conceptual illustration of the measurement of H^- flow.

With the assumptions above, the recovery speed at probe A and probe C are $v_{rA} = v_{th} + v_x$ and $v_{rC} = v_{th} - v_x$, respectively as shown in Figure 5-8, where v_{th} is the thermal velocity of H^-. v_x and v_{th} are given by

$$\begin{aligned} v_{th} &= \frac{v_{rA} + v_{rC}}{2} \\ v_x &= \frac{v_{rA} - v_{rC}}{2} \end{aligned}, \tag{5-1}$$

With the assumption of Boltzmann velocity distribution of H^- ions, the thermal velocity of H^- ions is expressed as

$$v_{th} = \sqrt{\frac{8kT_{H-}}{\pi m_{H-}}}, \tag{5-2}$$

where T_{H-} is the temperature of H^- ions. By the thermal velocity obtained from Equation 5-1, H^- temperature is then derived.

The data obtained at probe A and C provide H^- temperature and flow velocity in x direction v_x. By the same procedure described above, the flow velocity in y direction v_y is given by the recovery speed at probe B and C. Finally, the total flow velocity is $v_f = v_x + v_y$. v_f is the flow velocity at the center of the probe stem. Therefore, this method provides the mean flow velocity of probe stem position.

5.3 H^- flow and temperature

By the method introduced in Section 5.2, one-dimensional flow velocity has been measured along the central line of the grid metal as indicated in Figure 5-9. The flow velocity at each measurement point is listed in Table 5-1. Note that negative flow velocity indicates the flow points to the negative direction of the coordinate definition. The H^- temperature was estimated to be 0.12 $\pm$0.03 eV in the experiments. This result is consistent with the H^- temperature which is 0.05 – 0.15 eV obtained by saturated cavity ring-down method [8]. The thermal velocity is ~5400 m/s and is one order higher than the flow velocity. The result shown in Figure 5-9 indicates that H^- ions are produced on the surface of the plasma grid and flow to the plasma in the extraction region.

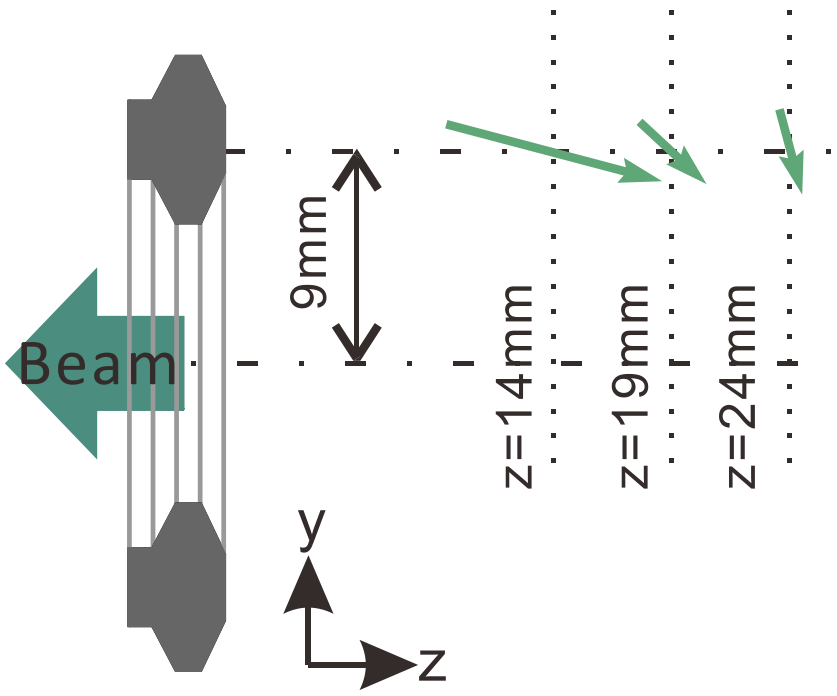

Figure 5-9. One-dimensional H^- flow during beam extraction.

Table 5-1. Flow velocity of H^- ions.

	z = 14mm	z = 19 mm	z = 24 mm
v_y	-298 m/s	-326 m/s	-456 m/s
v_z	1127 m/s	350 m/s	119 m/s
v_f	1166 m/s	478 m/s	461 m/s

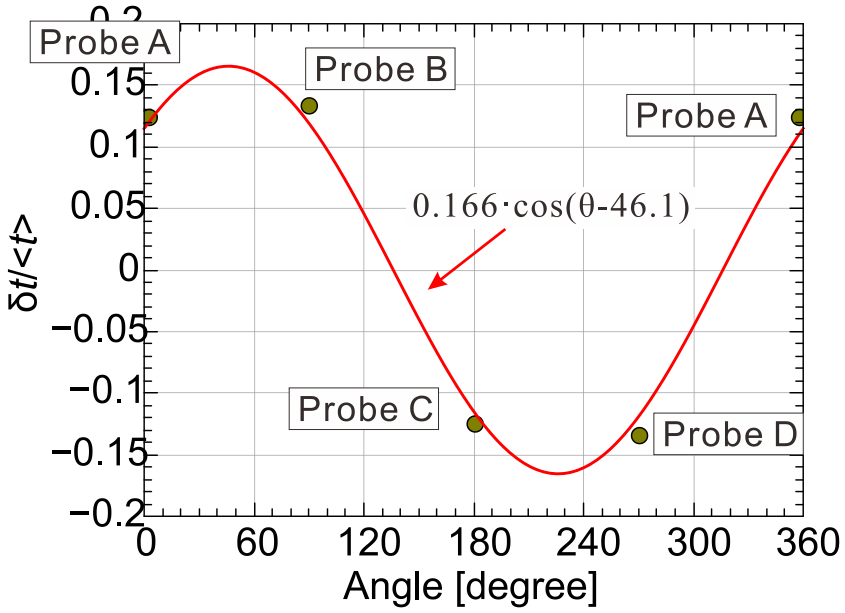

Figure 5-10. Function fitting for the periodic distribution of recovery time.

In Chapter 4, the flow directions of electrons and positive ions are determined by the periodic distribution of the probe saturation current. This method is also useful for H^- ion flow measurement to confirm the measured flow direction. Since the measured quantity is the recovery time t, the ratio $\delta t/\langle t\rangle$ should have a characteristic of shifted cosine function. Following the procedure introduced in Chapter 4, FFT analysis and function fitting can be performed to the experimental data. The result for the data at z = 19 mm is shown in Figure 5-10. It can be found that the function for the experimental data is

0.166 cos(θ-46.1). It means the angle between the incoming flow and the z axis is 46.1°. On the other hand, this angle is also calculated by arctan(v_y/v_x). At z = 19 mm, the angle is arctan(326/350) = 43° which is close to the value determined by function fitting. Therefore, the method to measure the H^- flow by the recovery time can be confirmed.

5.4 Production and extraction of H^- ions

5.4.1 Flow pattern of H^- ions

By scanning the measurement position in the beam extraction region, two-dimensional flow pattern of H^- ions has been obtained during beam extraction. As shown in Figure 5-11, there are 12 measurement points on *y*-*z* plane. The horizontal axis in Figure 5-11 indicates the distance from the plasma grid. The origin of vertical axis indicates the center of the extraction aperture of the plasma grid. Similar as the two-dimensional flow pattern discussed in Chapter 4, the details of the flow pattern is not sufficient in arrow plot. In order to have more information, interpolation has been performed to obtain the streamline plot as shown in Figure 5-12 with the indication of the measurement region.

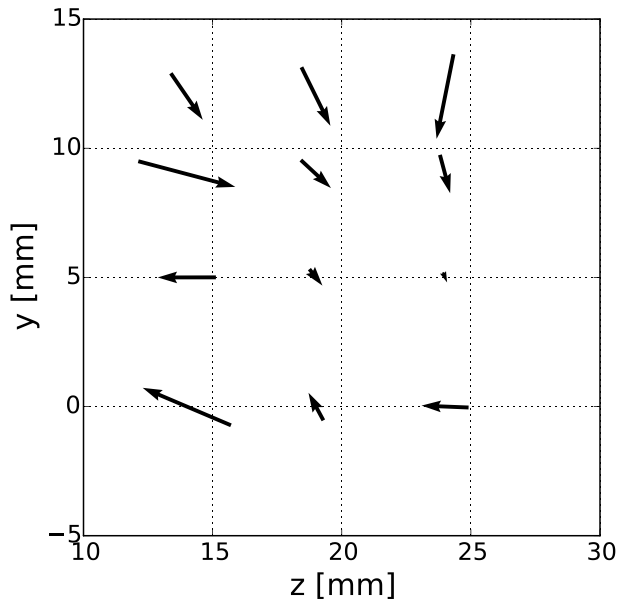

Figure 5-11. Arrow plot of two-dimensional H^- flow pattern

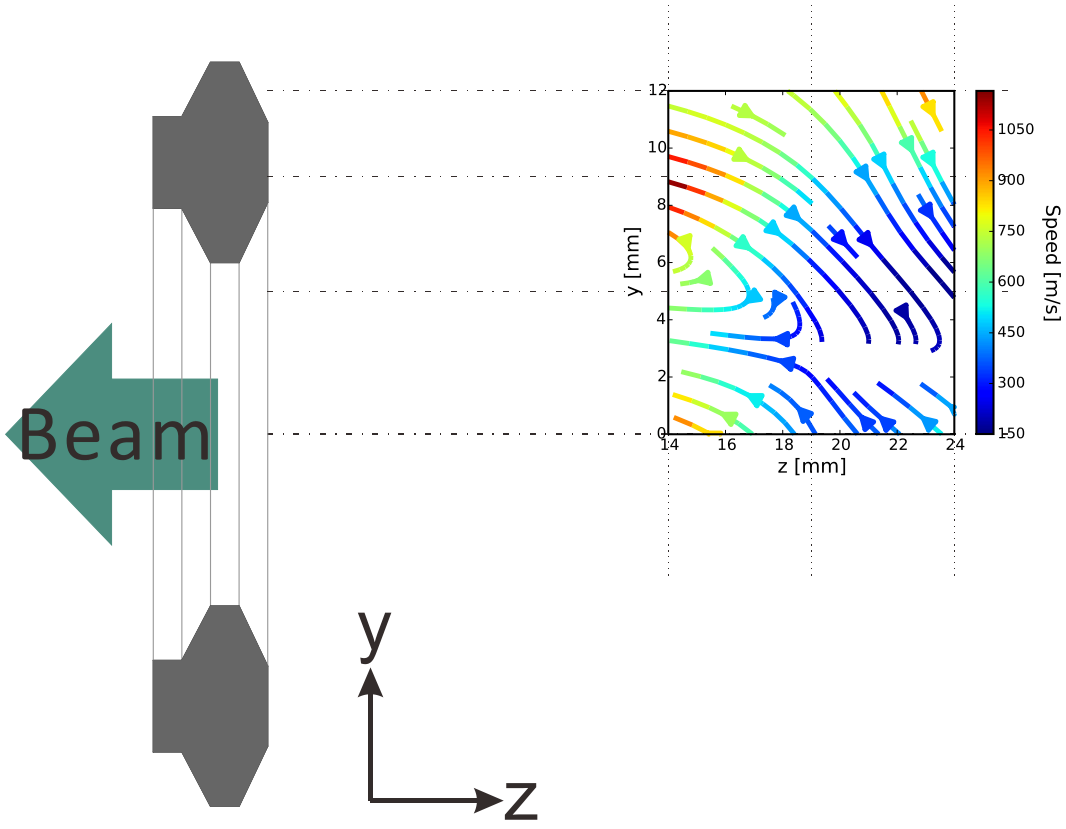

Figure 5-12. Streamline plot of the two-dimensional H^- flow pattern with the indication of the measurement region during extraction.

The flow pattern in Figure 5-12 has been obtained at hydrogen pressure of 0.3 Pa and bias voltage of the 0.3 V which is applied to the plasma grid. This flow pattern shows H^- ions come from the direction of the plasma grid surface and flow to the plasma in the extraction region. H^- ions from the direction of upper grid metal flow to the lower side, and those from the direction of lower grid metal flow to the upper side. They join together near the central line of the extraction aperture and turn to the aperture direction. Comparing with the flow pattern of positive ions discussed in Chapter 4, the H^- ions in the upper part of the measurement region flow to the opposite direction of the positive ion flow. It suggests that the flows of H^- ions and positive ions are mutual. Positive ions feel the attraction of the H^- ions produced on the plasma grid surface and flow to upper direction and turn to the plasma grid. Meanwhile, H^- ions are attracted by positive ions,

leave the plasma grid, and flow to the opposite direction of positive ion flow in the plasma.

5.4.2 Production of H^- ions

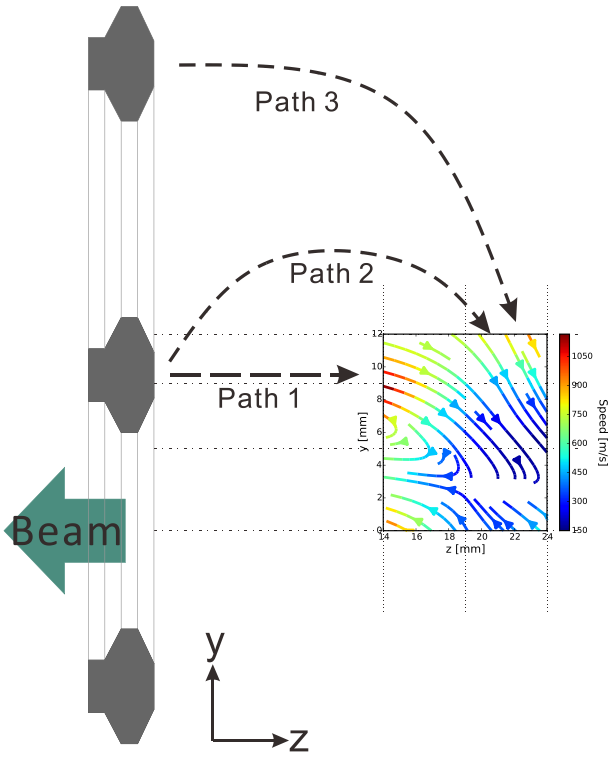

Figure 5-13. Possible paths of H^- ions from the surface of the plasma grid to the extraction region.

The two-dimensional flow pattern of H^- ions indicates that H^- ions in the extraction region are mainly from the direction of the plasma grid. The surface production of H^- ions has been confirmed. From the plasma grid surface to the extraction region, there are three possible paths as shown in Figure 5-13:

(1) H^- ion produced on the surface of the plasma grid flow to the plasma directly along path 1.

(2) H^- ions produced on the surface of the plasma grid travel along a curve, along path 2 to the plasma.

(3) H^- ions may come from the neighbor grid metal, travel long distance to the extraction region. This process is demonstrated as path 3.

In addition, H^- ion flow in x direction, not shown in Figure 5-13 is also possible.

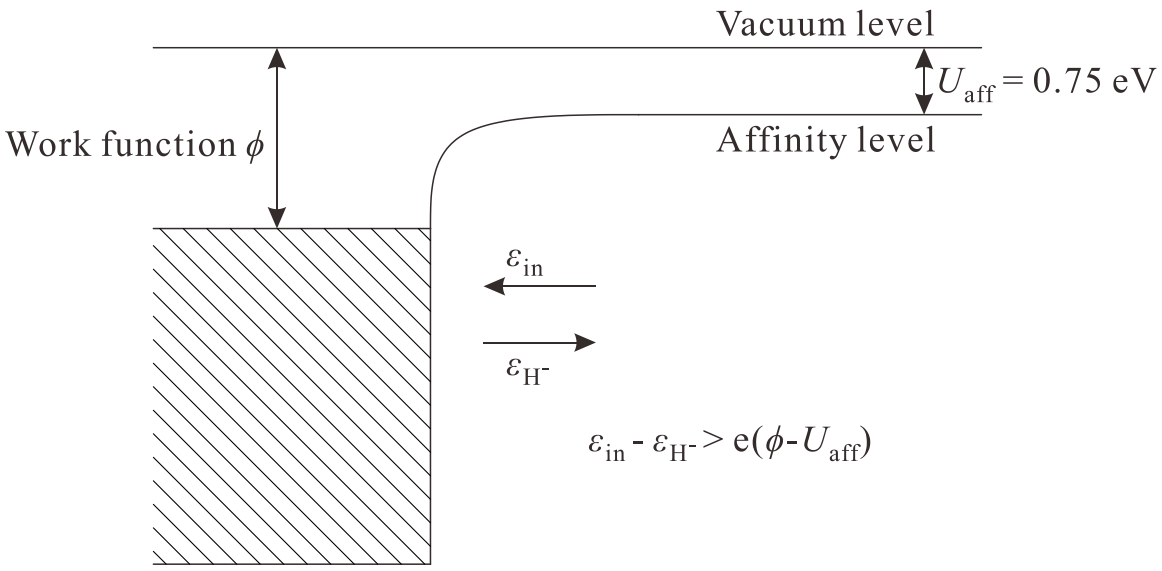

Figure 5-14. Energy relation of incident particle and H^-.

In the Cs-seeded negative ion source, it has been confirmed that H^- ions are produced on the surfaced of the caesiated plasma grid. The H^- temperature has been evaluated to be 0.05 – 0.15 eV by saturated cavity ring-down and ~0.12 eV by photodetachment. H^- ions are produced by the conversion of incident particles impact on the plasma grid. The balance relation between the energy of incident particles and outgoing H^- energy can be expressed as [9] $\varepsilon_{H^-} = \varepsilon_{in} - e(\phi - U_{aff})$, where ε_{H^-} is the energy of outgoing H^- ions, ε_{in} is the energy of incident particles, ϕ is the work function of the ceasiated plasma grid surface, and U_{aff} is the affinity energy of H^-. H^- ions can escape from the surface of the plasma grid only if $\varepsilon_{H^-} > 0$ or $\varepsilon_{in} > \varepsilon_{H^-} + e(\phi - U_{aff})$. In the case of well Cs-conditioning, ϕ can be assumed to be 1.45 eV, and U_{aff} is 0.75 eV. Considering ε_{H^-} is 0.05 – 0.15 eV, ε_{in}

should be higher than 0.85 eV. The H atom energy has been evaluated by Hα Laser Absorption Spectroscopy (Hα LAS) to be ~ 0.3 eV [10], which is lower than the required incident energy 0.85 eV. On ther other hand, in the experiments by High-resolution Optical Emission Spectroscopy (HR-OES), 0.8 – 1.0 eV of particle energy has been observed. The particles monitored in HR-OES experiments and cause Doppler shift are considered to be H_n^+, due to the response to the bias voltage of the plasma grid [11]. It suggests that H_n^+ has enough energy for the production of H^- ions. Therefore, the parent particles of H^- ions are considered to be H_n^+.

5.4.3 Extraction of H^- ions

From the two-dimensional flow pattern of H^- ions shown in Figure 5-12, it can be found that H^- ions flow to the plasma from the surface of the plasma grid turn to the aperture direction. The bending of H^- ion flow confirms one of the extraction mechanisms of H^- ions, that is, H^- ions come from the plasma grid surface turn their flow direction in the plasma as demonstrated in Figure 5-3.

The stagnation point of H^- ions is at ~ 20 mm apart from the plasma grid. It corresponds to the position where the maximum decrement of H^- density appears and the flow channel of extraction induced additional positive ion and electron fluxes. H^- ions in the region between plasma grid and the stagnation point can be extracted. Outside this region, H^- ions are trapped by the filter field and flow to the driver region due to the gradient of plasma potential. Therefore, H^- ions are not extracted directly from the plasma grid, but mainly from the region near the extraction aperture with a boundary of ~20 mm apart from the plasma grid.

5.4.4 Stagnation point of H^- flow

The position of stagnation point of H^- flow is interpreted to be determined by the boundary of the EDM field and the Larmor radius of H^-. It has been introduced in Chapter 2 that a EDM loop field is generated in the gap between the extraction grid and

the plasma grid by a series of permanent magnet bars to deflect the co-extracted electrons from the extracted beam. The EDM field penetrates into the extraction region though the plasma grid as shown in Figure 2-7. The two-dimensional of the plasma profile suggests that the boundary of the EDM field in the plasma is ~10 mm apart from the plasma grid. In addition, in the extraction region of the RNIS, the Larmor radius of H^- is ~10 mm. An H^- ion turns back to the aperture direction at ~10 mm apart from the boundary of the EDM field as demonstrated in Figure 5-15. It means the turning point is at ~20 mm apart from the plasma grid. The four-pin directional Langmuir probe with photodetachment provides the averaged effect of large amount of H^- ions. The turning positions of lots of H^- ions are detected as the stagnation point of H^- ions flow.

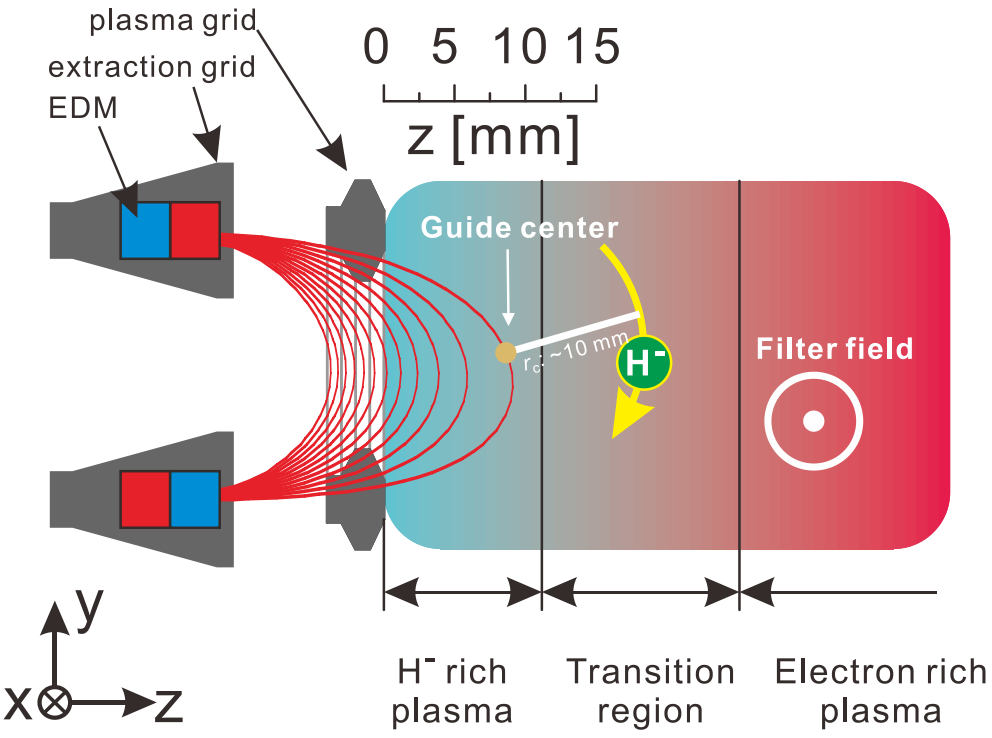

Figure 5-15. Turning of an H^- ion.

5.5 Summary

In order to understand the unexpected position of the reduction of H^- ion density caused by the extraction electric field and the extraction mechanism of H^- ions in the Cs-seeded plasma, four-pin directional Langmuir probe with photodetachment was utilized to the experiment to measure the H^- flow in the extraction region. The temperature and flow velocity of H^- ion were determined by the recovery speed at opposite tips of the directional Langmuir probe. Temperature of H^- ions was evaluated to be ~0.12 eV which is consistent with the result obtained by saturated cavity ring-down. The velocity of H^- flow is one order lower than the thermal velocities of H^- ions. By scanning the measurement position in the extraction region, two-dimensional flow pattern has been obtained. The results of H^- temperature and flow pattern during extraction indicate that:

(1) H^- ions come from the direction of the plasma-grid surface in the Cs-seeded plasma, flow to the plasma in the extraction region, and turn to the aperture during extraction.

(2) Stagnation point of H^- flow is at ~20 mm apart from the plasma grid. This position corresponds to the location where the maximum plasma response due to extraction appears. The channel of extraction induced additional electron and position fluxes is also in the same position in *z* direction.

(3) H^- flow is governed by the EDM field.

(4) H^- ions are not extracted from the plasma grid surface directly, but mainly from the region near the aperture.

(5) The extraction process occurs in a region near the aperture with a boundary of ~20 mm apart from the plasma grid.

(6) The parent particles of H^- ions are considered to be H_n^+.

(7) The low H^- temperature is one of the evidences for the low divergence angle of the beam.

References

[1] A. F. Lietzke, K. W. Ehlers, and K. N. Leung, AIP Conf. Proc. **111,** 344 (1984).

[2] I. G. Brown, *The Physics and Technology of Ion Sources* (John Wiley & Sons, 2004).

[3] K. Ikeda, H. Nakano, K. Tsumori, M. Kisaki, K. Nagaoka, M. Osakabe, Y. Takeiri, and O. Kaneko, New J. Phys. **15,** 103026 (2013).

[4] R. A. Stern, P. Devynck, M. Bacal, P. Berlemont, and F. Hillion, Phys. Rev. A **41,** 3307 (1990).

[5] M. Bacal, Rev. Sci. Instrum. **71,** 3981 (2000).

[6] S. Kado, S. Kajita, T. Shikama, Y. Iida, D. Yamasaki, A. Okamoto, and S. Tanaka, Contrib. Plasma Phys. **46,** 367 (2006).

[7] S. Christ-Koch, U. Fantz, M. Berger, and N. Team, Plasma Sources Sci. Technol. **18,** 025003 (2009).

[8] H. Nakano, K. Tsumori, M. Shibuya, S. Geng, M. Kisaki, K. Ikeda, K. Nagaoka, M. Osakabe, Y. Takeiri, and O. Kaneko, Journal of Instrumentation **11,** C03018 (2016).

[9] A. Pargellis and M. Seidl, Physical Review B **25,** 4356 (1982).

[10] H. Nakano, S. Nishiyama, M. Goto, K. Tsumori, M. Kisaki, K. Ikeda, K. Nagaoka, M. Osakabe, Y. Takeiri, O. Kaneko, and K. Sasaki, AIP Conf. Proc. **1655,** 020018 (2015).

[11] K. Tsumori, K. Ikeda, H. Nakano, M. Kisaki, S. Geng, M. Wada, K. Sasaki, S. Nishiyama, M. Goto, G. Serianni, P. Agostinetti, E. Sartori, M. Brombin, P. Veltri, C. Wimmer, K. Nagaoka, M. Osakabe, Y. Takeiri, and O. Kaneko, Rev. Sci. Instrum. **87,** 02B936 (2016).

6. **Conclusions and outlook**

Negative ion based neutral beam injector (N-NBI) is an indispensable device for plasma heating and current drive for a fusion reactor due to the advantages of high neutralization efficiency at high beam energy and low beam divergence angle. As the source of negative ions, the ion source determines the performance of the N-NBI system. In order to understand the mechanisms of electron and positive ion flow during beam extraction and the extraction of H^- ions in Cs-seeded plasma for the improvement of the present negative hydrogen ion source, investigation on charged particle dynamics of the negative-ion-rich plasma is required. In this research, Langmuir probe, cavity ring-down, photodetachment, and four-pin directional Langmuir probe have been utilized for the experiments on the RNIS to investigate the characteristics of the negative-ion-rich plasma and the charged particle flows.

In Chapter 1 of this thesis, the worldwide energy issue and the importance of the development of magnetic confinement fusion was introduced. A neutral beam injector can inject high energy particles into a fusion device to heat the core plasma and drive plasma current. Having the advantages of high neutralization efficiency and low beam divergence angle, the N-NBI system is a preferable choice. The basis of negative hydrogen ion source has been introduced in this Chapter. In a negative hydrogen ion source, negative ions (H^-) are produced by two mechanisms: (1) a hydrogen molecule is vibrationally excited by the collision with a fast electron and a slow electron can attach onto this exited H_2 molecule. The decay of this molecule produces a hydrogen atom and a negative ion. This process is named dissociative attachment and this mechanism is named “volume production”; (2) a proton or hydrogen atom impacts on the ceasiated metal surface which has low work function, the incident particle is possible to capture electrons from the metal and bound back as an negative ion (H^-). This mechanism is named “surface production”. In a practical negative ion source, Cs vapor is seeded and H^- ions are mainly produced by surface mechanism. N-NBI systems have contributed

remarkable achievements on LHD at NIFS and on JT-60SA at JAEA. At NIFS, it has been observed in the negative ion source that n_{H^-} decreases and electron density n_e increases during beam extraction. Understanding of the mechanisms of the electron and positive ion flow in the extraction region and H^- extraction is requied for the improvement of the negative hydrogen ion source. Therefore, research on charged particle dynamic of negative-ion-rich has been conducted.

In Chapter 2, the negative ion source utilized for the experiments named Research and Development Negative Ion Source (RNIS) was introduced and described, as well as the diagnostic methods. This ion source is divided into a driver region and an extraction region by a transversal magnetic field named filter field. Plasma is generated by filament-arc discharge and confined in the multi-cusp magnetic field. During the diffusion process of the plasma from the driver region to the extraction region, electrons are trapped into the filter field and collide with neutral and charged particles, lose energy and the electron temperature decreases to be lower than 1 eV. Loss of H^- ions by electron detachment decreases and plasma with high n_{H^-} is obtained in the extraction region. A bias voltage is applied to the plasma grid to suppress electrons and decrease the electron density near the plasma grid. A magnetic field generated by electron deflection magnets, named "EDM field" is used to deflect the co-extracted electrons and filter the electron component from the extracted beam. Three diagnostic tools have been applied to the experiments: Langmuir probe, cavity ring-down (CRD) and photodetachment. The Langmuir probe has been used to obtain basic plasma parameters such as plasma potential, electron density and electron temperature. The CRD provided line-averaged H^- ion density. The photodetachment technique was applied to measure the H^- density at a specific point. In the negative-ion-rich plasma, traditional method based on the probe current and electron density to evaluate H^- ion density from the photodetachment current is not available. Therefore, a new method by combining the CRD and the photodetachment technique has been developed. The coefficient $k_{pd} = 0.105 \times 10^{17} \cdot m^{-3} \cdot mA^{-1}$ has been estimated by the comparison of line-integrated H^- ion density and the integral of the profile of the photodetachment current along the laser beam. By using this new method, the H^- density can be determined not only in the plasma with low density H^- ions but also in negative-ion-rich plasma, even in ion-ion plasma in which essentially no

electrons exist. For photodetachment, laser with wavelength of 1064 nm is necessary. In order to drain all the detached electrons, the DC voltage applied to the probe should be higher than 40 V. The laser beam is required to have a diameter higher than 2 mm. The energy density of laser pulse should be in the range of 40 – 90 mJ/cm^2 to detached all the H^- ions in the laser column and avoid overestimation of the local H^- ion density.

In Chapter 3, the basic characteristics of the RNIS have been investigated by the diagnostics tools introduced in Chapter 2. By seeding Cs into the ion source, n_{H^-} increases slowly and meanwhile n_e decreases. During Cs-conditioning, the plasma potential V_s decreases due to the emission of H^- ions from the plasma-grid surface and H^- ion density increases comparable to electron. The influence of bias voltage of the plasma grid on the plasma has been investigated. The negative saturation current of probe I_{neg} decrease monotonically with the increasing bias voltage of the plasma grid V_{bias}. Correspondingly, the extraction current shows the same characteristic as I_{neg}. H^- ion density n_{H^-} keeps stable at negative V_{bias} and decreases slowly when V_{bias} is positive. The acceleration current shows the same behavior as that of n_{H^-}. It is necessary to apply low bias voltage to the plasma grid in order to obtain high H^- beam current with the premise of avoiding damage on the extraction grid. Hydrogen pressure also influences the plasma in the extraction region. n_{H^-} decreases at high pressure due to the mutual neutralization with positive ions. As a consequence, extraction and acceleration currents decrease as the pressure increases at high pressure. Low operational gas pressure is beneficial to the RNIS, because stripping loss of H^- ions due to collisions with neutral molecules and atoms are reduced at lower pressure. However, the discharge is unstable in extremely low gas pressure, because the plasma of the RNIS is sustained by electrons impact ionization and the mean free paths of electrons are large at lower pressure. In addition, electron percentage in the source plasma increases with respect to H^- percentage in low gas pressure. Consequently, 0.2 to 0.4 Pa of hydrogen pressure is a proper choice for the operation of the negative ion source.

Plasma produced in the driver region diffuse across the filter field to reach the extraction region. Therefore, the profile of the filter field affects the distribution of the plasma in the extraction region. Plasma in the extraction region concentrates in the

central part of the extraction region. Near the plasma grid, electrons are trapped into the magnetic cusp of the EDM field and absorbed by the metal part of the plasma grid. The boundary of the EDM field is estimated to be at ~10 mm apart from the plasma grid.

In *z* direction perpendicular to the plasma grid, the experimental results show the maximum plasma response to the extraction electric field is at ~20 mm apart from the plasma grid. The boundary of extraction region and driver region is estimated to be at ~40 mm apart from the plasma grid. Although the maximum response is initially expected close to the extraction aperture, the experimental results show that the peak position of the plasma response is located far from the plasma grid. The understanding of this unexpected phenomenon requires the information of charged particle flows in the extraction region.

In Chapter 4, flows of electrons and positive ions have been investigated by a four-pin directional Langmuir probe. The flow direction has been determined by the periodic distribution of the probe saturation current by rotating the directional Langmuir probe. The flow speed has been determined by the difference of probe saturation currents at upstream and downstream positions. In the extraction region, the flows of electrons and positive ions are dominated by $E \times B$ drift in *y* direction and ambipolar diffusion in *z* direction. In Cs-seeded plasma, the two-dimensional flow pattern has been obtained by scanning the measurement position. Subtracting the flow pattern before beam extraction from that during beam extraction, the change of the flow velocity caused by the extraction electric field has been obtained. This flow change is considered as the flux increments of electrons and positive ions caused by the extraction electric field. The flux increments come from the transition region of filter field and EDM field, which is at ~20 mm apart from the plasma grid, move from lower side to upper side, and are finally trapped into the magnetic cusp of the EDM field. If a Langmuir probe is located in the transition region, maximum plasma response is detected.

In Chapter 5, the four-pin directional Langmuir probe with photodetachmen has been utilized to the experiments to investigated H^- flow for the understanding of the extraction mechanism and the unexpected position of the maximum H^- ion density reduction. The temperature and flow velocity of H^- have been determined by the recovery speed at

opposite tips of the directional Langmuir probe. Temperature of H^- ion has been evaluated to be ~0.12 eV which is consistent with the result obtained by saturated cavity ring-down. The velocity of H^- flow is one order lower than the thermal velocity. By scanning the measurement position in the extraction region, two-dimensional flow pattern has been obtained. H^- ions come from the direction of the plasma grid, flow to the plasma in the extraction region and turn to the aperture in the plasma. The extraction mechanism of H^- has been confirmed by this result. H^- flow has a stagnation point which is at ~ 20 mm apart from the plasma grid. The maximum H^- density reduction appears near the stagnation point. The stagnation point is affected by the boundary of the EDM field and the Larmor radius of H^- ion. H^- ions are not extracted directly from the plasma grid surface, but from the region near the aperture. The extraction process occurs in the region near the aperture with a boundary of ~20 mm apart from the plasma grid. From the evaluated H^- temperature, the parent particles of H^- ion are considered as H_n^+. The low H^- temperature is one of the evidences for the low divergence angle of the H^- ion beam.

The Cs-conditioning process suggests that the expansion of Cs atoms in the negative ion source is complicated and slow. Before reaching the plasma grid, Cs atoms are covered on the wall of the plasma chamber. In order to enhance the Cs transport, increasing the temperature of the plasma chamber by active temperature controlling is possible. In the future, experiments by replacing the cooling water of the plasma chamber by hot water will be carried out to enhance the vaporization of Cs covered on the wall of the plasma chamber. It is expected that Cs-conditioning time and Cs consumption is decreased.

Because the EDM field can suppress the electrons near the plasma grid, and the stagnation point of H^- flow is governed by the boundary of the EDM field. Increasing the strength of the EDM field is beneficial to the suppression of electrons and increase of H^- current. In addition, the boundary of the EDM field is expanded and the area of the extraction region is increased. Consequently, enhancement of electron suppression is expected and extracted H^- beam current is increased.

In order to obtain high H^- beam current, Cs has to be seeded into the ion source. However, Cs vapor can pollute the acceleration stage. High consumption of Cs will increase the maintenance time of the negative ion source. The development of Cs-free negative hydrogen ion source is necessary. In the future, alternative materials with low work function such as diamond and diamond-like-carbon will be investigated for the surface production of H^- ions as alternative materials for Cs-free negative hydrogen ion source.

List of figures

List of tables

Published papers and conference presentations

The followings are the published papers related to this research

(1) Shaofei GENG, Katsuyoshi TSUMORI, Haruhisa NAKANO, Masashi KISAKI, Katsunori IKEDA, Masaki OSAKABE, Ken-ichi NAGAOKA, Yasuhiko TAKEIRI, Masayuki SHIBUYA and Osamu KANEKO, "Depth of Influence on the Plasma by Beam Extraction in a Negative Hydrogen Ion Source for NBI", Plasma Fusion Res. 11, 2405037 (2016).

(2) S. Geng, K. Tsumori, H. Nakano, M. Kisaki, K. Ikeda, M. Osakabe, K. Nagaoka, Y. Takeiri, M. Shibuya, and O. Kaneko, "Charged Particle Flows in the Beam Extraction Region of a Negative Ion Source for NBI", Rev. Sci. Instrum. 87, 02B103 (2016).

(3) Shaofei GENG, Katsuyoshi TSUMORI, Haruhisa NAKANO, Masashi KISAKI, Yasuhiko TAKEIRI, Masaki OSAKABE, Katsunori IKEDA, Ken-ichi NAGAOKA, Osamu KANEKO, Masayuki SHIBUYA and NIFS NBI Group, “Spatial distributions of charged particles and plasma potential before and during beam extraction in a negative hydrogen ion source for NBI”, Plasma Fusion Res. 10, 3405016 (2015).

(4) S. Geng, K. Tsumori, H. Nakano, M. Kisaki, K. Ikeda, Y. Takeiri, M. Osakabe, K. Nagaoka, and O. Kaneko, “Laser photodetachment diagnostics of a 1/3-size negative hydrogen ion source for NBI”, AIP Conf. Proc. 1655, 040014 (2015).

The followings are conference presentations related to this research

(1) S. Geng, K. Tsumori, H. Nakano, M. Kisaki, K. Ikeda, M. Osakabe, K. Nagaoka, Y. Takeiri and M. Shibuya, "Response of H^- ions to extraction field in a negative

hydrogen ion source", 29th Symposium on Fusion Technology (SOFT 2016), 5-9 September 2016, Prague, Czech Republic.

(2) Shaofei GENG, Katsuyoshi TSUMORI, Haruhisa NAKANO, Masashi KISAKI, Katsunori IKEDA, Masaki OSAKABE, Kenichi NAGAOKA, Masayuki SHIBUYA, Yasuhiko TAKEIRI, "Positive and Negative Ion Flows in the Vicinity of Plasma Grid in a Negative Hydrogen Ion Source for Neutral Beam Injector", 第 11 回 核融合エネルギー連合講演会, 14-15 July, 2016, 九州大学伊都キャンパス, 福岡.

(3) S. Geng, K. Tsumori, H. Nakano, M. Kisaki, K. Ikeda, M. Osakabe, K. Nagaoka, Y. Takeiri, M. Shibuya, and O. Kaneko, "Response of charged particle flows to the extraction field in a negative hydrogen ion source for NBI", 第 32 回プラズマ・核融合学会 年会, Nov. 24-27, 2015, 名古屋大学東山キャンパス・豊田講堂, 名古屋.

(4) S. Geng, K. Tsumori, H. Nakano, M. Kisaki, K. Ikeda, M. Osakabe, K. Nagaoka, Y. Takeiri, M. Shibuya, and O. Kaneko, "Depth of Influence on the Plasma by Beam Extraction in a Negative Hydrogen Ion Source for NBI", 25th International Toki Conference, November 3-6, 2015, Ceratopia Toki, Toki-city, Gifu, Japan.

(5) S. Geng, K. Tsumori, H. Nakano, M. Kisaki, K. Ikeda, M. Osakabe, K. Nagaoka, Y. Takeiri, M. Shibuya, and O. Kaneko, "Charged particle flows in the beam extraction region of a negative ion source for NBI", 16th International Conference on Ion Sources, August 23-28, 2015, New York, USA.

(6) Shaofei Geng, Katsuyoshi Tsumori, Haruhisa Nakano, Masashi Kisaki, Yasuhiko Takeiri, Masaki Osakabe, Katsunori Ikeda, Ken-ichi Nagaoka, Osamu Kaneko and Masayuki Shibuya, Spatial Distribution of Negative Hydrogen Ions in the Extraction Region of a Negative Hydrogen Ion Source for NBI, Plasma Conference 2014, November 18 – 21, 2014, 朱鷺メッセ, 新潟.

(7) Shaofei GENG, Katsuyoshi TSUMORI, Haruhisa NAKANO, Masashi KISAKI, Yasuhiko TAKEIRI, Masaki OSAKABE, Katsunori IKEDA, Ken-ichi NAGAOKA, Osamu KANEKO, Masayuki SHIBUYA and NIFS NBI Group, Spatial distributions of charged particles and plasma potential before and during beam extraction in a negative hydrogen ion source for NBI, 24th International Toki Conference, November 4-7, 2014, Ceratopia Toki, Toki-city, Gifu, Japan.

(8) S. Geng, K. Tsumori, H. Nakano, M. Kisaki, K. Ikeda, Y. Takeiri, M. Osakabe, K. Nagaoka, and O. Kaneko, Laser photodetachment diagnostics of a 1/3-size negative hydrogen ion source for NBI, 4th International Symposium on Negative Ions, Beams and Sources (NIBS 2014) 6 - 10 October 2014, IPP Garching, Germany.

(9) S. F. Geng, K. Tsumori, H. Nakano, M. Kisaki, K. Ikeda, Y. Takeiri, M. Osakabe, Influence of bias voltage on H- density in the negative ion source for NBI by Langmuir probe and photodetachment measurements, 第 10 回 核融合エネルギー連合講演会 19-20 June, つくば.

Acknowledgements

It was my pleasure to have the opportunity as a doctoral student to study in SOKENDAI (the Graduate University for Advanced Studies). This work was administrated by SOKENDAI and implemented at NIFS. I would like to express my gratitude to SOKENDAI and NIFS for the financial support for my study.

The three-year doctoral course was a precious experience in my life. I learned a lot from the courses and the experiments. The knowledge in science and technology is valuable and made me have a comprehensive understanding of fusion and negative ion source. I believe this experience is helpful very much for my future career. Many thanks to all the people I met here.

This research was supervised by Prof. Katsuyoshi Tsumori, Prof. Masaki Osakabe and Dr. Haruhisa Nakano. They gave me undivided guidance, training and support. During my research, Prof. Takeiri, Dr. Kisaki, Dr. Nagaoka and Dr. Ikeda also provided indispensable assistance and gave me many crucial and helpful suggestions and comments. With the guidance and assistance, I learned many experimental techniques and experience and can finish my research and doctoral thesis. I would like to express my deep gratitude to them.

Mr. Hitoshi Hayashi helped me very much for the preparation of the experiments and operated the negative ion source during the experiment, taught me how to use the tools in the laboratory. His work provided huge support for my experiments. Mr. Masayuki Shibuya helped me a lot for the data acquisition systems. I cannot finish my research without his work. I am grateful very much to them for their support.

I would like to thank all the technical stuffs for their work on the disassembly, maintaining and installation of the negative hydrogen ion source.

I would like to express my great gratefulness for the financial support by YUKWAI and JASSO scholarship. With the support, I can devote all my attentions to my research without concern about the daily life.

Finally, I must acknowledge my wife Dr. Haiying Fu. She has sacrificed a lot in the last three years. I am grateful to her for her unconditional support and inspiration.